Integration of Geodesy Mission Design and Navigation for Planetary Satellite Orbiters

by

Dylan R. Boone

B.S.E., Aerospace Engineering, University of Michigan, 2004

M.Eng., Space Systems, University of Michigan, 2005

M.S., Aerospace Engineering Sciences, University of Colorado, 2011

A thesis submitted to the

Faculty of the Graduate School of the

University of Colorado in partial fulfillment

of the requirements for the degree of

Doctor of Philosophy

Department of Aerospace Engineering Sciences

2013

This thesis entitled:
Integration of Geodesy Mission Design and Navigation for Planetary Satellite Orbiters
written by Dylan R. Boone
has been approved for the Department of Aerospace Engineering Sciences

_____

Daniel J. Scheeres

_____

George H. Born

_____

R. S. Nerem

_____

Hanspeter Schaub

_____

John Wahr

Date _____

The final copy of this thesis has been examined by the signatories, and we find that both the content and the form meet acceptable presentation standards of scholarly work in the above mentioned discipline.

Boone, Dylan R. (Ph.D., Aerospace Engineering Sciences)

Integration of Geodesy Mission Design and Navigation for Planetary Satellite Orbiters

Thesis directed by Prof. Daniel J. Scheeres

Planetary satellites have become the primary targets of proposed missions to the outer planets as the places in the Solar System most likely to harbor extraterrestrial life. Observations from the Galileo spacecraft suggest Europa has a subsurface salt-bearing ocean and water plumes have been observed at Enceladus's south pole. However, orbits about planetary satellites are known to be unstable due to the perturbing gravity of the primary body. This work investigates the properties of phase space in the vicinity of a periodic orbit and examines the effect of these properties on the orbit evolution and lifetime. Low altitude, near-polar periodic orbits are found in the Circular Restricted Three Body Problem and a covariance matrix is generated for each nominal periodic orbit by processing range-rate and altimetry measurement types in a Square-root Information Filter. Computed Love number estimation uncertainties yield similar or better performance than previous studies. This processed covariance is used to draw randomly dispersed initial conditions around the periodic orbit from a multivariate normal distribution in a Monte Carlo analysis. These simulation results show a bias toward longer lifetime orbits that is associated with the linear manifolds of an unstable periodic orbit. Lifetimes for both Europa and Enceladus orbiters are increased by an order of magnitude over the nominal lifetime and long lifetime orbits are not isolated in phase space. A mathematical development of information accumulation in the orbit determination process is given for the Europa L_2 equilibrium point using the eigenstructure decomposition of the State Transition Matrix. The covariance matrix for an equilibrium point orbit is shown to collapse along the left unstable manifold for epoch state estimation and collapse along the left stable manifold for current state estimation.

Dedication

For my parents Bob and Roxanne, for their love and encouragement supporting me through my move to Colorado and completion of the Ph.D.

Acknowledgements

Contents

Appendix

Tables

Table

x

Figures

Figure

Chapter 1

Introduction

Planetary satellites have become the primary targets of proposed missions to the outer planets as the places in the Solar System most likely to harbor extraterrestrial life. Observations from the Galileo spacecraft suggest Europa has a subsurface salt-bearing ocean and water plumes have been observed at Enceladus's south pole. The presence of liquid water combined with tidal deformation as a possible heat source point to the possible existence of microbial or other forms of life at such planetary satellites. Potential missions to Europa have gone through many design iterations under names such as Europa Orbiter, Jupiter Icy Moons Orbiter, and Jupiter Europa Orbiter (JEO). A descoped version of the JEO mission called the Europa Clipper has now been proposed involving multiple flybys of the moon only, which could confirm the presence of a subsurface ocean [1].

Orbits about planetary satellites are known to be unstable due to the perturbing gravity of the third body. This effect is dependent on the inclination of the orbit and the strength of the third body's gravity. The goal of the JEO [2] mission is to measure the Love numbers, geophysical coefficients which give insight into whether there is liquid water on the body. Missions like JEO require near-polar, mapping type orbits which are greatly affected by this gravitational instability. General low altitude, high inclination orbits impact on the surface of the planetary satellite after a time span on the order of weeks [3]. Periodic orbits computed in the Restricted Three Body Problem have the potential to extend this lifetime to the order of months [4]. A JEO type mission is used here as a baseline for a potential Europa orbiter mission. While there is currently no call

for an Enceladus mission in the 2013 Planetary Science Decadal survey [5], an Enceladus orbiter would encounter the same stability challenges and desire similar geodesy measurements.

1.1 Icy Moons Background

Geodesy missions generally require low altitude, high inclination orbits with good spatial coverage for mapping considerations and good temporal coverage for sensing tides. One issue for the Europa mission is instability due to perturbations on high-inclination orbits from Jupiter's gravity. The desired low altitude, polar orbits are highly unstable and lead to impact with Europa after several weeks. The most recent NASA description of the mission calls for a one month mapping mission after Europa Orbit Insertion with the possibility of orbit correcting maneuvers. The nominal parameters for the Europa orbit are a 100 km altitude, circular orbit with inclination between $95°$ and $100°$. This high inclination results in a decline of periapsis radius due to an increase in the orbit's eccentricity. This is shown in Figure 1.1 where the red line shows Europa's surface radius which intersects the blue periapse radius curve after about 13 days. Other studies [6, 7, 8] use this type of orbit in geodesy simulations for a Europa mapping mission but do not discuss the effects of this decay of periapse. Thus, there is a need to evaluate the performance of Europa orbits in terms of orbit lifetime and stability and the measurement precision of desired science parameters.

A low-altitude, near-polar Enceladus orbiter would experience a similar decay of periapsis due to the perturbing third-body gravity of Saturn. Such orbits would impact on the order of days. Missions to both Europa and Enceladus would be interested in determining the depth of a subsurface ocean and the ice shell thickness. These measurements are related to the Love numbers, geophysical coefficients which characterize the strength of a body's response to tidal gravity [9]. The amount of time-varying surface deformation is related to the h_2 Love number and can be estimated through altimetry measurements. Changes in a body's gravity field due to mass redistribution is tied to the k_2 Love number [10] and can be estimated through Doppler or range-rate tracking. These measurement types are included in a covariance analysis for Europa to bound the uncertainty
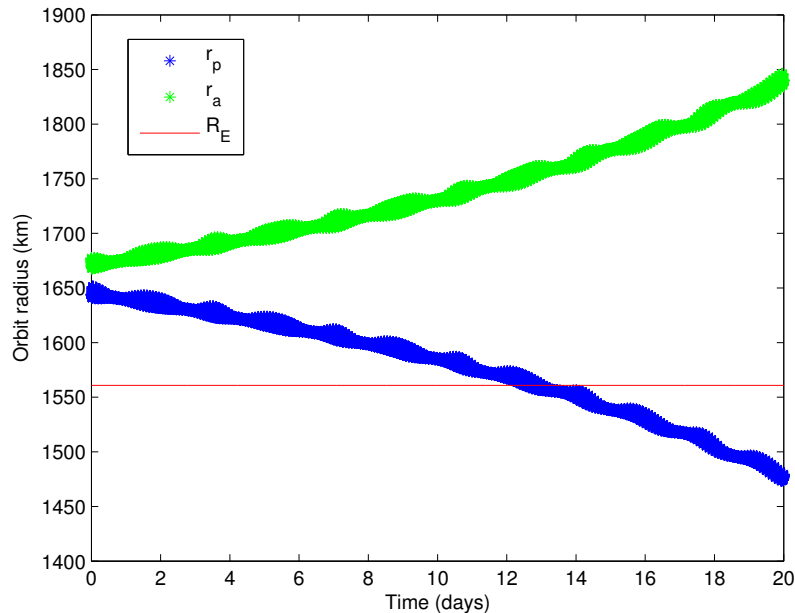
Figure 1.1: Typical geodesy orbit periapse decay

in measuring the Love numbers for a particular orbit.

1.2   Literature Review

The geophysical structure of icy moons such as Europa and Enceladus has been modeled by many authors. From geophysical models and Galileo flyby data, Anderson et al.[11] suggest that Europa's structure is differentiated into a metallic core, rocky mantle, and an ice-liquid shell that may vary in thickness from 80 to 170 km. Moore and Schubert [12] give several Love number models for different ice thickness and ocean depths and show that observing tidal deflection alone is not sufficient to determine the ice thickness. Similar models for Enceladus ice thicknesses and Love numbers are given in Olgin et al. [13]. The ability to detect a subsurface ocean from orbit is examined in Rappaport et al. [14] where a greater than 90% probability is given for validating the presence of an ocean from determination of the k_2 Love number. This work implements Love number models similar to those in previous work in a realistic covariance analysis and examines the resulting covariance in position and velocity space. This covariance is used to evaluate the

statistical lifetime properties of low altitude, near-polar orbits.

Periodic orbits at Europa in particular and also Enceladus are the subject of many published investigations. Frozen orbits are computed through averaging techniques at Europa to be used as science orbits in Paskowitz-Possner [15, 16] and San-Juan et al. [17]. Periodic orbits in the Restricted Three Body Problem are computed by Russell at Europa [18] and Enceladus [19] in global searches but most are of altitudes too great for low altitude mapping missions. Long-lifetime orbits at Europa are computed in Gomez et al. [20] and in Lara et al. [21] with lifetimes greater than 150 days in the ephemeris model but the question of how isolated those orbits are in phase space is not answered. This work computes periodic orbits at Europa and Enceladus and generates realistic covariance matrices about these orbits. Europa orbits with similar maximum lifetimes to previous studies are found and new, low altitude, long lifetime Enceladus orbits are found. The properties of periodic orbits are shown to influence the lifetime distribution of orbits in their phase space vicinity.

The stability of Europa orbits is studied in Lara et al. [22] through characterizing the orbits by the eigenvalues of the State Transition Matrix. The stable and unstable eigenvalues and eigenvectors of periodic orbits are shown to influence information accumulation in the orbit determination process. Scheeres et al. [23] investigate the alignment of stable and unstable manifolds of halo orbits with the direction of maximum uncertainty in phase space. In this work, the left unstable and stable manifolds of periodic orbits are shown to control the directions of uncertainty compression for epoch and current state accumulation of information, respectively. Mathematical development of these characteristics is given and confirmed in simulation at an equilibrium point.

1.3   Summary of Results

This work investigates the properties of phase space in the vicinity of a periodic orbit and examines the effect of these properties on the orbit evolution and lifetime. Low altitude, near-polar periodic orbits are found in the Circular Restricted Three Body Problem [24] at the Jupiter-Europa

and Saturn-Enceladus systems using a differential corrector [25]. A covariance matrix is generated for each nominal periodic orbit by processing range-rate and altimetry measurement types in a Square-root Information Filter [26]. Parameters which affect the estimation process but which are not estimated themselves, called consider parameters [27], are included in the Europa covariance analysis. Models for Love numbers at Europa are taken from the geophysical studies referenced and k_2 and h_2 Love number estimation uncertainties are produced for accumulating measurements about a Europa periodic orbit. Generation of a realistic covariance is key to the discussion of statistical lifetime properties of the orbits considered. This processed covariance is used to draw randomly dispersed initial conditions around the periodic orbit from a multivariate normal distribution in a Monte Carlo analysis for both Europa and Enceladus. The dispersed orbits are integrated in the inertial frame including the effects of Europa and Enceladus eccentricity about their primaries, which would be the main effect of an ephemeris integration. These simulation results show a bias toward longer lifetime orbits that is associated with the linear manifolds of an unstable periodic orbit [28]. These long-lifetime orbits are shown to be dense in the phase space vicinity of these periodic orbits. The concept of manifold coordinates [29] reveals what components of the orbit initial conditions are aligned with the stable, unstable, and center manifolds associated with the periodic orbit, respectively. Lifetimes for both Europa and Enceladus orbiters are increased by an order of magnitude over the nominal lifetime. The nominal periodic orbit at Europa is continued [30, 31] into a family of periodic orbits to show that no one particular set of manifolds is controlling the phase space distribution. A mathematical development of information accumulation in the orbit determination process given at the Europa L_2 equilibrium point using the eigenstructure decomposition of the State Transition Matrix. The covariance matrix for range-rate measurements at an equilibrium point is shown to collapse along the left unstable manifold for epoch state estimation. Conversely, the covariance matrix is shown to collapse along the left stable manifold for current state estimation. This is shown to be a function of mapping measurements and the information matrix in time via the State Transition Matrix.

The main contributions of this thesis are:

- Accounting for navigation uncertainties in the design of long lifetime geodesy orbits at Europa

- Understanding the properties of phase space near a periodic orbit in terms of its stable and unstable manifolds, orbit lifetime, and orbit determination

- Showing a fundamental structure to information and measurement partial mapping in terms of the stability properties of an equilibrium point

- Enabling geodesy science at Enceladus by computing statistically realistic long lifetime orbits

Chapter 2

Restricted Three Body Problem

The specific astrodynamic problem under consideration is the Restricted Three Body Problem (RTBP). The equations of motion are applied to the Jupiter-Europa system and the Saturn-Enceladus system. The RTBP equations of motion are expressed in the secondary-centered rotating frame where the primary and secondary are in circular orbits about their mutual center of mass [24].

2.1   Equations of Motion

First, the equations of motion are constructed in the barycenter inertial frame.
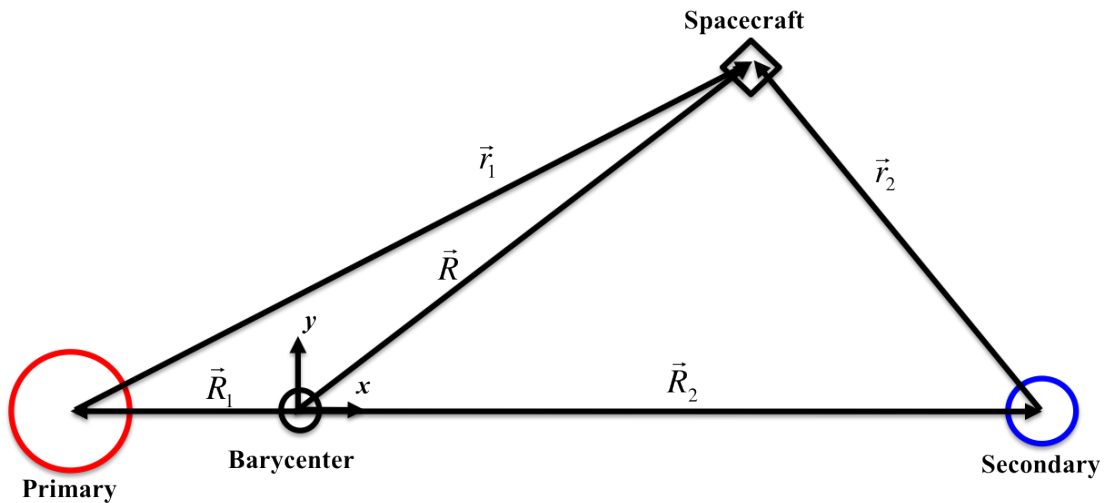
Figure 2.1: Geometry of Restricted Three Body Problem

Figure 2.1 shows the geometry of the problem. The $\hat{x}$ direction points away from the primary's

initial position on the primary-secondary line, the $\hat{z}$ direction is aligned with secondary's angular momentum vector, and the $\hat{y}$ direction completes a right-handed coordinate system.

$$\begin{aligned}\ddot{\boldsymbol{R}} &= -\mu_1\frac{\boldsymbol{r}_1}{|\boldsymbol{r}_1|^3} - \mu_2\frac{\boldsymbol{r}_2}{|\boldsymbol{r}_2|^3} \\ &= -\mu_1\frac{\boldsymbol{R}-\boldsymbol{R}_1}{|\boldsymbol{R}-\boldsymbol{R}_1|^3} - \mu_2\frac{\boldsymbol{R}-\boldsymbol{R}_2}{|\boldsymbol{R}-\boldsymbol{R}_2|^3}\end{aligned} \tag{2.1}$$

A coordinate transformation is used to shift the origin of the coordinate system from the barycenter to Europa's center of mass.

$$\boldsymbol{R} = \boldsymbol{r}_2 + \boldsymbol{R}_2 \tag{2.2}$$

Taking the inertial derivative of Equation 2.2 gives:

$$\ddot{\boldsymbol{R}} = \ddot{\boldsymbol{r}}_2 + \ddot{\boldsymbol{R}}_2 \tag{2.3}$$

and the motion of the secondary about the primary, neglecting the mass of the satellite for the restricted problem:

$$\ddot{\boldsymbol{R}}_2 = -\mu_1\frac{\boldsymbol{R}_2-\boldsymbol{R}_1}{|\boldsymbol{R}_2-\boldsymbol{R}_1|^3} = \mu_1\frac{\boldsymbol{R}_{21}}{|\boldsymbol{R}_{21}|^3} \tag{2.4}$$

where the position of the primary with respect to the secondary is $\boldsymbol{R}_{21} = \boldsymbol{R}_1 - \boldsymbol{R}_2$. Substituting Equations 2.3 and 2.4 into Equation 2.1 gives the equations of motion for a planetary satellite orbiter in the inertial frame, centered at the secondary. Dropping the $_2$ subscript designating the secondary and adding an $_I$ subscript denoting the inertial frame yields:

$$\ddot{\boldsymbol{r}}_I = -\mu_1\frac{\boldsymbol{r}_I-\boldsymbol{R}_{21}}{|\boldsymbol{r}_I-\boldsymbol{R}_{21}|^3} - \mu_2\frac{\boldsymbol{r}_I}{|\boldsymbol{r}_I|^3} - \mu_1\frac{\boldsymbol{R}_{21}}{|\boldsymbol{R}_{21}|^3} \tag{2.5}$$

Equation 2.5 is used for orbit lifetime integrations and includes the eccentricity of the secondary's orbit about the primary. This eccentricity is included in the $\boldsymbol{R}_{21}$ term where the secondary's orbit is stepped in the perifocal frame, assuming the inclination of the secondary-primary orbit is zero. Now the inertial equations of motion for the three-body system are transformed to a rotating frame to form the Circular Restricted Three Body Problem. The assumptions made are that the primary and secondary bodies are in circular orbit about their mutual center of mass, and that the body-fixed secondary centered rotating frame rotates at a constant rate n_S with respect to the inertial

frame [34].

$$n_S = \sqrt{\frac{\mu_1 + \mu_2}{a_S^3}} \tag{2.6}$$

Assuming that the two frames are aligned at epoch, the following transformations are applied to form the rotating frame equations of motion. The $_I$ subscript represents inertial frame quantities and the $_R$ subscript represents rotating frame quantities.

$$
\begin{aligned}
\boldsymbol{r}_I &= \boldsymbol{r}_R \\
\dot{\boldsymbol{r}}_I &= \dot{\boldsymbol{r}}_R + n_S \hat{z} \times \boldsymbol{r}_R \\
\ddot{\boldsymbol{r}}_I &= \ddot{\boldsymbol{r}}_R + 2 n_S \hat{z} \times \dot{\boldsymbol{r}}_R + n_S \hat{z} \times (n_S \hat{z} \times \boldsymbol{r}_R)
\end{aligned}
\tag{2.7}
$$

This results in two quantities involving the cross product of the secondary's rotation rate being subtracted from the inertial equations to form the rotating frame equations.

$$\ddot{\boldsymbol{r}}_R = -\mu_1 \frac{\boldsymbol{r}_R - \boldsymbol{R}_{21}}{|\boldsymbol{r}_R - \boldsymbol{R}_{21}|^3} - \mu_2 \frac{\boldsymbol{r}_R}{|\boldsymbol{r}_R|^3} - \mu_1 \frac{\boldsymbol{R}_{21}}{|\boldsymbol{R}_{21}|^3} - 2 n_S \hat{z} \times \dot{\boldsymbol{r}}_R - n_S \hat{z} \times (n_S \hat{z} \times \boldsymbol{r}_R) \tag{2.8}$$

The periodic orbits studied in this work are computed in the rotating frame using the RTBP equations. Equation 2.8 is non-dimensionalized using units derived from system parameters to facilitate numerical computation. The semi-major axis of the primary-secondary mutual orbit a_S is used as a length unit (LU) and the time unit (TU) is chosen such that the system mean motion n_S is unity. The non-dimensional parameter μ characterizes the system, where $\mu_1 = 1 - \mu$ and $\mu_2 = \mu$.

$$\mu = \frac{\mu_2}{\mu_1 + \mu_2} \tag{2.9}$$

The coordinate translation from the barycenter to the secondary affects the x coordinate, such that $x \rightarrow x + 1 - \mu$. The equations of motion for the non-dimensional RTBP centered at the secondary in Cartesian coordinates then become:

$$
\begin{aligned}
\ddot{x} &= 2\dot{y} + (x + 1 - \mu) - (1 - \mu)\frac{x+1}{r_1^3} - \mu\frac{x}{r_2^3} \\
\ddot{y} &= -2\dot{x} + y - (1 - \mu)\frac{y}{r_1^3} - \mu\frac{y}{r_2^3} \\
\ddot{z} &= -(1 - \mu)\frac{z}{r_1^3} - \mu\frac{z}{r_2^3}
\end{aligned}
\tag{2.10}
$$

where the spacecraft distances to the primary and secondary, respectively are:

$$
\begin{aligned}
r_1 &= \sqrt{(x+1)^2 + y^2 + z^2} \\
r_2 &= \sqrt{x^2 + y^2 + z^2}
\end{aligned}
\tag{2.11}
$$

The RTBP admits an additional integral of motion called the Jacobi integral C. Each scalar component in Equations 2.10 is multiplied by $2\dot{x}$, $2\dot{y}$, and $2\dot{z}$ respectively with the gravity terms written in potential form. The three equations are summed resulting in:

$$
2\dot{x}\ddot{x} + 2\dot{y}\ddot{y} + 2\dot{z}\ddot{z} - 2\left((x+1-\mu)\,\dot{x} + y\dot{y}\right) =
$$
$$
2\dot{x}\frac{\partial}{\partial x}\left(\frac{1-\mu}{r_1} + \frac{\mu}{r_2}\right) + 2\dot{y}\frac{\partial}{\partial y}\left(\frac{1-\mu}{r_1} + \frac{\mu}{r_2}\right) + 2\dot{z}\frac{\partial}{\partial z}\left(\frac{1-\mu}{r_1} + \frac{\mu}{r_2}\right)
\tag{2.12}
$$

This equation forms a total differential. Integrating with respect to time gives the Jacobi integral or Jacobi energy C.

$$
C = (x+1-\mu)^2 + y^2 - \left(\dot{x}^2 + \dot{y}^2 + \dot{z}^2\right) + 2\left(\frac{1-\mu}{r_1} + \frac{\mu}{r_2}\right)
\tag{2.13}
$$

The Jacobi energy is used to distinguish different periodic orbits. The parameters for each system such as length and time units and gravity coefficients are given in the chapters for each planetary satellite examined.

2.1.1   Spherical Harmonics

The equations of the RTBP include point-mass gravity terms for the primary and secondary bodies. For a planetary satellite orbiter, any non-sphericity of the secondary body has an effect on the spacecraft orbit. One way of expressing the non-spherical components of a gravity field is through a spherical harmonic potential U. Each C_{nm} and S_{nm} is a Stokes coefficient of degree n and order m and expresses some component of the gravity field. In these simulations, the Stokes coefficients are non-dimensionalized using the radius of the secondary body to the nth power but remain unnormalized. The ΔC_{nm} and ΔS_{nm} terms represent time-variable gravity due to tidal forces acting on the secondary. This expansion is an infinite series in Stokes coefficients

and associated Legendre polynomials P_{nm}, which are part of the solution to Laplace's equation in spherical coordinates. The $_2$ subscript indicates parameters of the secondary body, ϕ and λ are the orbiter latitude and longitude, and r is the magnitude of the orbiter position.

$$U = \frac{\mu_2}{r} \sum_{n=2}^{N} \sum_{m=0}^{n} \left(\frac{R_2}{r}\right)^n P_{nm}\left(\sin(\phi)\right) \left[(C_{nm} + \Delta C_{nm})\cos(m\lambda) + (S_{nm} + \Delta S_{nm})\sin(m\lambda)\right] \quad (2.14)$$

The associated Legendre polynomials are defined as follows.

$$P_{nm}(x) = \frac{(-1)^m}{2^n n!} \left(1 - x^2\right)^{m/2} \frac{\partial^{n+m}}{\partial x^{n+m}} \left(x^2 - 1\right)^n \quad (2.15)$$

In the case of the gravitational potential, the x in Equation 2.15 is $\sin(\phi)$. The spherical harmonic gravitational potential is converted to Cartesian coordinates using the definition of spherical coordinates given in Equations 2.16 and trigonometric substitution to reduce the $\cos(m\lambda)/\sin(m\lambda)$ terms to single λ arguments.

$$
\begin{aligned}
x &= r\sin(\phi)\cos(\lambda) \\
y &= r\sin(\phi)\sin(\lambda) \\
z &= r\cos(\phi)
\end{aligned}
\quad (2.16)
$$

The gradient of the potential of Europa's extended gravity field is taken in the rotating frame with respect to $\boldsymbol{r}$, the rotating frame position vector. For inertial integrations, the potential gradient is transformed into the inertial frame using a rotation $R3$ about the secondary body's angular momentum axis $\hat{z}$ with magnitude $n_S t$, the secondary sidereal angle.

2.1.2   Time-variable Gravity and Love Numbers

The instability of orbits about planetary satellites is due to the perturbing gravity of the primary mass or third body. This perturbing gravity also raises tides on the surface of the secondary body. Tides redistribute mass on the secondary which in turn changes the gravity field. This can be represented by fluctuations in the Stokes coefficients of the spherical harmonic gravity potential. The physical parameters which characterizes a body's tidal response are the Love numbers. The

Love numbers h_2 and k_2 are coefficients of the tide-raising potential which measure the amplitude of the elastic response of a deformed body. These are dimensionless coefficients and are related to the spherical harmonic expansion of a gravitational potential. Just as the second degree oblateness coefficient of a spherical body will dominate the gravitational perturbation spectrum, the second degree tidal potential and thus the second degree Love numbers dominate tidal perturbations. For the second degree coefficients, the k_2 Love number applies to all orders [10]. The h_2 Love number measures the strength of the tidal surface deformation of a body and the k_2 Love number measures the strength of the time-variation in gravitational coefficients [9].

$$\Delta C_{nm} - i\Delta S_{nm} = \frac{k_{nm}}{2n+1}\frac{\mu_1}{\mu_2}\left(\frac{R_2}{r_1}\right)^{n+1} P_{nm}\left(\sin(\phi_1)\right) e^{-im\lambda_1} \tag{2.17}$$

Equation 2.17 represents the time-variation in the Stokes coefficients C_{nm}/S_{nm} which are coefficients of the spherical harmonic gravitational potential of degree n and order m. This variation involves the associated Legendre polynomial P_{nm} and is a function of the Love number k_2, the position of the primary with respect to the secondary in spherical coordinates (r_1, ϕ_1, λ_1), and other system parameters. The complex notation is used to denote that the cosine terms are associated with ΔC_{nm} and the sine terms are associated with ΔS_{nm}. While time variations in the gravity coefficients are necessary for sensing k_2 in the estimation process, care must be taken with ΔC_{20} and ΔC_{22} as both have nonzero time averages. This effectively changes the nominal value of these coefficients, so the time average component must be subtracted in the dynamics.

$$s_R\left(t\right) = \frac{h_2}{g_e}U_2 \tag{2.18}$$

Equation 2.18 shows the dependence of radial surface uplift s_R on the h_2 Love number, the surface gravity of Europa g_e, and the tidal potential of degree two U_2 used in Wahr et al.. This tidal potential in Equation 2.19 is expanded to the lowest order in the secondary's eccentricity as described in Kaula [33].

$$U_2 = \frac{3\mu_1 eR_2^2}{4a_{12}^3}\left(\frac{r}{R_2}\right)^2 \left[\left(1 - 3\cos^2(\phi)\right)\cos(n_2 t) + \sin^2(\phi)\left[3\cos(n_2 t)\cos(2\lambda) + 4\sin(n_2 t)\sin(2\lambda)\right]\right]$$

$$\tag{2.19}$$

Through geophysical models, a linear combination of the k_2 and h_2 Love numbers places bounds on the estimate of the possible ice thicknesses of a planetary satellite with a subsurface ocean [8]. Measurement of these numbers is a primary goal of the JEO mission.

2.2 Equilibrium Points

The RTBP contains five equilibrium points known as Lagrange points. These points are solutions to the equations of motion which remain constant for all time. The dynamics of a system must be time invariant in general to have an equilibrium solution. Therefore, equilibrium points are associated with systems that have a Jacobi integral. Figure 2.2 shows the general location of the five Lagrange points in the plane of a three-body system. The L_4 and L_5 points are located at the points of equilateral triangles formed between the primary and secondary, represented by the orange stars. The collinear Lagrange points L_1, L_2, and L_3 are shown as green stars along the extension of the line connecting the primary and secondary.
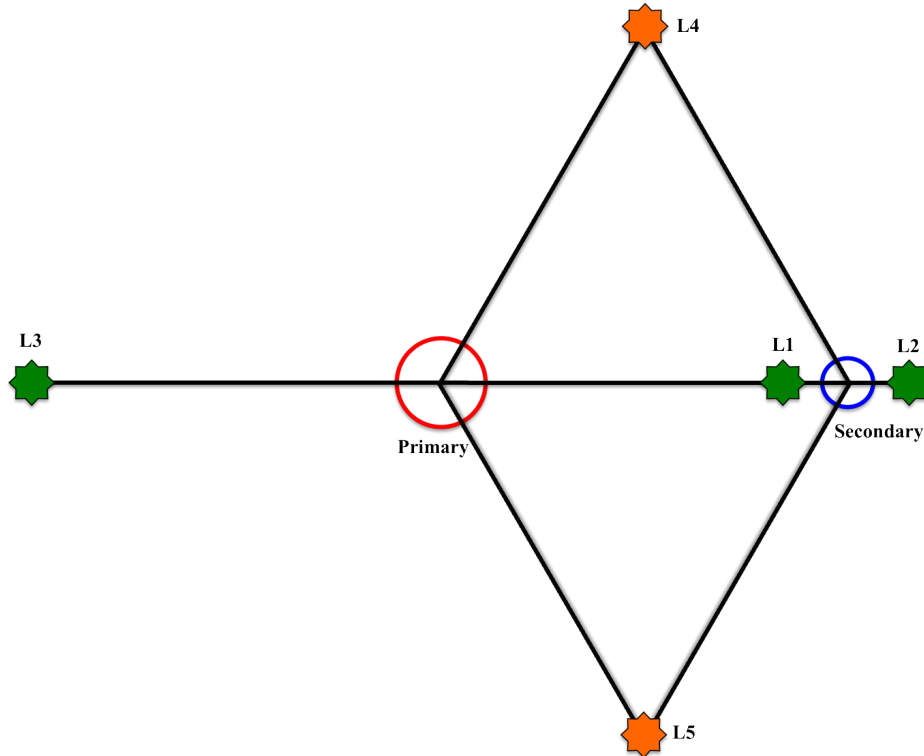
Figure 2.2: Schematic of Lagrange points in RTBP

The equilibrium points of most interest involving planetary satellite orbiters are the collinear Lagrange points L_1 and L_2. The locations of these points are obtained by setting all time derivatives to zero and solving the x scalar equation of motion. This requires $y = z = 0$ and velocity components equal to zero as well. The x values of the collinear points are obtained by solving:

$$(x + 1 - \mu) - (1 - \mu)\frac{x + 1}{r_1^3} - \mu\frac{x}{r_2^3} = 0 \tag{2.20}$$

2.3   Periodic Orbits

Periodic orbits are trajectories which exactly repeat themselves after some specified time period T. Equilibrium points are a special case of periodic orbits with period $T = 0$. Such orbits have the potential to extend orbit lifetime in the unstable environment near planetary satellites such as Europa [18, 20, 21] and Enceladus. Previous studies have found a wealth of periodic orbits in the vicinity of these planetary satellites but few if any are low-altitude, near-polar orbits. This section focuses on the computation of these types of orbits and their properties, since they are desired for geodesy-type missions.

2.3.1   Computation

A search is conducted in the CRTBP for circular, near polar orbits that make an integer number of revolutions N for every orbit of the secondary, such that the period of the orbiter T_{sat} is commensurate with the period T_2 of the secondary's orbit about the primary.

$$\frac{N}{D} = \frac{T_2}{T_{sat}} = \sqrt{\frac{\mu_2\, a_{12}^3}{(\mu_1 + \mu_2)\, a_{sat}^3}} \tag{2.21}$$

Equation 2.21 expresses this number of revolutions N as a function of the orbiter's semi-major axis a_{sat}. Since the primary-secondary semi-major axis a_{12} is fixed, the number of revolutions about the secondary is specified for different values of spacecraft altitude. The process for searching out periodic orbits is as follows. First, generate Cartesian initial conditions of the orbit from the chosen

orbit elements. Searching around the altitude specified by the two-body approximation given above, zero eccentricity, polar orbits are numerically integrated until the required number of revolutions are completed. For near-polar orbits, the xy coordinate plane is taken as a Poincare surface of section and the number of crossings are counted until the desired N value is reached. At the Nth crossing, the spacecraft state and partials of the Jacobi integral are used to differentially correct the initial conditions of the orbit to be more periodic using an algorithm given in Scheeres et al [25]. A visualization of the Poincare map is shown for a Europa orbit in Figure 2.3.
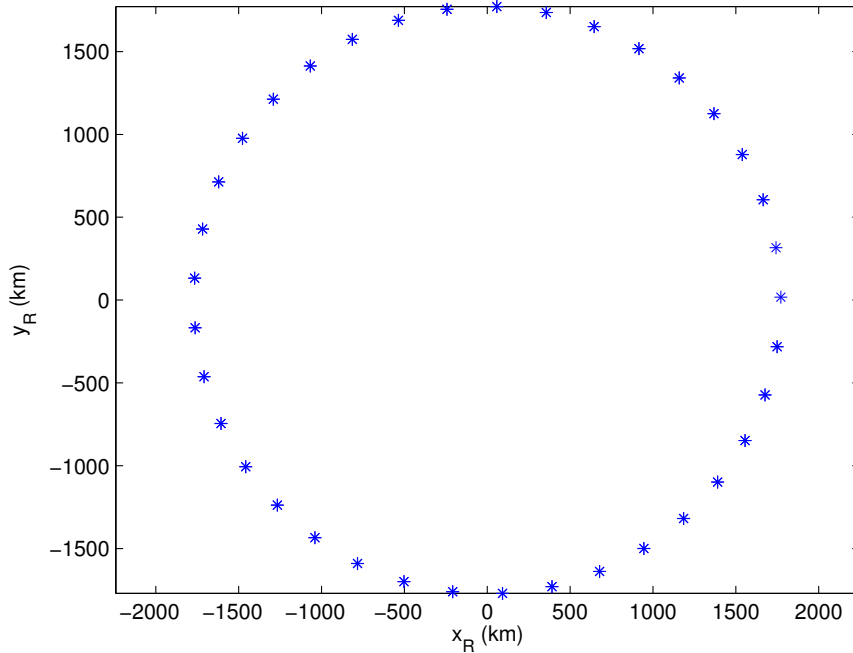
Figure 2.3: $z = 0$ Poincare surface of section for 215 km altitude Europa orbit

The Poincare map is then defined as the discrete mapping of one crossing of $z = 0$ in the positive $\dot{z}$ direction to another. The objective is to match the final surface of section crossing with the initial crossing to form a periodic orbit. The integration of the STM along with the nominal trajectory is necessary to map the full position and velocity state from one crossing to the next. In the case for Europa and Enceladus, the STM will have two unity eigenvalues which form a barrier to the computation of periodic orbits. The monodromy matrix, or the STM evaluated at the system

period time T can be reformulated as a 4x4 matrix with unity eigenvalues removed. This process and the computation of the initial state correction is described below. For the purposes of the orbits given in the paper, the l coordinate used, z, corresponds to $l = 3$. The desired orbit is integrated until the final surface of section crossing and the state dynamics are evaluated at this crossing. The partial derivatives of the Jacobi integral with respect to the state are also required for the computation. The monodromy matrix is formed as follows using the STM evaluated at the periodic time T:

$$M_{ij} = \Phi_{ij}(T) - \frac{\dot{\boldsymbol{X}}_i}{\dot{\boldsymbol{r}}_l(T)} \Phi_{lj}(T) - \frac{1}{\partial J_{l+3}(0)} \left[\Phi_{i,l+3} - \frac{\dot{\boldsymbol{X}}_i(T)}{\dot{\boldsymbol{r}}_l(T)} \Phi_{l,l+3}(T) \right] \frac{\partial J}{\partial \boldsymbol{X}_j}(0) \qquad (2.22)$$

Then, the correction to the initial state in Equation 2.25 is calculated using the difference between the reduced nominal initial state $\boldsymbol{y}_0$ in Equation 2.24 and the reduced final state $\boldsymbol{y}_1$ in Equation 2.23 integrated to the periodic time. The l and $l + 3$ coordinates correspond to z and $\dot{z}$ in these calculations. Thus, they do not appear in the reduced state $\boldsymbol{y}$.

$$\boldsymbol{y}_1 = [x(T) \ y(T) \ \dot{x}(T) \ \dot{y}(T)]^T \qquad (2.23)$$

$$\boldsymbol{y}_0 = [x(0) \ y(0) \ \dot{x}(0) \ \dot{y}(0)]^T \qquad (2.24)$$

$$\delta \boldsymbol{y}_0 = [I_{4x4} - M]^{-1} (\boldsymbol{y}_1 - \boldsymbol{y}_0) \qquad (2.25)$$

The Poincare surface of section constrains the l coordinate z to be zero at the final time. To ensure that the computed state correction maintains the Poincare map, a correction to the $l + 3$ velocity component $\dot{z}$ is computed in the final equation.

$$\delta \dot{\boldsymbol{r}}_l = -\frac{1}{\partial J_{l+3}} \left[\sum_{j=1,\neq l}^{3} \frac{\partial J}{\partial \dot{\boldsymbol{r}}_j} \delta y_0 (2 + j) + \sum_{j=1,\neq l}^{3} \frac{\partial J}{\partial \boldsymbol{r}_j} \delta y_0 (j) \right] \qquad (2.26)$$

These state corrections are applied to the nominal initial conditions and this process is iterated until convergence, which is defined by a user set tolerance of the maximum absolute value of the difference between initial and final states. For the orbits computed in this work, a tolerance of 1 mm in position and 1 mm/sec in velocity was used. The y coordinate is generally the most difficult to converge for the types of orbits examined here, making position the limiting factor for

setting the tolerance. The Europa periodic orbits are also corrected for the effects of Europa's estimated non-spherical gravity field. This involves repeating the differential correction procedure subsequently for the C_{20}, C_{22}, and C_{30} gravity coefficients [15].

2.3.2   Continuation

Periodic orbits are generally isolated at a given level of Jacobi energy. However, neighboring periodic orbits may exist with slightly different Jacobi energies. By incrementing the Jacobi energy in small steps, a family of periodic orbits can be constructed. This process in general will change the eigenvalues and repeat period associated with the periodic orbit. A periodic orbit can also be continued if there exists some other free parameter in the system, such as the μ in the RTBP or C_{22} for a body orbiter. The process for continuing a periodic orbit in Jacobi energy is outlined here.

The function $\boldsymbol{h}$ is a Poincare map. The condition to satisfy for a periodic orbit is:

$$\boldsymbol{y}^{\star} = \boldsymbol{h}\left(\boldsymbol{y}^{\star}, C\right) \tag{2.27}$$

such that the state after one mapping is identical to the initial state, conserving the Jacobi energy. A new periodic orbit is computed by incrementing the Jacobi energy δC while maintaining the Poincare map for the modified state $\boldsymbol{y}^{\star} + \delta \boldsymbol{y}$ such that:

$$\boldsymbol{y}^{\star} + \delta \boldsymbol{y} = \boldsymbol{h}\left(\boldsymbol{y}^{\star} + \delta \boldsymbol{y}, C + \delta C\right) \tag{2.28}$$

The increment in Jacobi constant δC is the control variable and the increment to the reduced state $\delta \boldsymbol{y}$ is derived. Expanding this condition in a Taylor series to first order gives:

$$\boldsymbol{y}^{\star} + \delta \boldsymbol{y} = \boldsymbol{h}\left(\boldsymbol{y}^{\star}, C\right) + \frac{\partial \boldsymbol{h}}{\partial \boldsymbol{y}}\big|^{\star}\delta \boldsymbol{y} + \frac{\partial \boldsymbol{h}}{\partial C}\big|^{\star}\delta C \tag{2.29}$$

where the partial of the Poincare mapping with respect to the state evaluated at the periodic orbit is the monodromy matrix M and the $|^{\star}$ notation represents evaluation on the nominal periodic orbit. Recognizing that $\boldsymbol{y}^{\star} = \boldsymbol{h}\left(\boldsymbol{y}^{\star}, C\right)$ and simplifying:

$$\left[I - M\right]\delta \boldsymbol{y} = \frac{\partial \boldsymbol{h}}{\partial C}\big|^{\star}\delta C \tag{2.30}$$

As long as the matrix $[I - M]$ is invertible, a state correction can be computed to obtain a continued periodic orbit. For periodic orbits about planetary satellites, the monodromy matrix will in general contain unity eigenvalues. Thus, the same reduction procedure as in the differential corrector algorithm is employed to reduce the monodromy matrix to a 4x4 matrix, removing the z and $\dot{z}$ coordinates. The partial of the Poincare map with respect to Jacobi energy is necessary to proceed.

$$\frac{\partial \boldsymbol{h}}{\partial C} = \frac{\partial \boldsymbol{y}_1}{\partial C} = \frac{\partial \boldsymbol{y}_1}{\partial \dot{z}}\frac{\partial \dot{z}}{\partial C} + \frac{\partial \boldsymbol{y}_1}{\partial t}\frac{\delta T}{\delta C} \tag{2.31}$$

Here $\boldsymbol{y}_1$ is the first iteration of the Poincare map over one system time period T, $\frac{\partial \boldsymbol{y}_1}{\partial t}$ is the partial of the state dynamics with respect to time, and δT is the variation in the mapping time to enforce that the state lies on the Poincare surface of section, $z = 0$ in this case. Enforcing the condition:

$$z_1 = \frac{\partial z_1}{\partial C}\delta C + \frac{\partial z_1}{\partial t}\delta T = 0 \tag{2.32}$$

so that the mapped z_1 state lies on the surface of section and

$$\frac{\partial z_1}{\partial C}\delta C = \frac{\partial z_1}{\partial \dot{z}_1}\frac{\partial \dot{z}_1}{\partial C}\delta C = -\dot{z}_1\delta T \tag{2.33}$$

taking the partial of the Jacobi constant with respect to $\dot{z}$,

$$\frac{\partial C}{\partial \dot{z}_1} = -2\dot{z}_1 \tag{2.34}$$

and simplifying gives us an expression for the variation in mapping time δT, where ϕ_{ij} corresponds to the element of the STM in the ith row and jth column.

$$\delta T = \frac{\phi_{36}}{2\dot{z}_1}\frac{1}{\dot{z}_1}\delta C \tag{2.35}$$

For the orbits considered here, the surface of section chosen is $z = 0$, with the corresponding momenta $\dot{z}$ removed in the reduced state. The details are given in Scheeres [31], where the final

computed correction to the reduced state of the nominal periodic orbit is:

$$
\delta \boldsymbol{y} \;=\; [I - M]^{-1} \left(\begin{bmatrix} \phi_{16} \\ \phi_{26} \\ \phi_{46} \\ \phi_{56} \end{bmatrix} - \begin{bmatrix} \dot{x} \\ \dot{y} \\ \ddot{x} \\ \ddot{y} \end{bmatrix} \frac{\phi_{36}}{\dot{z}} \right) \frac{1}{-2\dot{z}} \delta C \tag{2.36}
$$

The continuation $\delta \boldsymbol{y}$ is applied to the initial state, and the resulting state is then input to the differential corrector from the previous section. This process ensures another periodic orbit is the outcome. The properties of continued periodic orbits for the Europa orbiter are discussed in a later section.

2.3.3   Properties of Eigenvectors

Periodic orbits are characterized by the eigenstructure of the STM. The eigenvalues and eigenvectors of the STM determine the stability of a periodic orbit and the behavior of trajectories in the vicinity of the periodic orbit. Before discussing the properties of periodic orbits, it is necessary to present some properties of eigenvectors.

A right eigenvector $\boldsymbol{u}$ is a column vector that satisfies the following property:

$$
\Phi \boldsymbol{u} \;=\; \lambda \boldsymbol{u} \tag{2.37}
$$

where λ is its associated eigenvalue. A left eigenvector $\boldsymbol{v}$ is a row vector which satisfies a similar property:

$$
\boldsymbol{v} \Phi \;=\; \lambda \boldsymbol{v} \tag{2.38}
$$

The STM can be decomposed into matrices of its right eigenvectors V, left eigenvectors U, and eigenvalues L.

$$
\Phi \;=\; ULV^T = \begin{bmatrix} \boldsymbol{u}_1 & \boldsymbol{u}_2 & \cdots & \boldsymbol{u}_n \end{bmatrix} \begin{bmatrix} \lambda_1 & & 0 \\ & \ddots & \\ 0 & & \lambda_n \end{bmatrix} \begin{bmatrix} \boldsymbol{v}_1 \\ \boldsymbol{v}_2 \\ \vdots \\ \boldsymbol{v}_n \end{bmatrix} \tag{2.39}
$$

The sets of right and left eigenvectors are not self-orthogonal but span the STM. A useful property exists between the sets of left and right eigenvectors.

$$\boldsymbol{v}_i \cdot \boldsymbol{u}_j \quad = \quad \begin{cases} 1, & \text{if } i = j. \\ 0, & i \neq j. \end{cases} \tag{2.40}$$

From Equation 2.40, all left eigenvectors are orthogonal to all right eigenvectors except for those pairs generated with the same eigenvalue. Effectively, the set of left eigenvectors is the inverse transpose of the set of right eigenvectors.

$$U \quad = \quad V^{-T} \tag{2.41}$$

2.3.4 Properties of Unstable Periodic Orbits

The STM of a periodic orbit near a planetary satellite will in general have two unity eigenvalues, a conjugate pair of complex eigenvalues, and one eigenvalue each greater than one and less than one. The complex eigenvalues and eigenvectors represent the center manifold of the periodic orbit, the eigenvalue greater than one and its eigenvector represent the unstable manifold, and the eigenvalue less than one and its eigenvector represent the stable manifold. Using the eigenvectors of the State Transition Matrix associated with the stable, unstable, and center manifolds, a set of local dynamic coordinates associated with these manifolds can be constructed [29]. Right eigenvectors control the evolution of trajectories in the vicinity of a periodic orbit forward in time. So, the left eigenvectors of the monodromy matrix (the STM evaluated at the periodic time T) are used in the manifold coordinate decomposition computation due to the orthogonality properties of left and right eigenvectors. The components of an orbiter's state aligned with the right stable, unstable, and center manifolds can be extracted by taking the dot product of the state with the corresponding left eigenvector. Since the left stable eigenvector is orthogonal to every right eigenvector except for the right stable eigenvector, dotting the state with the left stable eigenvector yields only the component aligned with the right stable eigenvector.

The STM is integrated in the rotating frame of the RTBP and evaluated at the system repeat period. Since the Monte Carlo lifetime runs presented later are conducted in the inertial frame for realism, the state must be transformed back to the rotating frame for this computation. The manifold coordinates a_u and a_s representing the unstable and stable components of the state are computed by taking the dot product of the left unstable $\boldsymbol{v}^u$ and left stable $\boldsymbol{v}^s$ eigenvectors with the difference between the dispersed state $\boldsymbol{X}_{disp}$ and the periodic orbit state $\boldsymbol{X}_{PO}$ as in Equations 2.42.

$$
\begin{aligned}
\delta\boldsymbol{x} &= (\boldsymbol{X}_{disp} - \boldsymbol{X}_{PO}) \\
a_u &= \boldsymbol{v}^u \cdot \delta\boldsymbol{x} \\
a_s &= \boldsymbol{v}^s \cdot \delta\boldsymbol{x}
\end{aligned}
\tag{2.42}
$$

The representation of the center manifold includes a magnitude and a phase difference since the center eigenvalues have imaginary components. The center magnitude ρ and center phase γ are computed using the center eigenvector $\boldsymbol{v}_c$ in Equations 2.43.

$$
\begin{aligned}
\boldsymbol{\alpha} &= \text{real}\,(\boldsymbol{v}^c) \\
\boldsymbol{\beta} &= \text{imag}\,(\boldsymbol{v}^c) \\
\rho &= \left[(\delta\boldsymbol{x} \cdot \boldsymbol{\alpha})^2 + (\delta\boldsymbol{x} \cdot \boldsymbol{\beta})^2 \right]^{1/2} \\
\gamma &= \text{atan}\,(\delta\boldsymbol{x} \cdot \boldsymbol{\beta}/\delta\boldsymbol{x} \cdot \boldsymbol{\alpha})
\end{aligned}
\tag{2.43}
$$

The left eigenvectors are normalized to have magnitude one while the orbiter state difference retains it's magnitude. The orbiter states are non-dimensionalized since the STM is integrated using non-dimensional equations of motion. The coordinates themselves are intended to show whether orbits are primarily aligned with the stable or unstable manifolds. The numerical values do not denote how unstable a particular orbit is, more so its relative alignment. The methodology for plotting the computed manifold coordinates is developed in Appendix A.

Chapter 3

Covariance Analysis

One of the motivations for a potential mission to icy planetary moons is to measure the tidal Love numbers, which give insight into the presence of liquid water below the body's surface. In addition to measuring the Love numbers, accurate knowledge of a spacecraft's position and velocity is necessary for any space mission. A covariance analysis is implemented to estimate the accuracy to which the orbiter state, the secondary's extended gravity field, and the Love numbers k_2 and h_2 can be known for this type of mission. The particular implementation is a square-root information filter (SRIF) where the square-root of the information matrix is updated with range-rate and altimetry measurement types. Information is accumulated into the square-root information matrix using an orthogonal transformation known as a Givens rotation. Parameters which affect the estimation process but are not themselves estimated are considered in the Europa covariance computation. The generation of this realistic covariance is critical to the discussion of the lifetime properties of periodic orbits.

3.1   Square-root Information Filter

For a covariance analysis we process no actual observations so a batch processor is sufficient for computing the epoch state covariance matrix. However, there are well known numerical issues with inverting the information matrix at the final step of a batch processor [26]. We use the batch formulation of the Square Root Information Filter (SRIF) such that all information is mapped to the epoch state. The SRIF accumulates the square root information matrix R, where the information

matrix Λ is decomposed as in Eq. 3.1.

$$\Lambda = R^T R \tag{3.1}$$

A batch formulation of the SRIF is used to compute an epoch error covariance associated with the orbiter position and velocity, the extended gravity field coefficients, and the Love numbers. The state vector $\boldsymbol{X}$ is shown in Equation 3.2.

$$\boldsymbol{X} = [\, \boldsymbol{r} \; \boldsymbol{v} \; \mu_2 \; C_{nm} \; S_{nm} \; k_2 \; h_2 \,]^T \tag{3.2}$$

The State Transition matrix (STM) Φ maps small deviations $\delta\boldsymbol{x}$ from the nominal state from time t_0 to time t and controls the local dynamics about an orbit. The STM is used to map all measurement partials back to epoch for addition to the information matrix.

$$\delta\dot{\boldsymbol{x}}\,(t) = \Phi\,(t, t_0)\,\delta\boldsymbol{x}_0 \tag{3.3}$$

The STM is defined as the partial of the estimated state with respect to the initial state.

$$\Phi(t, t_0) = \frac{\partial \boldsymbol{X}(t)}{\partial \boldsymbol{X}(t_0)} \quad A(t) = \frac{\partial \dot{\boldsymbol{X}}(t)}{\partial \boldsymbol{X}(t)} \tag{3.4}$$

The STM Φ is integrated along with the state and is used to map measurement partials back to epoch.

$$\dot{\Phi}(t, t_0) \;=\; A(t)\Phi(t, t_0) \tag{3.5}$$

Equation 3.5 shows the differential equation for the STM which involves the matrix of dynamic partial derivatives A given in Equation 3.4 .

$$\tilde{H}_x = \frac{\partial G(\boldsymbol{X})}{\partial \boldsymbol{X}} \tag{3.6}$$

The observation-mapping matrix $\tilde{H}_x$ is formed by taking the partial derivatives of the measurements $G(\boldsymbol{X})$ used with respect to the state. These measurement partials are mapped to the simulation epoch t_0 by postmultiplying by the STM, weighted by premultiplying with the square-root of the observation weighting matrix W, and then accumulated in the SRIF procedure.

$$H_x\,(t) = W^{1/2}\tilde{H}_x\,(t)\,\Phi\,(t, t_k) \tag{3.7}$$

A Cholesky decomposition is applied to the a priori covariance matrix $\bar{P}_x$, to form the initial square root matrix $\bar{R}_x$. The square root information matrix is accumulated by an orthogonal transformation T such as the Givens transformation used here. This transformation is applied at each measurement update step.

$$\text{Chol}\left(\bar{P}_x^{-1}\right) \;=\; \bar{R}_x \tag{3.8}$$

$$T \begin{bmatrix} \bar{R}_x \\ H_x \end{bmatrix} \;=\; \begin{bmatrix} \hat{R}_x \\ 0 \end{bmatrix} \tag{3.9}$$

All information from the measurement partial is accumulated into the square-root information matrix. This matrix $\hat{R}_x$ is used to compute the final covariance after all measurements are processed.

$$P_x = \hat{R}_x^{-1} \hat{R}_x^{-T} \tag{3.10}$$

The details of the measurement models and the additional contribution of the consider parameters to the information accumulation process are described in the following section.

3.2   Measurement Types

The measurement types used in this covariance analysis are Earth-centered range-rate and nadir-pointing Europa altimetry.

$$\dot{\rho} = \frac{(\boldsymbol{r} + \boldsymbol{R}_{EE}) \cdot (\boldsymbol{v} + \boldsymbol{V}_{EE})}{\sqrt{(\boldsymbol{r} + \boldsymbol{R}_{EE}) \cdot (\boldsymbol{r} + \boldsymbol{R}_{EE})}} \tag{3.11}$$

The range-rate measurement assumes that Earth is in the direction of the negative x axis for the duration of the simulation, where $\boldsymbol{R}_{EE}$ and $\boldsymbol{V}_{EE}$ are the Earth position and velocity vectors with respect to Europa or Enceladus. The standard accuracy of $0.1\sqrt{\Delta t/60\text{s}}$ mm/s for Doppler measurements is used, with measurement partials accumulated every minute in eight hour arcs, representing access to one Deep Space Network antenna. For range-rate, the measurement partials with respect to orbiter position and velocity become:

$$\frac{d\dot{\rho}}{d\,(\boldsymbol{r},\boldsymbol{v})} = \left[\left[\frac{I}{\rho} - \frac{\hat{\rho}\hat{\rho}^T}{\rho}\right](\boldsymbol{v} + \boldsymbol{V}_{EE}) \quad \hat{\boldsymbol{R}}_{EE} \right] \tag{3.12}$$

where $\rho = \sqrt{(\boldsymbol{r} + \boldsymbol{R}_{EE}) \cdot (\boldsymbol{r} + \boldsymbol{R}_{EE})}$. Partials of range-rate with respect to the remaining state entries are zero. However, information on the k_2 Love number is obtained through determining the gravity field. Range-rate tracking gives information on the orbiter position and velocity which allows the filter to fit the gravity field. Fluctuations in the gravity field due to the Love number k_2 are included in the dynamic partials which make up the A matrix. The STM which maps the measurement partials is integrated using the A matrix, and distributes part of the measurement contribution to the k_2 slot in the information matrix.

$$h = |\boldsymbol{r}| - (R_2 + s_R) \tag{3.13}$$

The altimetry measurement in Equation 3.13 includes a time variable surface deformation s_R due to the third body's tidal gravity, where R_2 is the secondary body's radius, and $\boldsymbol{r}$ is the position of the orbiter about the secondary. Altimetry partials are accumulated every 150 seconds with an accuracy of 10 meters. The Love number h_2 is included in the computation of the surface uplift s_R. So, the measurement partial for altimetry becomes [6]:

$$\frac{\partial h}{\partial h_2} = \frac{\partial h}{\partial s_R} \frac{\partial s_R}{\partial h_2} = \frac{-s_R}{h_2} \tag{3.14}$$

with all other state partials equal to zero. In this way, information about the h_2 Love number appears in the information matrix.

3.3   Consider Analysis

Parameters that affect the estimation process but are not themselves estimated can be considered in the filtering process [27]. For the Europa orbiter the following effects are considered: uncertainty in Jupiter's gravitational parameter μ_J, a potential bias in the altimeter measurement Δh, and a potential non-gravitational acceleration a_z constrained to the $\hat{z}$ direction for near-polar orbits. This possible non-gravitational acceleration would be due to the sparse atmosphere [32] on Europa but is not implemented in the dynamics. The gravitational coefficients to degree four are also considered since no reliable estimates of their numerical values are available. These are

represented in the consider state vector in Equation 3.15. The detailed construction of the SRIF covariance analysis can be found in Boone and Scheeres [4].

$$\boldsymbol{C} \quad = \quad [C_{nm}, \; S_{nm}, \; \mu_J, \; a_z \, \Delta h] \tag{3.15}$$

The consider STM ψ is defined in a similar way as the usual STM by taking the partial of the estimated state with respect to the epoch consider state.

$$\psi\left(t, t_0\right) = \frac{\partial \boldsymbol{X}\left(t\right)}{\partial \boldsymbol{C}\left(t_0\right)} \quad B\left(t\right) = \frac{\partial \dot{\boldsymbol{X}}}{\partial \boldsymbol{C}} \tag{3.16}$$

The differential equation for the consider STM, shown in Equation 3.17, takes a slightly different form with an additional B matrix term, the partial of the dynamics with respect to the consider state.

$$\dot{\psi}\left(t, t_0\right) \quad = \quad A\left(t\right) \psi\left(t, t_0\right) + B\left(t\right) \tag{3.17}$$

The consider observation-mapping matrix is formed analogously to the $\tilde{H}_x$ matrix but is not mapped to epoch using the STM.

$$\tilde{H}_c \quad = \quad \frac{\partial G(\boldsymbol{X})}{\partial \boldsymbol{C}} \tag{3.18}$$

$$H_c\left(t\right) \quad = \quad W^{1/2}\left(\tilde{H}_x\left(t\right) \psi\left(t, t_0\right) + \tilde{H}_c\left(t\right)\right) \tag{3.19}$$

A Cholesky decomposition is applied to the full a priori covariance matrix, including the consider covariance contributions to form the initial square-root matrices. The P_{xc} and P_{cx} terms are usually set to zero and the P_{cc} term represents the a priori accuracies of the considered terms. The square-root information matrix is accumulated by an orthogonal transformation T such as a Givens transformation. This transformation is applied at each measurement update step.

$$Chol\left(\begin{bmatrix} \bar{P}_x & \bar{P}_{xc} \\ \bar{P}_{cx} & \bar{P}_{cc} \end{bmatrix}^{-1}\right) = \begin{bmatrix} \bar{R}_x & \bar{R}_{xc} \\ 0 & \bar{R}_c \end{bmatrix} \tag{3.20}$$

$$T\begin{bmatrix} \bar{R}_x & \bar{R}_{xc} \\ H_x & H_c \end{bmatrix} = \begin{bmatrix} \hat{R}_x & \hat{R}_{xc} \\ 0 & \tilde{R}_c \end{bmatrix} \tag{3.21}$$

The usual estimation error covariance P is computed using the accumulated square root information matrix as usual in the SRIF process [26]. The consider covariance matrix P_c is computed using the accumulated square-root information matrix and the sensitivity matrix S shown in Equations 3.22. The final P_c matrix is applied to Europa orbiters in a subsequent chapter.

$$
\begin{aligned}
P &= \hat{R}_x^{-1} \hat{R}_x^{-T} \\
S &= -\hat{R}_x^{-1} \hat{R}_{xc} \\
P_c &= P + S \bar{P}_{cc} S^T
\end{aligned}
\tag{3.22}
$$

The a priori values for the consider parameters are shown in Table 3.1. The first value is taken from the uncertainty in Jupiter's mass and the next two are best estimates based on results from published papers on Galileo data [32]. The uncertainty in the gravitational coefficients comes from an initial seven day SRIF run with coefficients from C_{31} up to C_{40} in the estimate list. The third order and higher Stokes gravity coefficients are not included in the dynamics since numerical estimates are not available. The Stokes coefficients in the covariance analysis are non-dimensionalized using the radius of Europa raised to the power of the coefficient degree n. These parameters are used in the SRIF consider covariance process for constructing covariance matrices for evaluating periodic orbits at Europa.

Table 3.1: Consider a priori uncertainties

Parameter	σ
μ_J (km^3/s^2)	1.001142
a_z (km/s^2)	1×10^{-09}
Δh (m)	100
C_{31}	1.98613×10^{-09}
S_{31}	3.10642×10^{-09}
C_{32}	1.74740×10^{-09}
S_{32}	9.05493×10^{-10}
C_{33}	2.87245×10^{-11}
S_{33}	6.40779×10^{-11}
C_{40}	2.08224×10^{-07}

3.4   Current State SRIF

A current state formulation of the SRIF is used as part of the study of information processing at Europa Lagrange points. In this form, the measurement partial is not mapped in time, but the square-root information matrix is mapped between measurement update times. Since a spacecraft placed at an equilibrium points remains stationary, all time derivatives in the dynamics are zero and the A matrix is constant. This simplifies the filtering process. The STM can be expressed as the matrix exponential of this constant A matrix, eliminating the need to integrate Φ along with the equations of motion.

$$\Phi\left(t_2, t_1\right) = e^{A(t_2 - t_1)} \tag{3.23}$$

The measurement partial is generated as described in the preceding section. The square-root information matrix is mapped between measurement times using the STM as:

$$\bar{R}_x\left(t_2\right) = R_0\left(t_1\right)\Phi^{-1}\left(t_2, t_1\right) \tag{3.24}$$

This measurement partial is then accumulated into this mapped square-root information matrix using an orthogonal transformation.

$$T \begin{bmatrix} \bar{R}_x \\ H_x \end{bmatrix} = \begin{bmatrix} \hat{R}_x \\ 0 \end{bmatrix} \tag{3.25}$$

The covariance matrix P_x for that time is computed as usual.

$$P_x = \hat{R}_x^{-1}\hat{R}_x^{-T} \tag{3.26}$$

The computed square-root information matrix $\hat{R}_x$ then becomes the a priori square-root information matrix for the next measurement accumulation step.

$$R_0 = \hat{R}_x \tag{3.27}$$

Consider parameters are not included for this covariance study at equilibrium points. The following section focuses on how information in the orbit determination process is accumulated along stable and unstable manifolds associated with the Europa L_2 point as an example.

Chapter 4

Information Processing at Equilibrium Points

Equilibrium points are a special case of the periodic orbits discussed earlier. As an introduction to the phase space properties of periodic orbits, equilibrium points are examined because the eigenvectors associated with them, and thus the manifold directions, are constant, simplifying some of the analysis. The collinear Lagrange points at Europa are computed and the L_2 point is chosen for investigation as an example of how the local manifold structure of a periodic orbit affects information accumulation in the orbit determination process. The covariances generated for Europa and Enceladus orbits are affected by the stable and unstable manifolds a similar manner, with the difference being the manifold directions are rotated in time in phase space. Future work in this area will focus on mapping the manifold directions in time using the STM. This analysis is conducted in the xy plane of the Jupiter-Europa three body system.

4.1   Europa Libration Points

For Europa, the reduced mass describing the three body system is $\mu = 2.52802 \cdot 10^{-5}$. To find the locations of the collinear libration points, the x scalar equation of motion is solved, with time derivatives set to zero along with the y and z coordinates set to zero. The roots of Equation 4.1 yield the locations of Europa's L_1, L_2, and L_3 points.

$$(x + 1 - \mu) - (1 - \mu)\frac{x + 1}{|x + 1|^3} - \mu\frac{x}{|x|^3} = 0 \tag{4.1}$$

The x coordinates of the collinear libration points are given in Table 4.1. A spacecraft placed at these locations with zero velocity will remain there indefinitely in the RTBP.

Table 4.1: Europa collinear libration point x coordinates

	x (km)
L_1	$-1.35593 \cdot 10^4$
L_2	$+1.37445 \cdot 10^4$
L_3	$-1.34179 \cdot 10^5$

Since the dynamics are identically zero at an equilibrium point, numerical integration is not necessary. The local dynamics are characterized by the STM which itself is integrated using the dynamic partials matrix A. However, the A matrix is constant since its values depend only on the orbiter position, and an eigenvector of the A matrix is also an eigenvector of the STM. There is a simple relationship between the eigenvalues σ of the A matrix and the eigenvalues λ of the STM.

$$\lambda_i = e^{\sigma_i t} \tag{4.2}$$

So, the eigenstructure of the L_2 equilibrium point is available from the analytical description of the A matrix. Equation 4.3 shows the components of the A matrix and Equation 4.4 gives the partials of the potential

$$A = \begin{bmatrix} 0 & 0 & 1 & 0 \\ 0 & 0 & 0 & 1 \\ U_{xx} & U_{xy} & 0 & 2 \\ U_{yx} & U_{yy} & -2 & 0 \end{bmatrix} \tag{4.3}$$

$$
\begin{aligned}
U_{xx} &= 1 - \frac{1-\mu}{r_J^3} - \frac{\mu}{r_E^3} + 3(1-\mu)\frac{(x+1)^2}{r_J^5} + 3\mu\frac{x^2}{r_E^5} \\
U_{xy} = U_{yx} &= 3\mu\frac{xy}{r_E^5} + 3y(1-\mu)\frac{x+1}{r_J^5} \\
U_{yy} &= 1 - \frac{1-\mu}{r_J^3} - \frac{\mu}{r_E^3} + 3(1-\mu)\frac{y^2}{r_J^5} + 3\mu\frac{y^2}{r_E^5}
\end{aligned} \tag{4.4}
$$

The eigenvectors and eigenvalues are computed from this analytical A matrix using the *eig* command in Matlab. The eigenvalues σ of the A matrix are shown in Table 4.2 to illustrate the instability of L_2. One eigenvalue has magnitude greater than one, corresponding to the unstable manifold, one eigenvalue has magnitude less than zero, corresponding to the stable manifold, and the final two eigenvalues are a complex conjugate pair representing the center manifold.

Table 4.2: Eigenvalues of A matrix for Europa L_2

	Value
λ_u	2.46012
λ_s	-2.46012
λ_{c1}	$0 + 2.04233i$
λ_{c2}	$0 - 2.04233i$

A simplified range-rate model is used to explore the processing of information from measurement partials at this equilibrium point. For the time periods considered in this simulation, Earth's position vector is fixed along the $\hat{u}$ direction in the Jupiter-Europa system. Equation 4.5 shows the range-rate measurement as the dot product of the Earth range direction and the orbiter velocity where T_{RI} is the transformation from the rotating frame to inertial frame.

$$\dot{\rho} = \hat{u} \cdot \boldsymbol{v}_{EE} \quad = \quad \hat{u} \cdot [T_{RI} (\boldsymbol{v}_R + \boldsymbol{\omega} \times \boldsymbol{r}_R)] \tag{4.5}$$

For a spacecraft at an equilibrium point, the rotating frame velocity $\boldsymbol{v}_R$ is zero. Equation 4.6 shows the partial of the range-rate measurement with respect to the rotating frame position and velocity where $\bar{U}$ is the unity dyad and $\tilde{\boldsymbol{\omega}}$ is the cross product matrix of the system angular velocity.

$$\frac{\partial \dot{\rho}}{\partial (\boldsymbol{r}_R, \boldsymbol{v}_R)} = \hat{u} \cdot T_{RI} \left[\tilde{\boldsymbol{\omega}} \, \bar{U} \right] \quad = \quad [1 \, 0 \, 0] \begin{bmatrix} \cos(n_2 t) & -\sin(n_2 t) \\ \sin(n_2 t) & \cos(n_2 t) \end{bmatrix} \left[\tilde{\boldsymbol{\omega}} \, \bar{U} \right] \tag{4.6}$$

This results in a $1x4$ partial since the xy plane is used for the equilibrium point analysis.

$$\frac{\partial \dot{\rho}}{\partial (\boldsymbol{r}_R, \boldsymbol{v}_R)} \quad = \quad [-n_2 \sin(n_2 t) \; -n_2 \cos(n_2 t) \; \cos(n_2 t) \; -\sin(n_2 t)] \tag{4.7}$$

This range-rate measurement partial is accumulated in the SRIF in epoch and current state formulations to explore how the manifolds of the equilibrium point influence the resulting covariance matrix. The following section gives the mathematical basis for the expected behavior of mapped partials.

4.2   Influence of STM Structure on Information Matrix

In a batch formulation of the square-root information filter, the information matrix Λ is updated with each processed measurement via the measurement partials $\tilde{H}$. These measurement partials are mapped to the epoch state by means of the STM which is integrated along with the equations of motion. The update is as follows:

$$\Lambda' \;=\; \Lambda + \Phi^T \left(t, t_0\right) \tilde{H}^T \tilde{H} \Phi \left(t, t_0\right) \tag{4.8}$$

As discussed previously, the STM can be decomposed into a product of matrices of right eigenvectors, left eigenvectors, and a diagonal matrix of eigenvalues.

$$\Phi \;=\; [\boldsymbol{u}] \operatorname{diag}(\lambda) \left[\boldsymbol{v}^T\right] = \begin{bmatrix} \boldsymbol{u}_1 & \boldsymbol{u}_2 & \cdots & \boldsymbol{u}_n \end{bmatrix} \begin{bmatrix} \lambda_1 & & 0 \\ & \ddots & \\ 0 & & \lambda_n \end{bmatrix} \begin{bmatrix} \boldsymbol{v}_1^T \\ \boldsymbol{v}_2^T \\ \vdots \\ \boldsymbol{v}_n^T \end{bmatrix} \tag{4.9}$$

A range-rate measurement partial is decomposed into components along the left eigenvectors of the STM since these vectors span the measurement space. Using a summation to represent the different eigenvector contributions to the partial:

$$\tilde{H} \;=\; \frac{\partial \dot{\rho}}{\partial \left(\boldsymbol{r}_R, \boldsymbol{v}_R\right)} = \sum_{i}^{N} \alpha_i \boldsymbol{v}_i^T \tag{4.10}$$

Decomposing the STM and the measurement partials using the eigenvalues and eigenvectors gives the information matrix update equation in this form:

$$\Lambda' \;=\; \Lambda + \sum_{i}^{N} [\boldsymbol{v}] \operatorname{diag}(\lambda) \left[\boldsymbol{u}^T\right] \left(\alpha_i \boldsymbol{v}_i\right) \left(\alpha_i \boldsymbol{v}_i^T\right) [\boldsymbol{u}] \operatorname{diag}(\lambda) \left[\boldsymbol{v}^T\right] \tag{4.11}$$

where $[\boldsymbol{u}]$ is a matrix of right eigenvectors and $[\boldsymbol{v}]$ is a matrix of left eigenvectors. Using the properties of left and right eigenvectors, this update relationship can be simplified. The dot product of a left eigenvector and right eigenvector is zero unless their indices are equal. In other words, all left and right eigenvectors are orthogonal to one another except for those paired with the same

eigenvalue.

$$\boldsymbol{v}_i \cdot \boldsymbol{u}_j \;=\; \begin{cases} 1, & \text{if } i = j. \\[2mm] 0, & i \neq j. \end{cases} \tag{4.12}$$

Using this property, only the eigenvector(s) aligned with the particular measurement partial will contribute to the addition to the information matrix. The left eigenvectors which make up the measurement partial will select out only their paired right eigenvectors and will dot to zero with all other STM eigenvectors. Using the matrix exponential form of the STM, where σ_i is the eigenvalue of the dynamics partials matrix A corresponding to λ_i:

$$\Lambda' \;=\; \Lambda + \sum_i^N \boldsymbol{v}_i e^{\sigma_i t} \left(\alpha_i \boldsymbol{u}_i^T \boldsymbol{v}_i \right) \left(\alpha_i \boldsymbol{v}_i^T \boldsymbol{u}_i \right) e^{\sigma_i t} \boldsymbol{v}_i^T \tag{4.13}$$

$$\;=\; \Lambda + \sum_i^N \alpha_i^2 e^{2\sigma_i t} \boldsymbol{v}_i \boldsymbol{v}_i^T \tag{4.14}$$

Since the batch formulation of the SRIF references the epoch time, all subsequent measurements will be mapped backward in time. Mapping backward in time along the unstable manifold is expected to decrease uncertainty or increase information content, the opposite of mapping forward in time [23]. Assume the measurement partial in Equation 4.14 is aligned with the unstable left eigenvector, which has a positive real eigenvalue λ greater than one. The natural logarithm of $\lambda_u > 1$ is positive and the measurements aligned with the unstable manifold direction will be mapped according to the exponential $e^{\sigma_u t}$. This will result in an increase in the amount of information in Λ along the left unstable manifold direction greater than any other direction since the exponential mapping will be greatest for the $\lambda_u > 1$ component. Correspondingly, the amount of information increase along the stable manifold direction will be less due to the stable eigenvalue λ_s being less than one. A series of measurements such as range-rate should sample across phase space and not predominantly align with any particular eigenvector. It is not as clear what the effect of STM mapping would be on measurements aligned with a right eigenvector. Returning to Equation 4.11, if the measurement partial is replaced with right eigenvector components:

$$\Lambda' \;=\; \Lambda + \sum_i^N [\boldsymbol{v}] \operatorname{diag}(\lambda) \left[\boldsymbol{u}^T \right] \left(\alpha_i \boldsymbol{u}_i \right) \left(\alpha_i \boldsymbol{u}_i^T \right) [\boldsymbol{u}] \operatorname{diag}(\lambda) \left[\boldsymbol{v}^T \right] \tag{4.15}$$

In this case, the orthogonality properties of left and right eigenvector properties do not simplify the analysis. The measurement partial will generally have nonzero dot products with all of the right eigenvectors in the $[\boldsymbol{u}]$ matrix portion of the STM, leaving no clear direction for enhanced information accumulation.

An analogous result comes out of the mathematics for current state measurement accumulation. In this case, the information matrix is mapped in time between measurement updates. Accumulating a measurement at epoch with no a priori information and then mapping to the next measurement time gives the following, where the mapping relation for the information matrix is the inverse of that for the covariance matrix:

$$\Lambda' = \Phi^{-T}\tilde{H}^T\tilde{H}\Phi^{-1} \tag{4.16}$$

Due to the definition of the STM and the properties of left and right eigenvectors discussed earlier, the inverse of the STM can be expressed as:

$$\Phi^{-1} = [\boldsymbol{u}]\operatorname{diag}(e^{-\sigma t})\left[\boldsymbol{v}^T\right] \tag{4.17}$$

such that the mapped information matrix becomes:

$$\Lambda' = [\boldsymbol{v}]\operatorname{diag}(e^{-\sigma t})\left[\boldsymbol{u}^T\right]\tilde{H}^T\tilde{H}[\boldsymbol{u}]\operatorname{diag}(e^{-\sigma t})\left[\boldsymbol{v}^T\right] \tag{4.18}$$

Since the inverse of the STM is used in mapping the information matrix between update times, the exponential controlling the mapping has a negative sign. This effectively reverses the trends for information accumulation discussed for the epoch state case. If a measurement partial aligned with a left eigenvector is substituted for $\tilde{H}$ in Equation 4.18, the exponential term associated with that eigenvector will have $\sigma > 0$ for the unstable direction or $\sigma < 0$ for the unstable direction. With the negative sign present in the mapping exponential, the left stable direction will accumulate information and reduce uncertainty more than the unstable direction. Again, due to the overall structure of the STM, measurement partials aligned with right eigenvectors do not produce any definite trends for information accumulation. This mapping effect of the STM is expected to

dominate the overall shape of the covariance with respect to the left stable and unstable manifolds. In the following section, experiments are performed to test this hypothesis.

4.3   Covariance Evolution

This section investigates how the covariance accumulated from a series of range-rate measurement partials at the Europa L_2 point evolves in time. The range-rate partial developed in Equation 4.7 is used here. In general, this partial will have projections on to both the left and right eigenvectors. Both the epoch state and current state formulations of a SRIF are used to generate the covariance. A spherical a priori covariance of $1000 \cdot I_{4x4}$ is used for both cases. The focus here is on the evolution of the covariance relative to the manifolds rather than a numerical value. The left and right stable and unstable manifolds are computed for Europa L_2 and the covariance is projected into the plane of intersection of the left stable and unstable manifolds as described in Appendix A.

4.3.1   Epoch State Mapping

Starting from a spherical a priori covariance, range-rate measurement partials are accumulated at the Europa L_2 equilibrium point and an epoch covariance is computed. Partials are accumulated every 10 minutes and an epoch covariance matrix is computed using a SRIF at every time step. Dispersions around the equilibrium point are drawn from the covariance matrix 10000 times and decomposed into manifold coordinates using the methodology in section 2.3.4. The mathematics involving the manifold structure of the STM suggest that there will be reduced uncertainty in this covariance draw along the left unstable manifold direction. In the plots, the left manifolds are plotted as dotted lines and the right manifolds are plotted as solid lines. The stable directions are shown in green and the unstable directions are shown in red. The blue dots each represent one trajectory in the vicinity of the equilibrium points drawn from the covariance. In this way, the relative alignment of the covariance with any particular manifold can be seen.

For epoch accumulation, the times given in the figures represent the last time a measurement
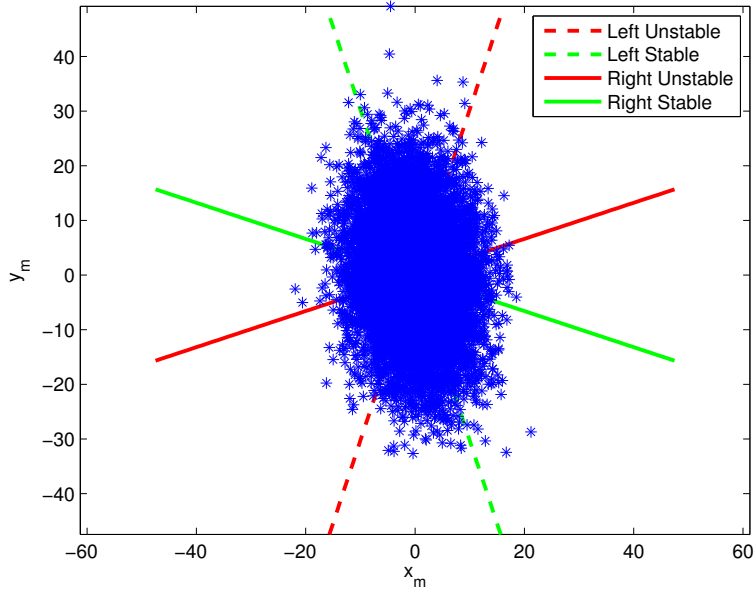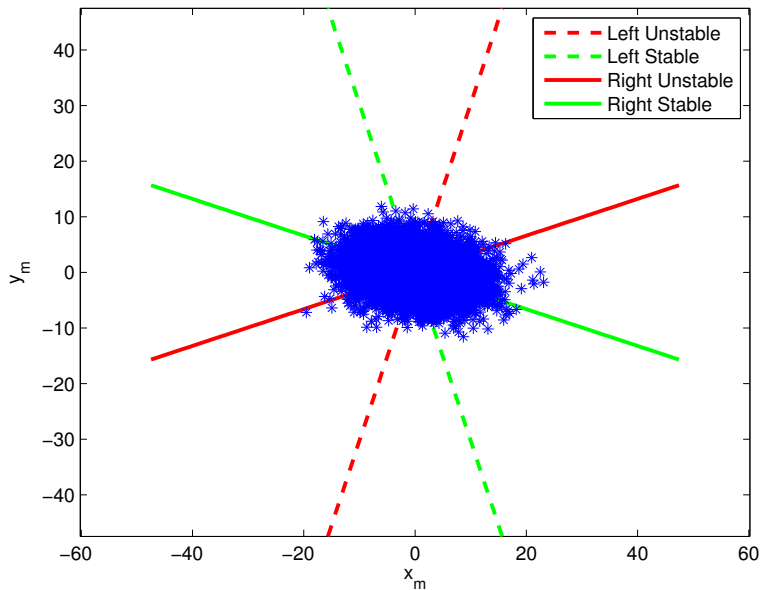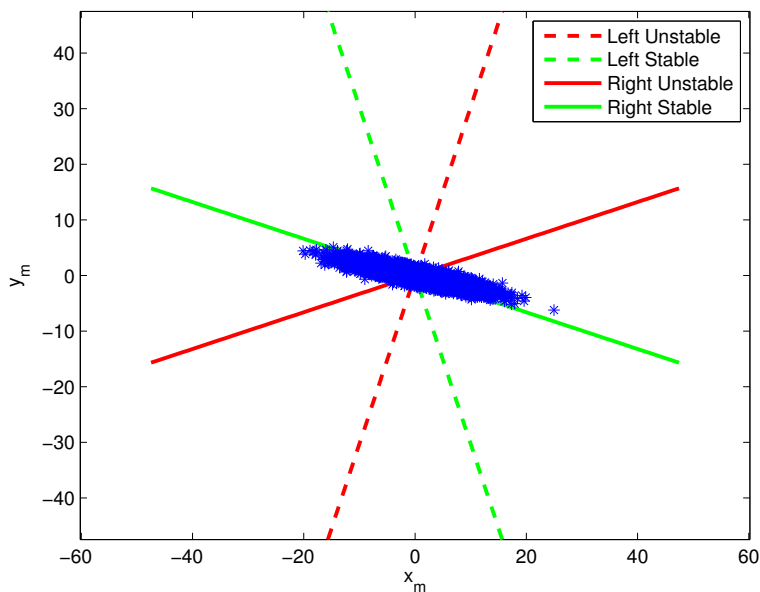
Figure 4.1: Epoch state covariance at $t = 10$ min

partial was accumulated into the information matrix. The specific times shown are chosen for comparison between epoch and current state formulations. All partials are mapped to epoch using the STM. After one measurement partial, the covariance distribution is still nearly spherical as shown in Figure 4.1. After more partials are accumulated, the covariance starts to take on an orientation with the long axis slightly aligned with the right stable manifold as in Figure 4.2. At $t = 300$ minutes in Figure 4.3, the covariance is definitely compressed along the left unstable manifold and has its greatest extent along the right stable manifold.

As the mapping time increases, the effect of the unstable eigenvalue becomes more and more important. Continuing to accumulate partials stretches the covariance even more along the right stable manifold and compresses most along the left unstable direction. Since Earth follows a cyclic pattern in the range-rate model, all eigenvectors of the STM should be sampled equally in this covariance computation. However, the results verify the prediction that the left unstable eigenvector will have the most influence on the epoch covariance. This makes intuitive sense as any errors along the right stable manifold direction would be expected to contract when mapped

Figure 4.2: Epoch state covariance at $t = 50$ min

Figure 4.3: Epoch state covariance at $t = 300$ min

forward in time. With the measurement partials being mapped backward in time for the epoch covariance, errors along the right stable manifold are expanded.

4.3.2 Current State Mapping

Starting from a spherical a priori covariance, range-rate measurement partials are accumu-
lated at the Europa L_2 equilibrium point and a current state covariance is computed. Partials are
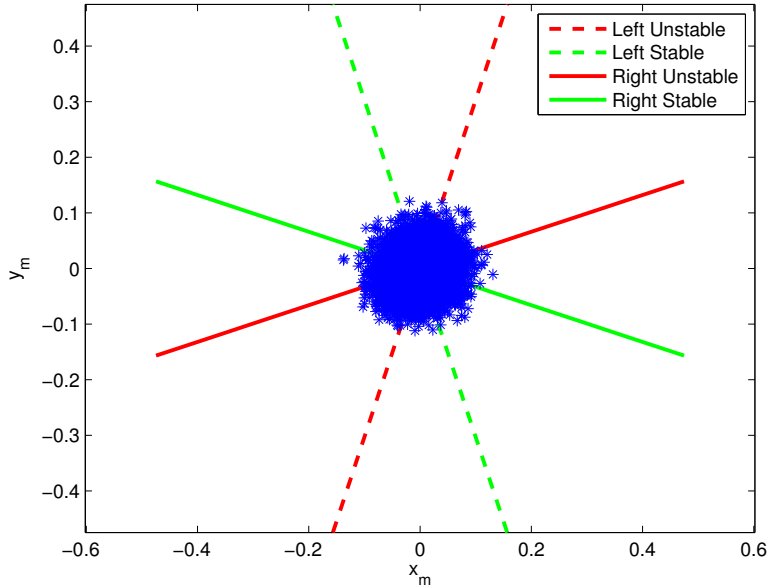accumulated every 10 minutes and the covariance matrix is computed using a current state SRIF.

Figure 4.4: Current state covariance at $t = 10$ min

Dispersions around the equilibrium point are drawn from the covariance matrix 10000 times
and decomposed into manifold coordinates. For the current state formulation, the mathematics
involving the manifold structure of the STM suggest that there will be reduced uncertainty in
this covariance draw along the left stable manifold direction. Figure 4.4 shows the covariance
decomposition after a single measurement has been taken at $t = 10$ minutes. The distribution is
still spherical, but compressed from the a priori since this measurement has not yet been mapped
in any way. For the current state filter, the entire information matrix is mapped between updates
and in this study there was no measurement at epoch.

After mapping the covariance and accumulating additional measurements, the properties of
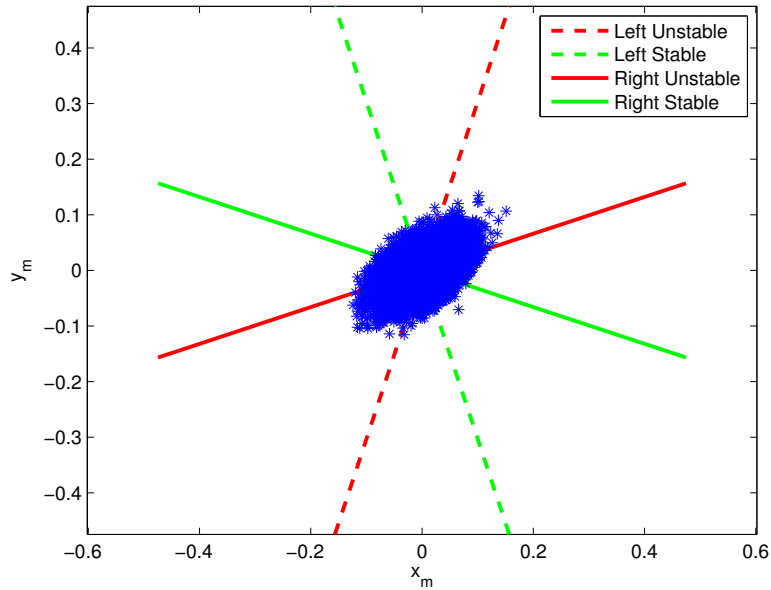the STM mapping begin to manifest in Figure 4.5. The distribution is no longer spherical and

Figure 4.5: Current state covariance at $t = 50$ min

there is some compression along the left stable manifold direction. Each measurement partial adds information and reduces the volume of the uncertainty but the information matrix is also mapped in time between measurement updates, expanding along the direction of the right unstable manifold. This right unstable manifold controls evolution forward in time.

Figure 4.6 shows the covariance being stretched even more along the right unstable manifold and compressing along the left stable manifold. This confirms the mathematical prediction based on the structure of the STM mapping in the SRIF process. The reason for compression along the left stable manifold in this case is due to the negative sign imparted to the exponential mapping in the time update equation for the information matrix. Similar behavior would be expected for covariance analyses conducted around unstable periodic orbits since they possess stable and unstable manifolds. However, the manifold structure for periodic orbits would also have to be mapped in time. Numerical difficulties arise in mapping the manifolds of the monodromy matrix which controls the local dynamics around a periodic orbit. The angle between the stable and unstable manifolds would be constant at each point in the orbit although rotated in phase space.
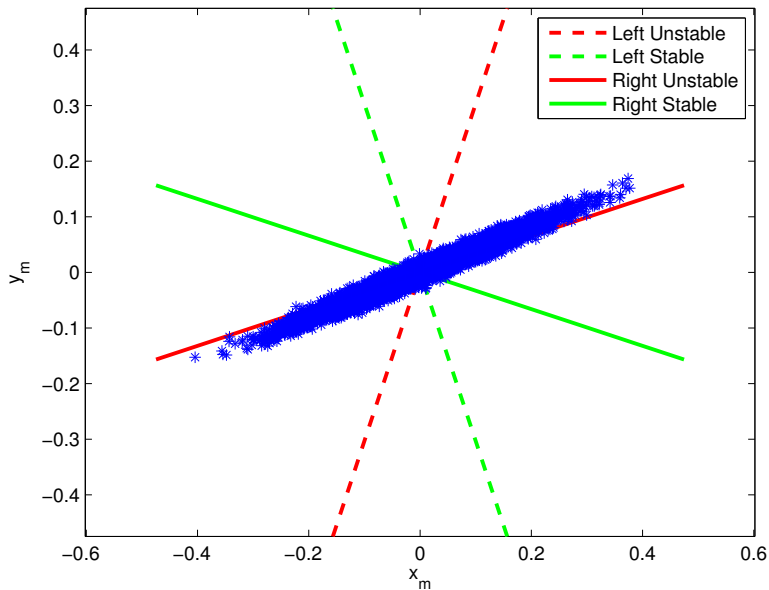
Figure 4.6: Current state covariance at $t = 300$ min

This is difficult to enforce numerically when many applications of the STM would be required for manifold decomposition at many measurement times. A libration point was chosen for this study because of the constant manifold properties. Such a study for periodic orbits may be the subject of future work.

4.4   Information Accessibility via Eigenvector

The previous sections show a dichotomy between how measurements aligned with left and right eigenvectors map in time. For epoch state filtering, the left unstable direction is best known and the right stable direction is least known. For a current state filter, the left stable direction is best known and the right unstable direction is least known. In this section, the possibility of having deficient measurement directions in phase space is explored. For measurements composed of left or right eigenvectors, epoch and current state mapping is examined in more detail to determine if there exists a direction in phase space where no information is available.

4.4.1 Left Eigenvectors

First, a measurement partial composed of left eigenvectors in a two degree of freedom system such as the planar CRTBP is examined under current state filtering, where any of the α_i constants may be zero.

$$\tilde{H} = \sum_{i=1}^{4} \alpha_i \boldsymbol{v}_i = \begin{bmatrix} \alpha_1 & \alpha_2 & \alpha_3 & \alpha_4 \end{bmatrix} \begin{bmatrix} \boldsymbol{v}_1^T \\ \boldsymbol{v}_2^T \\ \boldsymbol{v}_3^T \\ \boldsymbol{v}_4^T \end{bmatrix} = [\alpha] \begin{bmatrix} \boldsymbol{v}^T \end{bmatrix} \tag{4.19}$$

In the absence of a priori uncertainty, the information matrix becomes:

$$\Lambda_0' = \tilde{H}^T \tilde{H} \tag{4.20}$$

The resulting covariance is then mapped forward in time to the next measurement update.

$$\Lambda_1 = \Phi^{-T} \Lambda_0' \Phi^{-1} = \Phi^{-T} \tilde{H}^T \tilde{H} \Phi^{-1} \tag{4.21}$$

The mapping of the measurement partial is simplified due to the orthogonality properties of left and right eigenvectors, $\begin{bmatrix} \boldsymbol{v}^T \end{bmatrix} [\boldsymbol{u}] = I_{4x4}$.

$$\tilde{H}\Phi^{-1} = [\alpha] \begin{bmatrix} \boldsymbol{v}^T \end{bmatrix} [\boldsymbol{u}] \operatorname{diag}(e^{-\sigma t_1}) \begin{bmatrix} \boldsymbol{v}^T \end{bmatrix} = [\alpha] \operatorname{diag}(e^{-\sigma t_1}) \begin{bmatrix} \boldsymbol{v}^T \end{bmatrix} \tag{4.22}$$

Substituting the relation in Equation 4.22 and its transpose into Equation 4.21 gives:

$$\Lambda_1 = \left(\tilde{H}\Phi^{-1} \right)^T \left(\tilde{H}\Phi^{-1} \right) = [\boldsymbol{v}] \operatorname{diag}(e^{-\sigma t_1}) [\alpha]^T [\alpha] \operatorname{diag}(e^{-\sigma t_1}) \begin{bmatrix} \boldsymbol{v}^T \end{bmatrix} \tag{4.23}$$

The product of α coefficients becomes a matrix of products.

$$[\alpha]^T [\alpha] = \begin{bmatrix} \alpha_1\alpha_1 & \alpha_1\alpha_2 & \alpha_1\alpha_3 & \alpha_1\alpha_4 \\ \alpha_2\alpha_1 & \alpha_2\alpha_2 & \alpha_2\alpha_3 & \alpha_2\alpha_4 \\ \alpha_3\alpha_1 & \alpha_3\alpha_2 & \alpha_3\alpha_3 & \alpha_3\alpha_4 \\ \alpha_4\alpha_1 & \alpha_4\alpha_2 & \alpha_4\alpha_3 & \alpha_4\alpha_4 \end{bmatrix} \tag{4.24}$$

If a given measurement has no component along a particular eigenvector direction, the corresponding row and column of this matrix are zero. For example, if $\alpha_1 = 0$,

$$[\alpha]^T [\alpha] = \begin{bmatrix} 0 & 0 & 0 & 0 \\ 0 & \alpha_2\alpha_2 & \alpha_2\alpha_3 & \alpha_2\alpha_4 \\ 0 & \alpha_3\alpha_2 & \alpha_3\alpha_3 & \alpha_3\alpha_4 \\ 0 & \alpha_4\alpha_2 & \alpha_4\alpha_3 & \alpha_4\alpha_4 \end{bmatrix} \tag{4.25}$$

The update to the information matrix then becomes,

$$\left(\tilde{H}\Phi^{-1}\right)^T \left(\tilde{H}\Phi^{-1}\right) = \left[e^{-\sigma t_1}\boldsymbol{v}\right] \begin{bmatrix} 0 & 0 & 0 & 0 \\ 0 & \alpha_2\alpha_2 & \alpha_2\alpha_3 & \alpha_2\alpha_4 \\ 0 & \alpha_3\alpha_2 & \alpha_3\alpha_3 & \alpha_3\alpha_4 \\ 0 & \alpha_4\alpha_2 & \alpha_4\alpha_3 & \alpha_4\alpha_4 \end{bmatrix} \left[e^{-\sigma t_1}\boldsymbol{v}^T\right] \tag{4.26}$$

which results in,

$$\left(\tilde{H}\Phi^{-1}\right)^T \left(\tilde{H}\Phi^{-1}\right) = 0_{4x4} + Ae^{-\sigma_2 t_1}\boldsymbol{v}_2^T + Be^{-\sigma_3 t_1}\boldsymbol{v}_3^T + Ce^{-\sigma_4 t_1}\boldsymbol{v}_4^T \tag{4.27}$$

where the terms A, B, and C are linear combinations of $\boldsymbol{v}_2$, $\boldsymbol{v}_3$, and $\boldsymbol{v}_4$ mapped by the exponential of their corresponding eigenvector and multiplied by the constant α_i as follows:

$$
\begin{aligned}
A &= \alpha_2^2 e^{-\sigma_2 t_1}\boldsymbol{v}_2 + \alpha_2\alpha_3 e^{-\sigma_3 t_1}\boldsymbol{v}_3 + \alpha_2\alpha_4 e^{-\sigma_4 t_1}\boldsymbol{v}_4 \\
B &= \alpha_2\alpha_3 e^{-\sigma_2 t_1}\boldsymbol{v}_2 + \alpha_3^2 e^{-\sigma_3 t_1}\boldsymbol{v}_3 + \alpha_3\alpha_4 e^{-\sigma_4 t_1}\boldsymbol{v}_4 \\
C &= \alpha_2\alpha_4 e^{-\sigma_2 t_1}\boldsymbol{v}_2 + \alpha_3\alpha_4 e^{-\sigma_3 t_1}\boldsymbol{v}_3 + \alpha_4^2 e^{-\sigma_4 t_1}\boldsymbol{v}_4
\end{aligned}
\tag{4.28}
$$

In this example, there are no terms in this measurement update containing $\boldsymbol{v}_1$. However, the left eigenvectors are not self-orthogonal, and there may be some information along the $\boldsymbol{v}_1$ direction in phase space. The right eigenvector $\boldsymbol{u}_1$ dotted with this update to the information matrix will produce a zero result since the only vectors present are those which do not share an eigenvalue with $\boldsymbol{u}_1$. In other words, no information is present along the $\boldsymbol{u}_1$ direction because the measurement partial does not contain $\boldsymbol{v}_1$. This is verified numerically by constructing a measurement partial out of

the stable, and two center manifolds of the Europa L_2 point but omitting the unstable component. The result of mapping the information update to a subsequent time and dotting with the right unstable eigenvector is identically zero. This means that a series of measurements deficient in any left eigenvector direction will never have information along the paired right eigenvector direction in phase space, even under mapping in time.

If measurement partials composed of left eigenvectors are accumulated at epoch a similar result is found. Modifying Equation 4.11 for current state mapping:

$$\Lambda_1 = \Phi^T \tilde{H}^T \tilde{H} \Phi \quad = \quad [\boldsymbol{v}] \operatorname{diag}(e^{\sigma t_1}) [\boldsymbol{u}^T] [\boldsymbol{v}] [\alpha]^T [\alpha] [\boldsymbol{v}^T] [\boldsymbol{u}] \operatorname{diag}(e^{\sigma t_1}) [\boldsymbol{v}^T] \qquad (4.29)$$

Again, this is simplified using the orthogonality properties of left and right eigenvectors.

$$\Lambda_1 = \Phi^T \tilde{H}^T \tilde{H} \Phi \quad = \quad [\boldsymbol{v}] \operatorname{diag}(e^{\sigma t_1}) [\alpha]^T [\alpha] \operatorname{diag}(e^{\sigma t_1}) [\boldsymbol{v}^T] \qquad (4.30)$$

The only difference between Equation 4.30 and Equation 4.23 is the negative sign in matrix of exponential terms. Working through the math results in the same outcome as for the current state formulation in terms of information accessibility. If any left eigenvector was not a component of the measurement partial, then the direction of the right eigenvector paired with the missing left will contain no information. This is again verified by numerical experiment by constructing a left eigenvector measurement partial with one left omitted. The dot product of the information update mapped to epoch and dotted with the right eigenvector corresponding to the omitted left is zero.

4.4.2   Right Eigenvectors

A different strategy is taken with measurements composed of right eigenvectors since the structure of the STM does not yield simplifications in the information update. To determine whether there are directions in phase space deficient in information due to right eigenvector measurement partials, a series of measurements composed of the same right eigenvector are accumulated

and mapped in time. Using a range-rate partial composed of a single right eigenvector:

$$\tilde{H} \;=\; \frac{\partial \dot{\rho}}{\partial\left(\boldsymbol{r}_R, \boldsymbol{v}_R\right)} = \alpha \boldsymbol{u}^T \tag{4.31}$$

A series of identical partials described in Equation 4.31 are accumulated into the information matrix, which is mapped forward in time between measurement updates. For current state accumulation the inverse of the STM is used and the partials are mapped according to Equation 4.32 and its transpose.

$$\tilde{H}\Phi^{-1} \;=\; \alpha \boldsymbol{u}^T \left[\boldsymbol{u}\right] \operatorname{diag}(e^{-\sigma t}) \left[\boldsymbol{v}^T\right] \tag{4.32}$$

Here the measurement partial composed of a single right eigenvector will have nonzero dot products with the matrix of right eigenvectors in the decomposition of the STM. The same measurement partial constructed from a right eigenvector is used for each $\tilde{H}$ in Equations 4.33 through 4.36.

$$\Lambda_1 \;=\; \tilde{H}^T \tilde{H} \tag{4.33}$$

$$\Lambda_2 \;=\; \Phi^{-T}\Lambda_1\Phi^{-1} + \tilde{H}^T \tilde{H} \tag{4.34}$$

$$\Lambda_3 \;=\; \Phi^{-T}\Lambda_2\Phi^{-1} + \tilde{H}^T \tilde{H} \tag{4.35}$$

$$\Lambda_4 \;=\; \Phi^{-T}\Lambda_3\Phi^{-1} + \tilde{H}^T \tilde{H} \tag{4.36}$$

The rank of the resulting information matrices are examined and the same dot product tests as were administered to the left eigenvector accumulations are applied. The ranks of the resulting information matrices are $rank(\Lambda_1) = 1$, $rank(\Lambda_2) = 2$, $rank(\Lambda_3) = 3$, and $rank(\Lambda_4) = 4$. For the two degree of freedom system in the plane at Europa L_2, the final information matrix has full rank. This shows that measurements composed of right eigenvectors are rotated in phase space due to the properties of the STM. Taking the dot product of the final Λ_4 information matrix with each left eigenvector $\boldsymbol{v}$ gives a nonzero result. There is no information deficient phase space direction in terms of eigenvectors resulting from this process. This property is not true for a series of measurements constructed from a left eigenvector. Each information matrix in that case would have $rank(\Lambda_i) = 1$

due to the orthogonality properties of left and right eigenvectors. Repeating this process for epoch mapping of a series of the same right eigenvector measurements yields similar results.

$$\tilde{H}\Phi \;\; = \;\; \alpha \boldsymbol{u}^T \left[\boldsymbol{u}\right] \operatorname{diag}(e^{\sigma t}) \left[\boldsymbol{v}^T\right] \tag{4.37}$$

In this case, each measurement partial is mapped to epoch using Equation 4.37 and its transpose. Again, the measurement partial composed of a single right eigenvector will have nonzero dot products with the matrix of right eigenvectors in the STM decomposition.

$$\Lambda_1 \;\; = \;\; \Phi^T \tilde{H}^T \tilde{H} \Phi \tag{4.38}$$

$$\Lambda_2 \;\; = \;\; \Lambda_1 + \Phi^T \tilde{H}^T \tilde{H} \Phi \tag{4.39}$$

$$\Lambda_3 \;\; = \;\; \Lambda_2 + \Phi^T \tilde{H}^T \tilde{H} \Phi \tag{4.40}$$

$$\Lambda_4 \;\; = \;\; \Lambda_3 + \Phi^T \tilde{H}^T \tilde{H} \Phi \tag{4.41}$$

The final information matrix Λ_4 is full rank. Dotting the final information matrix with any of the left eigenvectors $\boldsymbol{v}$ gives a nonzero result. Accumulating a series of the same measurement allows determination of the full state due to the STM mapping properties. At an equilibrium point, working in four dimensions, it may be possible to construct a measurement perpendicular to the position components of a center manifold. If measurements are taken in that direction, the full state in the rotating frame can never be obtained. The measurement will lie along the other three eigenvectors in general but the resulting information matrix would be singular.

Chapter 5

Europa Orbiters

In this chapter, Europa periodic orbits are investigated as a means for extending orbit lifetime in the unstable environment of the Jupiter-Europa system. Periodic orbits are computed in the RTBP and corrected to be periodic with the effects of Europa's extended gravity field. The values of the Jupiter-Europa system parameters are given in Table 5.1. The nonzero Stokes coefficients [16] used in these simulations have been non-dimensionalized by Europa's radius raised to the n power, the coefficient degree.

Table 5.1: Jupiter-Europa system parameters

Parameter	Value
R_E (km)	1560.8
e_E	0.0094
n_E (rad/s)	$2.048 \cdot 10^{-5}$
T_E (days)	3.55
LU (km)	$6.709 \cdot 10^5$
TU (s)	$4.882 \cdot 10^4$
μ_E (km^3/s^2)	$3.20273 \cdot 10^3$
μ_J (km^3/s^2)	$1.26686 \cdot 10^8$
C_{20}	$-4.2748 \cdot 10^{-4}$
C_{22}	$1.2847 \cdot 10^{-4}$
C_{30}	$-1.3784 \cdot 10^{-4}$

A consider covariance analysis is conducted about a nominal periodic orbit to obtain estimation state uncertainties for the orbiter position and velocity, Europa's gravitational coefficients, and the tidal Love numbers. This covariance is used to disperse the nominal orbit in a Monte Carlo simulation which reveals a bias toward longer lifetime orbits. The phase space structure of

these orbits is examined through the application of manifold coordinates. The realistic covariance is shown to be influenced by the structure of the stable and unstable manifolds of the nominal periodic orbit. This manifold structure is shown to be sensitive to changes in system initial conditions, specifically the initial position of Jupiter. The nominal periodic orbit is continued to form a family of periodic orbits, all of which have similar manifold structures. This shows that the covariance is not controlled by one particular periodic orbit. The Monte Carlo simulations are iterated by applying the nominal covariance to the long-lifetime orbits computed from the scaled covariance draws. This increases the maximum orbit lifetimes found in the distribution by a factor of three over the nominal lifetime. As a check on numerical accuracy, orbits are constructed from dispersions along the stable manifold. The lifetimes of these orbits are comparable but less than the longest lifetime orbit found in the covariance draw.

5.1   Europa Periodic Orbits

Periodic orbits are computed using the differential corrector algorithm discussed in Section 2.3.1. Figure 5.1 below shows the number of Europa revolutions of the orbiter as a function of the orbit altitude given by Equation 2.21. The altitude currently under consideration by JEO for a Europa orbiter is 100 km, which corresponds to $N = 41$ in the commensurate period approximation.

The periodic orbits in this study are converged in the Europa-centered rotating frame with the effects of the higher order Europa gravity terms. The CRTBP form of the equations of motion is non-dimensionalized using the length (LU) and time (TU) units given in Table 5.1. The final fully converged orbit represented by the orbit elements in Table 5.2 is used for the covariance analysis and Monte Carlo simulation detailed in the following section. The variation in the two-body orbit elements a, e, i, Ω, ω, and M for this periodic orbit are shown over one Europa orbit period in Figures 5.4, 5.5, and 5.6.

The eigenvalues in Table 5.2 are computed from the full STM evaluated at Europa's repeat period. The eigenvalues $\lambda_u > 1$ and $\lambda_s < 1$ show that the orbit is fundamentally unstable with λ_u representing the unstable manifold and λ_s representing the stable manifold. The complex pair of

Table 5.2: Two-body elements and eigenvalues for 97 km altitude periodic orbit

Parameter	Value
a (km)	1658.31
e	0.026917
i (deg)	90.794
Ω (deg)	0.070868
ω (deg)	274.653
M (deg)	82.277
λ_u	1.29157
λ_s	0.774249
λ_{c1}	$0.99999998 + 0.000186358i$
λ_{c2}	$0.99999998 - 0.000186358i$
λ_1	0.999763
λ_1	1.00024
θ (deg)	60.4064
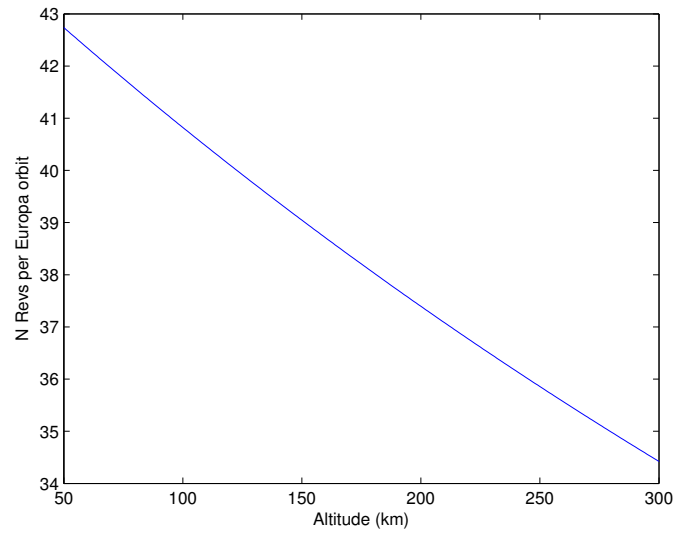
Figure 5.1: Number of xy-plane crossings N per Europa orbit
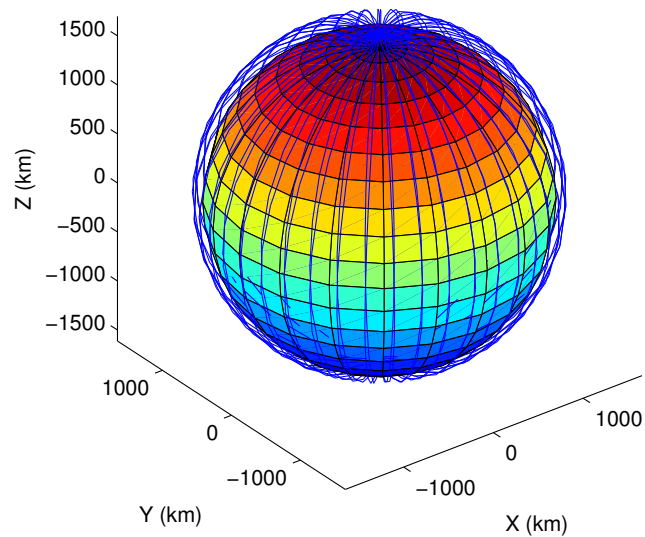
Figure 5.2: Europa 97 km altitude periodic orbit

eigenvalues represent the center manifold and the final eigenvalues are numerically unity, indicating

that the orbit is a fixed point in the RTBP. The first unity eigenvalue represents invariance when
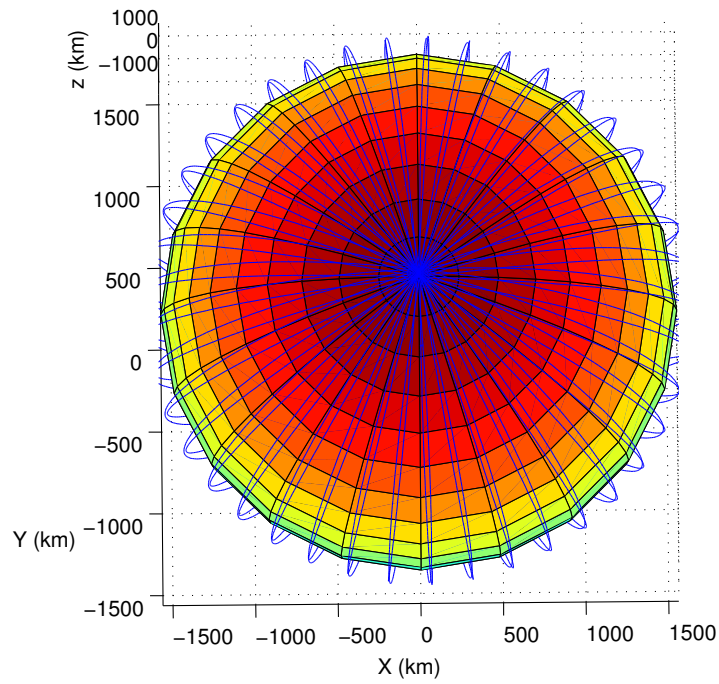
Figure 5.3: Europa 97 km altitude periodic orbit - top view
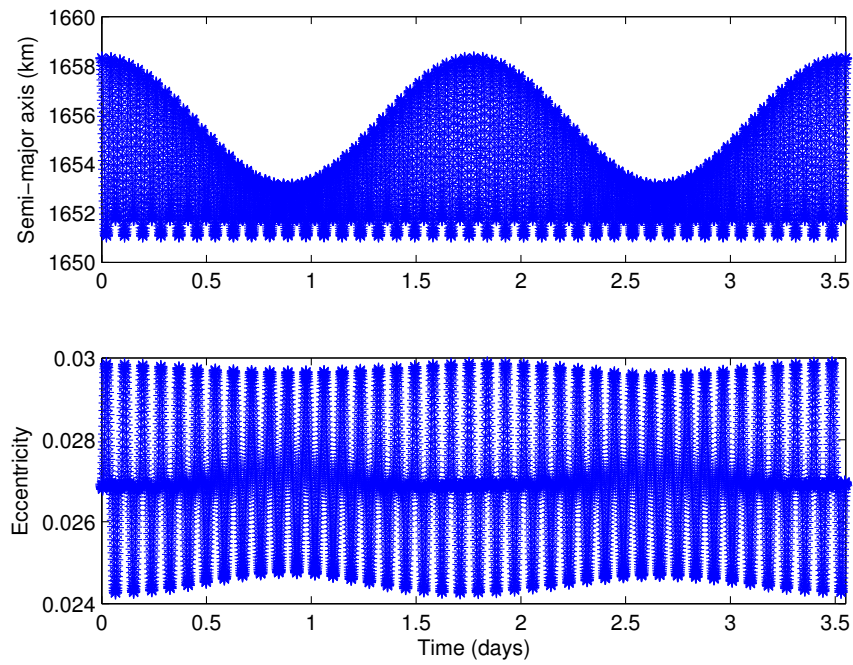
Figure 5.4: Semi-major axis and eccentricity for 97 km over one system repeat period
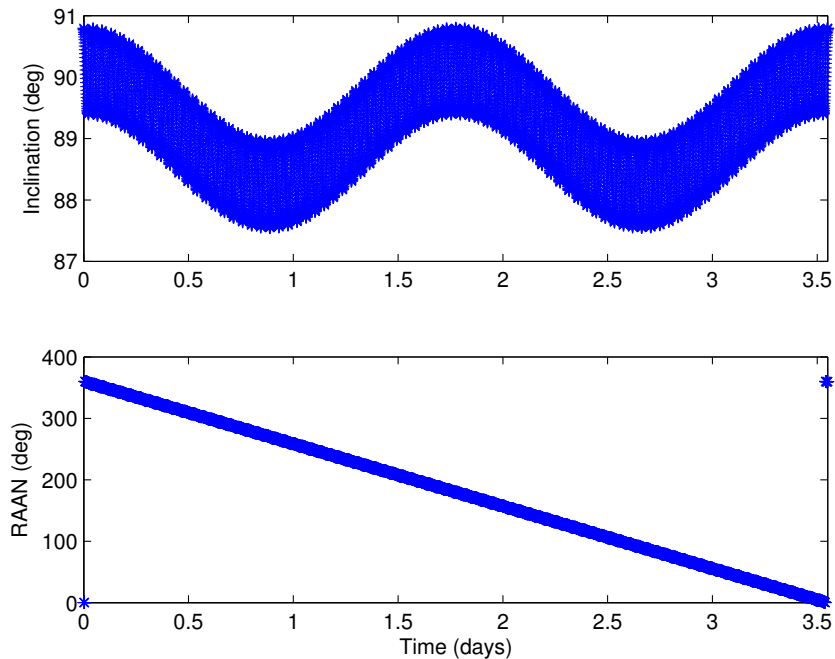
Figure 5.5: Inclination and RAAN for 97 km over one system repeat period
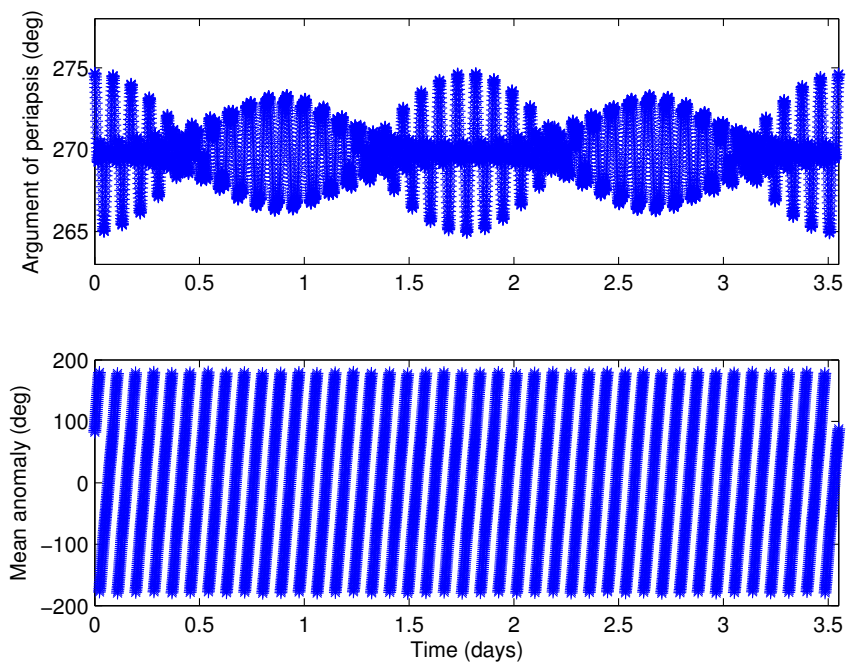
Figure 5.6: Argument of periapsis and mean anomaly for 97 km over one system repeat period

moving along the periodic orbit and the second unity eigenvalue is due to the existence of the Jacobi integral in the RTBP. The manifold structure described above is valid only for this particular nominal periodic orbit; however, multiple periodic orbits will reside in the vicinity of this orbit in phase space. This orbit is continued into a family of periodic orbits for analysis in the manifold decomposition in Section 5.4.

5.2   Covariance Results

Table 5.3 shows the 1σ state accuracies for a seven day SRIF covariance run. The position accuracies are on the order of meters and the velocity accuracies are on the order of mm/s. These accuracies may be challenging to realize for an outer planet type mission. The gravity field coefficients are very well known with uncertainties four orders of magnitude smaller than the actual non-dimensionalized values used in the dynamics.

Table 5.3: 97 km altitude Europa periodic orbit initial state uncertainties

x (km)	1.402×10^{-04}
y (km)	3.952×10^{-03}
z (km)	3.649×10^{-03}
u (km/s)	2.502×10^{-06}
v (km/s)	5.693×10^{-07}
w (km/s)	2.594×10^{-07}
μ_E (km^3/s^2)	1.230×10^{-04}
C_{20}	6.965×10^{-08}
C_{21}	6.141×10^{-08}
S_{21}	1.273×10^{-08}
C_{22}	1.473×10^{-09}
S_{22}	2.842×10^{-10}
C_{30}	4.062×10^{-06}
k_2	1.330×10^{-06}
h_2	2.536×10^{-02}

Figure 5.7 shows the covariance envelope for the Love numbers k_2 and h_2. The flat portions in the k_2 evolution represent time periods where range-rate measurements are not accumulated. The k_2 Love number is tied to fluctuations in Europa's gravity field, and the range-rate measurement partials give information on the orbiter position and velocity, and thus the gravity field. The Love number accuracies vary from those reported in other published results due to differences in
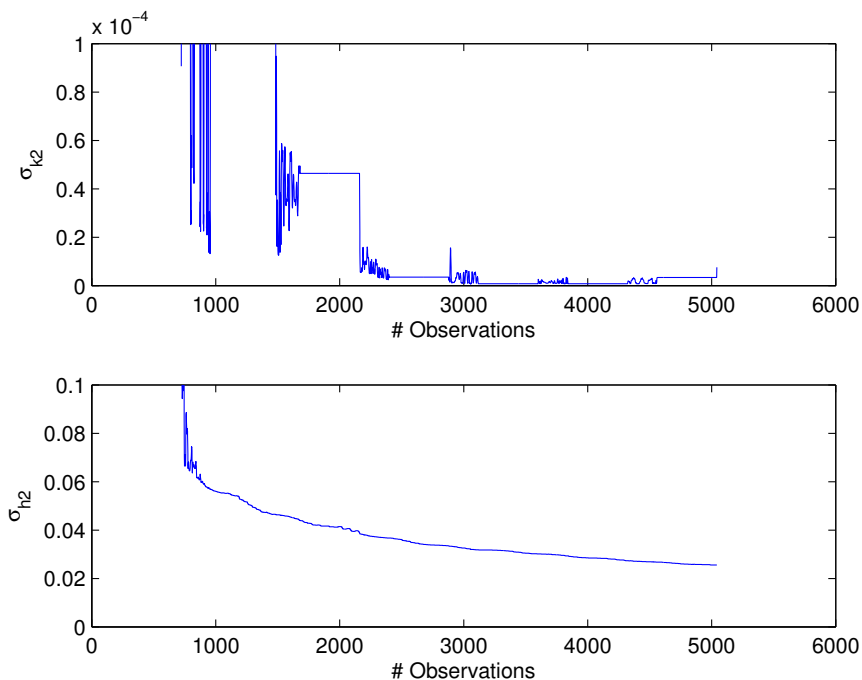
Figure 5.7: Consider covariance envelope accumulated over seven days

simulation time and dynamics models. The Love number accuracy for k_2 computed here, which has a nominal value of 0.25 in this simulation, is more accurate than the 0.0004 accuracy reported in Wu et al. The h_2 accuracy, which has a nominal value of 1.25 in this simulation, is not accurate enough per NASA objectives. Altimeter crossover measurements may improve this performance by removing orbital errors and capturing time-varying topography [35].

5.3   Monte Carlo Lifetime Simulation

To evaluate the statistical properties of an orbit's lifetime, the initial position and velocity of the orbit are dispersed by drawing a random vector from the multivariate normal distribution with zero mean and covariance specified by the output of the consider covariance analysis. This process is repeated in a Monte Carlo simulation 10000 times and the time to impact along with the integrated spacecraft state are saved for each run. Figure 5.8 shows the eventual decay of the radius magnitude of the nominal 97 km altitude periodic orbit, yielding an 83.3 day lifetime.
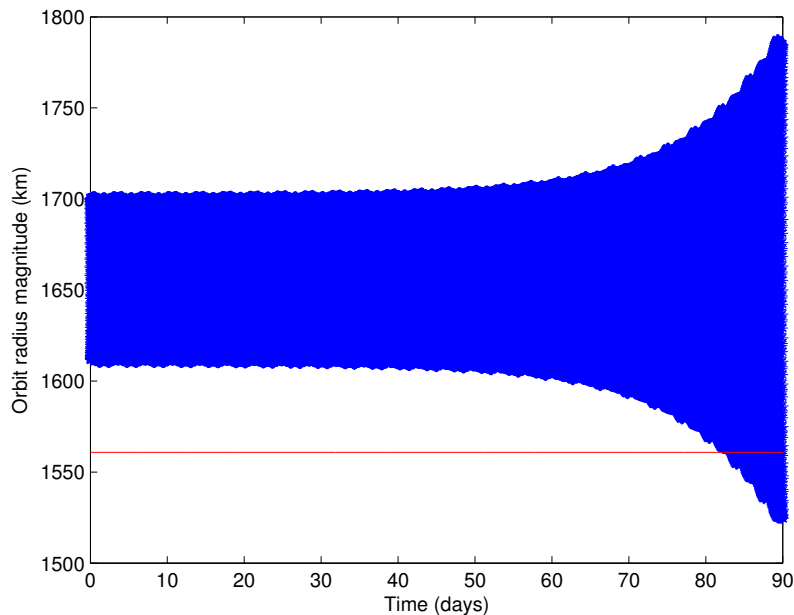
Figure 5.8: Orbit radius decay for 97 km orbit

Figure 5.9 shows the lifetime distribution produced by the nominal seven day covariance applied to the 97 km altitude periodic orbit. 10000 dispersed trajectories are integrated until impact. There is very little variance from the nominal lifetime of 83.3 days.

Figure 5.10 shows the covariance of a generic geodesy type orbit applied to a polar, 100 km altitude orbit. The periodic orbit has an average lifetime of around 83 days, already much greater than the 13 day average lifetime of a random geodesy orbit.

Neither Monte Carlo simulation produces much variance in their respective lifetime distributions. Investigating this, the entire covariance of the periodic orbit is scaled by a factor of 100 in both position and velocity terms to see the qualitative effect on the distribution. This produces a level of uncertainty of hundreds of meters in position and and tens of cm/s in velocity that is more realistic for the targeting of a deep space orbiter.

Figure 5.11 shows the lifetime distribution of a 97 km altitude periodic orbit with initial conditions dispersed by a covariance matrix scaled by factors of 100 in position and velocity. The intention of scaling the covariance in this way is to achieve 1σ accuracies that are 100 times larger
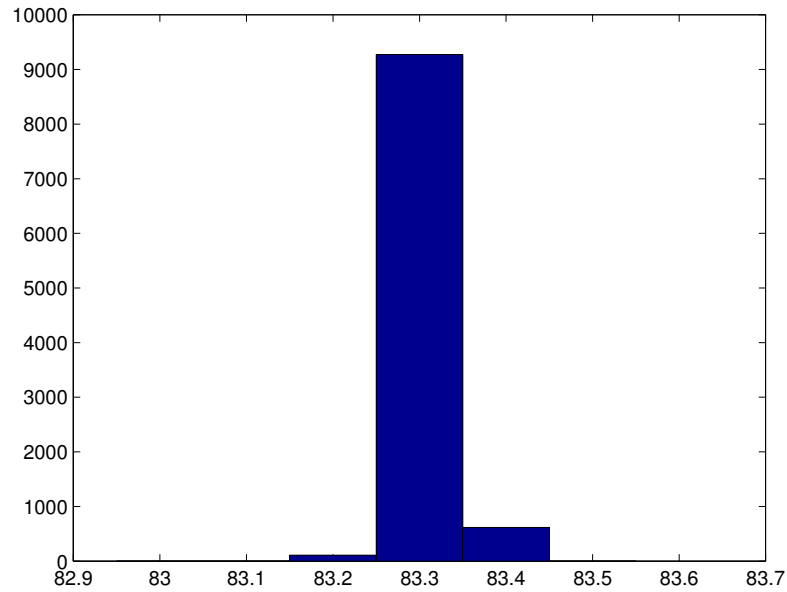
Figure 5.9: 97 km orbit with nominal covariance perturbation
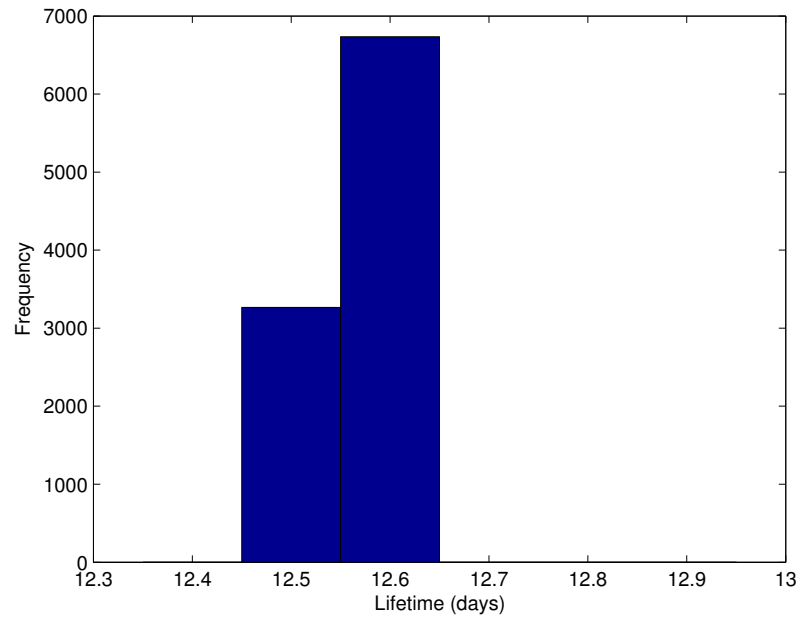
Figure 5.10: Typical geodesy type orbit with covariance dispersal

numerically than the nominal run. The mean of the distribution is lowered from the nominal 83
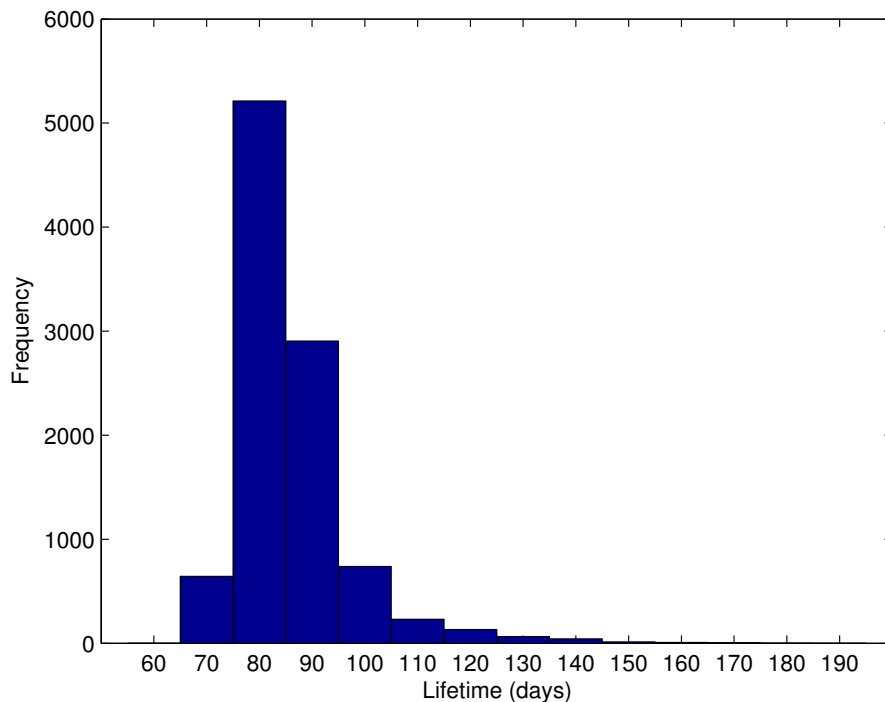
Figure 5.11: 97 km orbit with covariance perturbation scaled by 100^2

days but the distribution is skewed toward greater lifetimes. In addition to this long lifetime bias, none of the orbits dispersed by this augmented covariance matrix reach the 13 day lifetime of a generic polar orbit. If this process is repeated with a scaled covariance for the typical geodesy-type orbit, no increase in lifetime is observed.

Figure 5.12 shows the results of a Monte Carlo simulation conducted with only the diagonal terms of the processed covariance applied to the distribution. In this case, the mean of the distribution drops to around 76 days without the covariance (off-diagonal) terms. While some long lifetime orbits are present in this distribution, the lowest observed lifetime for this case, 45 days, is much lower than the minimum lifetime of 69 days from the full covariance draw. This suggests that the covariance terms which are based on tracking data, serve to remove the lowest lifetime orbits in the distribution.

Figure 5.13 shows the effect on orbit lifetime of shifting Jupiter's initial true anomaly away
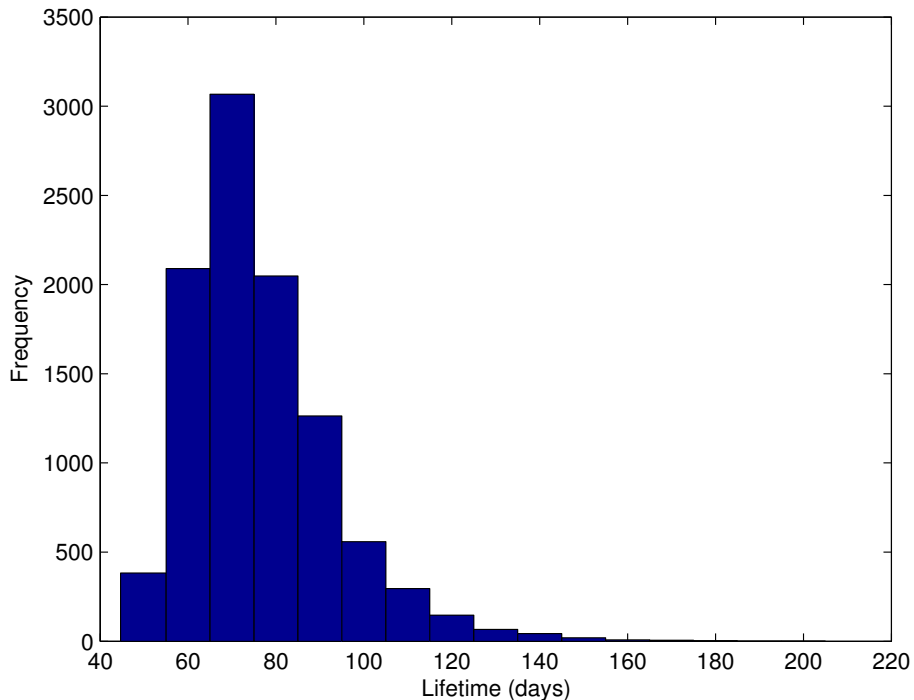
Figure 5.12: 97 km orbit with diagonal covariance perturbation scaled by 100^2

from periapsis such that the initial distance from Jupiter to Europa equals the semi-major axis of the Jupiter-Europa system. This is the circular system value for which periodic orbits are designed. Dispersed orbits are drawn from the scaled covariance matrix and the resulting lifetimes are much less than the other distributions. The lifetime distribution for this case is Gaussian, with a mean of around 56 days and very little variance. This shows the system is very sensitive to initial conditions and that the change in Jupiter true anomaly was too drastic.

Table 5.4: Monte Carlo lifetime statistics for shifting initial Jupiter true anomaly

$\Delta\nu_J$	Min (days)	Mean (days)	Max (days)
$+15°$	76.58	101.0	238.5
$+12°$	74.93	105.7	244.5
$+10°$	72.86	102.6	225.2
$+5°$	69.03	90.33	225.7
0	67.99	85.71	191.87
$-5°$	70.77	90.44	219.7
$-10°$	70.95	98.48	221.5
$-12°$	73.11	103.5	226.1
$-15°$	75.89	104.3	220.3
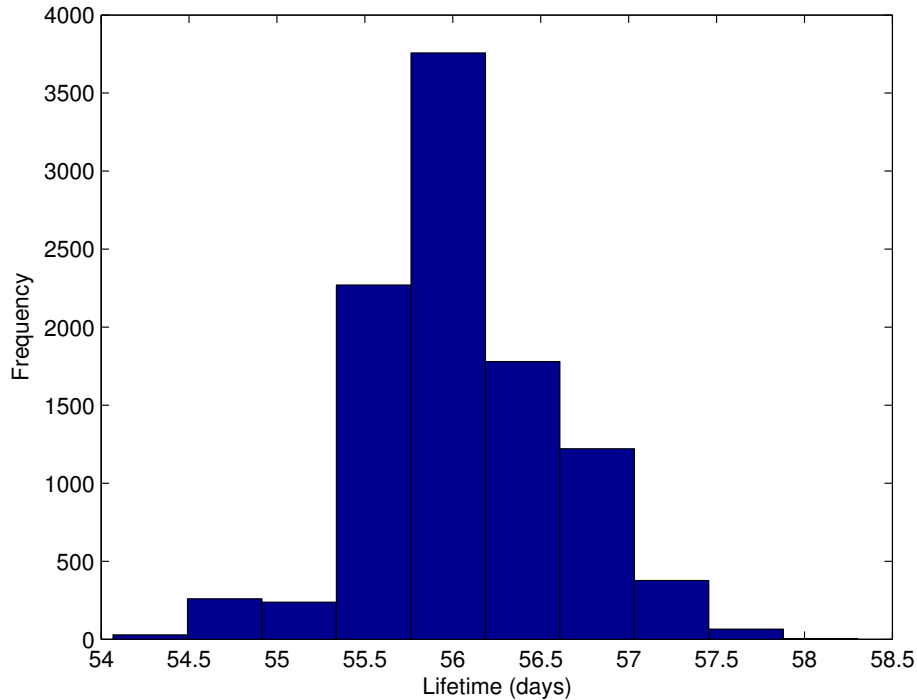
Figure 5.13: 97 km orbit with Jupiter initial true anomaly shifted by $\Delta\nu_J = \cos^{-1}(-e)$

The initial Jupiter true anomaly is shifted in small increments to determine whether positive or negative changes increase or decrease orbit lifetime. Some selected results are shown in Table 5.4. Greater mean lifetimes and greater maximum lifetimes are found by shifting the initial Jupiter true anomaly in both positive and negative directions. The mean and maximum lifetimes obtained from this process appear to peak for the $\Delta\nu_J$ case. The lifetime distribution for this case is shown in Figure 5.14.

The maximum lifetime for this Monte Carlo simulation is 244 days, more than 50 days greater than the maximum of the original scaled covariance dispersal. The mean lifetime is also raised to 105 days, a desirable trait for a Europa orbiter in an unstable system. The significance of the 12° value for shifting Jupiter' initial true anomaly is discussed in the following section. As a potential means of increasing the lifetime statistics of the distribution, the longest lifetime orbit from the scaled covariance draw selected as the nominal orbit of a new Monte Carlo simulation and dispersed
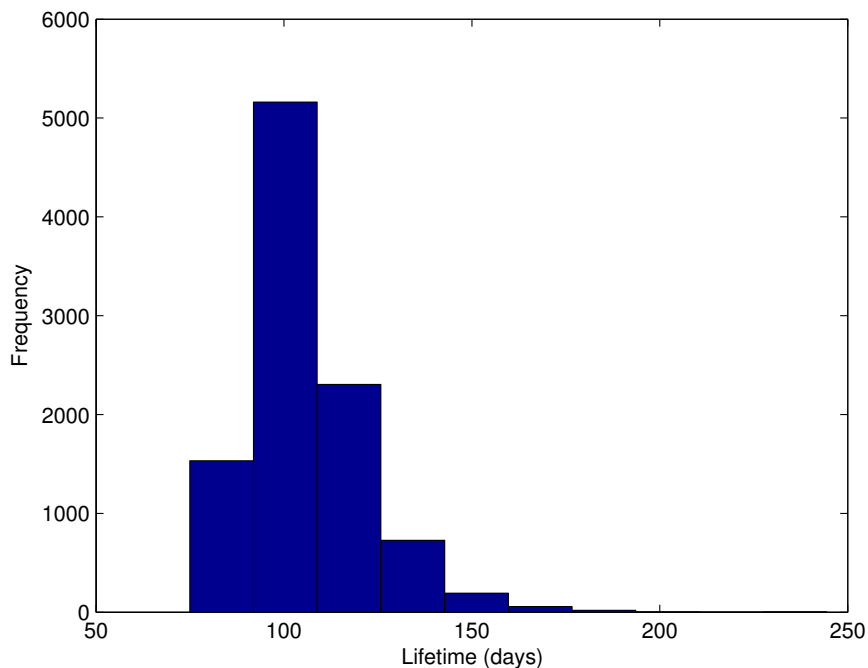
Figure 5.14: 97 km orbit with Jupiter initial true anomaly shifted by $\Delta\nu_J = +12°$

with the unscaled covariance.

Figure 5.15 shows the lifetime distribution produced by the covariance dispersal around this long lifetime orbit. The mean lifetime is shifted much higher to 168 days and the maximum lifetime in the eccentric inertial frame is 271 days. The same process is repeated for the maximum lifetime orbit from the shifted Jupiter true anomaly dispersal. Applying the nominal covariance to this long lifetime orbit yields a lifetime distribution in Figure 5.16 similar to that in Figure 5.15. Both have maximum orbit lifetimes near 270 days and increased mean lifetimes of 150 days.
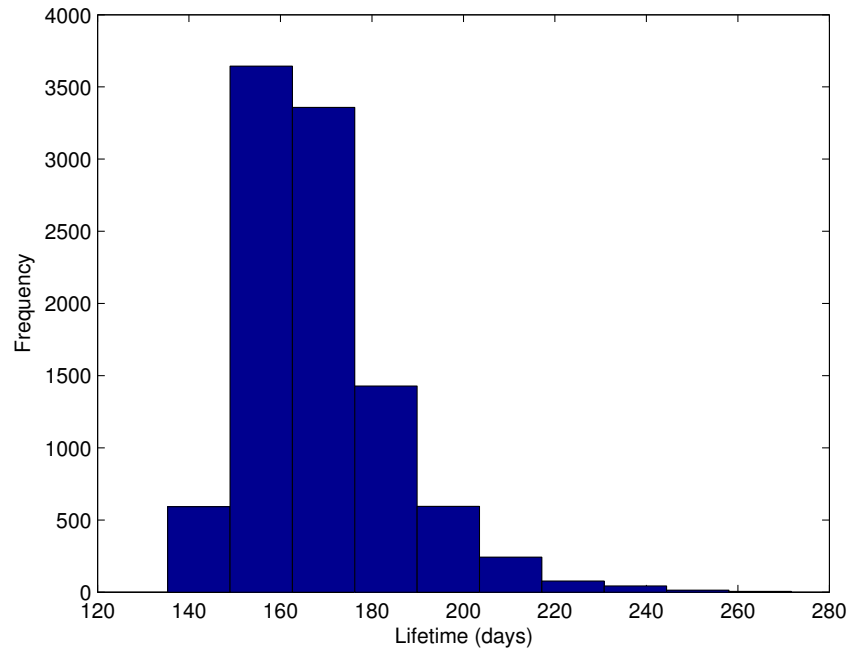
Figure 5.15: Long-lifetime orbit dispersed with nominal covariance matrix
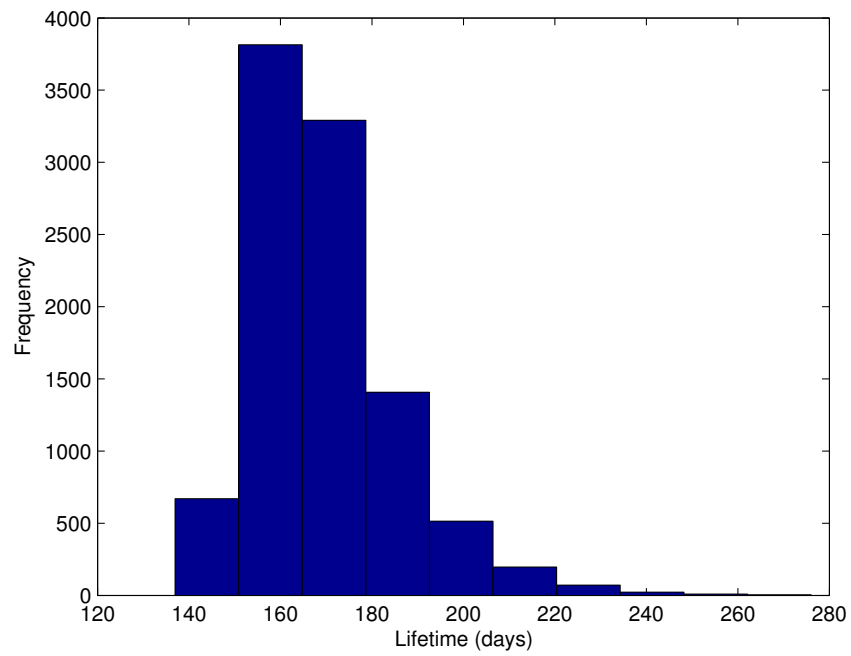
Figure 5.16: Long-lifetime orbit from $\Delta\nu_J = +12°$ simulation dispersed with nominal covariance matrix

5.4   Manifold Coordinate Decomposition

The bias toward longer lifetime orbits is an effect of conducting orbit determination in the vicinity of a periodic orbit. Seeking to find the cause of the increased orbit lifetimes observed in the processed covariance, coordinates other than position and velocity are investigated. Orbit elements are a natural first step. The initial eccentricity and argument of periapsis of the dispersed orbit distribution are shown in Figures 5.17 and 5.18 without the effect of Europa's eccentricity in the lifetime integrations.
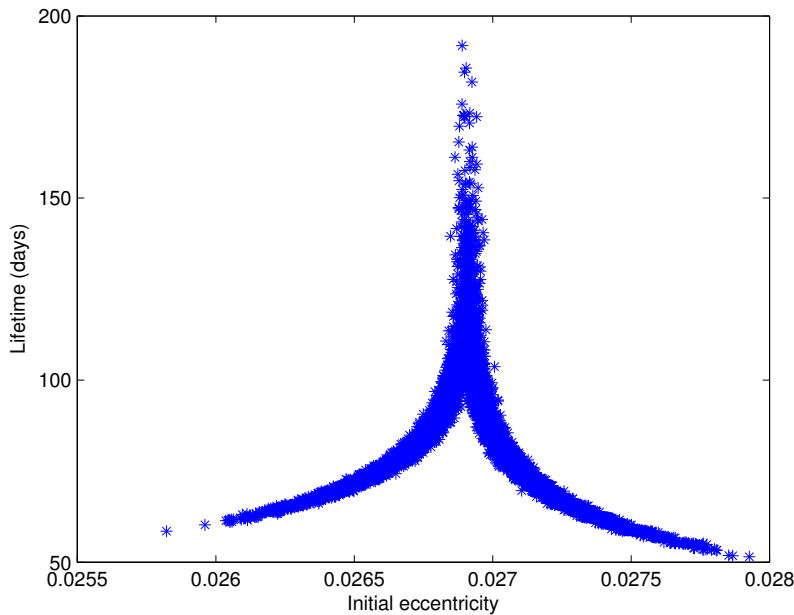
Figure 5.17: Initial eccentricity distribution

The nominal eccentricity and argument of periapse fall in the middle of both distributions. There is a definite trend toward a long lifetime eccentricity while the corresponding argument of periapse trend is not as pronounced. Figures 5.19 and 5.20 show the same plots with the effect of Europa's eccentricity included in the lifetime integrations. The trend toward a preferred eccentricity and argument of periapsis for greater lifetimes is still present but the symmetry of the distribution is broken by Europa's eccentricity.
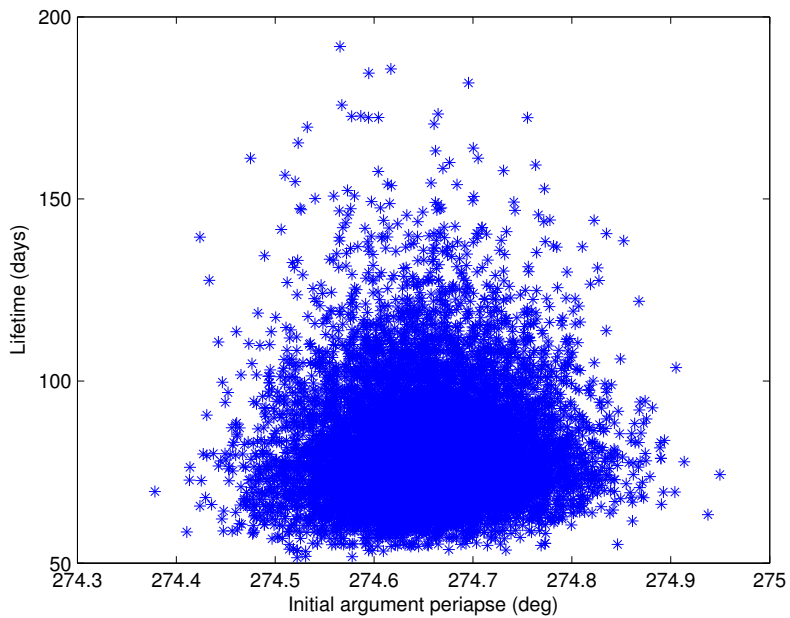
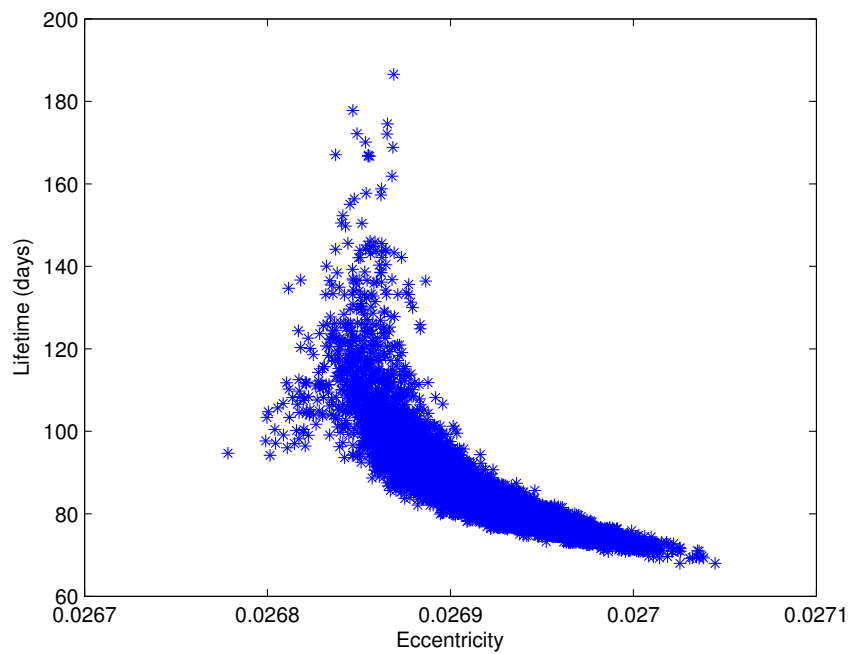Figure 5.18: Initial argument of periapsis distribution

Figure 5.19: Initial eccentricity distribution with Europa eccentricity

Figure 5.21 shows the distribution of Jacobi energy versus lifetime for the dispersed orbits.
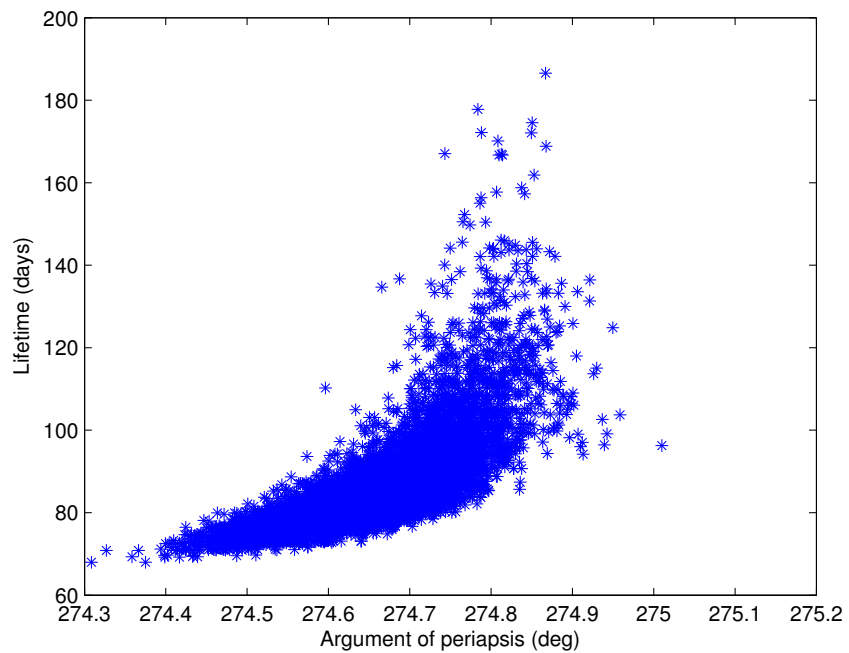
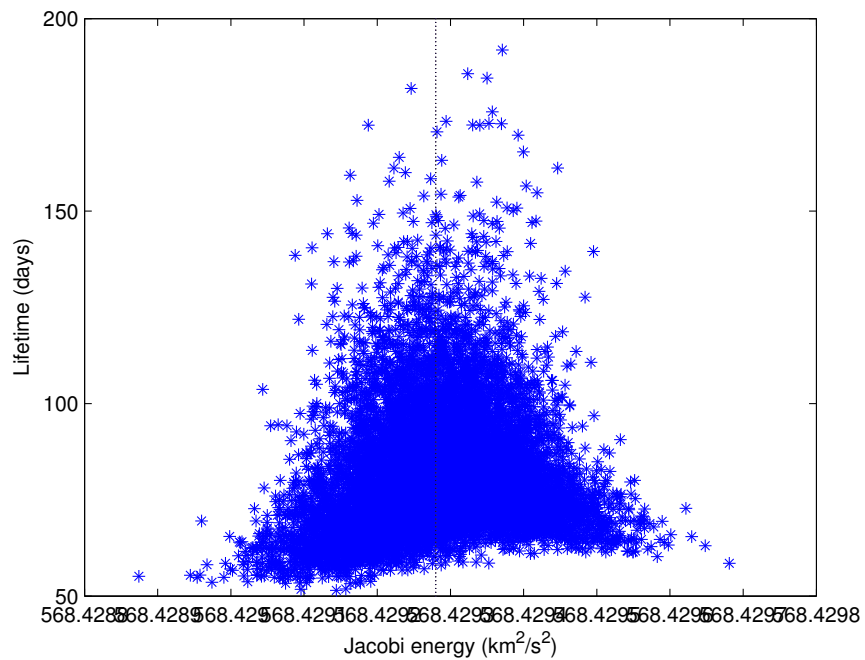Figure 5.20: Initial argument of periapsis distribution with Europa eccentricity

Figure 5.21: Jacobi energy distribution with lifetime

The energy of the nominal orbit is shown as the dotted line in the middle of the distribution. Since short and long lifetime orbits are both present for these values of eccentricity, argument of periapsis, and Jacobi energy, specific orbit elements and energies are not the driving force behind the increased lifetime. Orbits in the vicinity of the stable manifold associated with a periodic orbit are expected to have longer lifetimes. So, the stable and unstable manifolds of the nominal periodic orbit are computed and the initial conditions generated by covariance dispersal in the Monte Carlo simulation are projected into manifold coordinate space using the methodology in Appendix A.
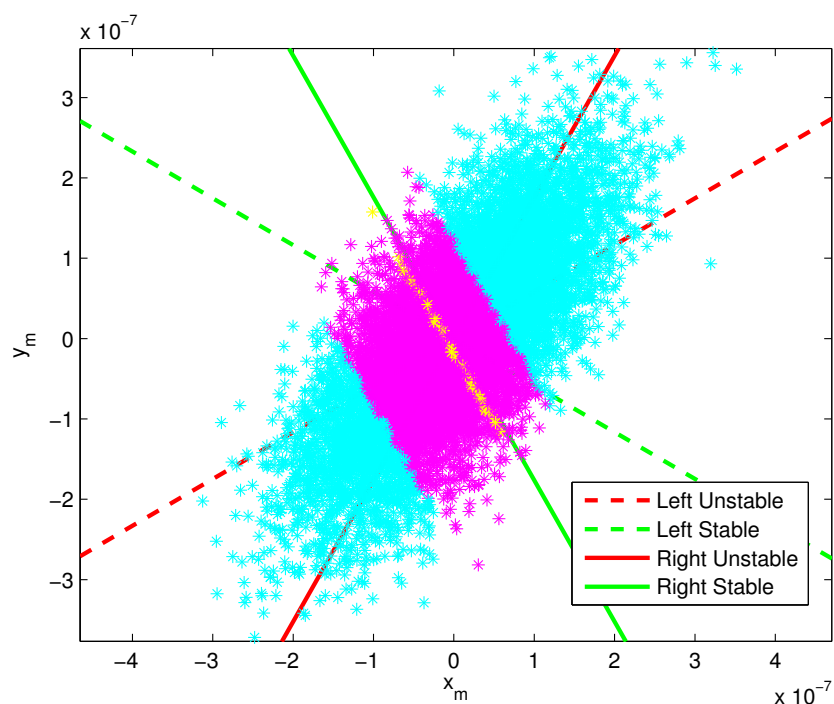
Figure 5.22: Dispersed orbit manifold coordinate projection distribution. Blue: $L < 70$ days, Cyan: $70 \leq L < 100$ days, Magenta: $100 \leq L < 150$ days, Yellow: $L > 150$ days

Figure 5.22 shows the manifold coordinate decomposition for the covariance scaled by 100^2 lifetime integrations without Europa eccentricity in the dynamics. The projections of the manifold coordinates are color coded based on the lifetime of the dispersed orbits. Blue denotes orbits with lifetimes L less than 70 days, cyan denotes lifetimes greater than 70 but less than 100 days, magenta denotes lifetimes greater than 100 but less than 150 days, and yellow denotes orbits with greater

than 150 days lifetime. The critical result comes from the properties of left and right eigenvectors. The left stable eigenvector (corresponding to the stable manifold) is orthogonal to all other right eigenvectors of the monodromy matrix except the right stable eigenvector. Similarly, the left unstable eigenvector is orthogonal to all right eigenvectors besides the right unstable eigenvector. In this projection, the right stable eigenvector is perpendicular to the left unstable eigenvector. It is likely that the orbits along the line formed by the yellow longest lifetime orbits in the distribution are aligned with the right stable eigenvector. In addition, other demarkations for increased lifetime are parallel to the left stable manifold as seen by the strips of color coded lifetime areas. When mapping forward in time, orbits aligned with the stable manifold approach the periodic orbit and orbits aligned with the unstable manifold depart from the periodic orbit [23]. The long lifetime orbits produced by the covariance dispersal follow the stable manifold toward the periodic orbit and then depart along the unstable manifold, effectively doubling the nominal lifetime of 83 days to greater than 150 days.
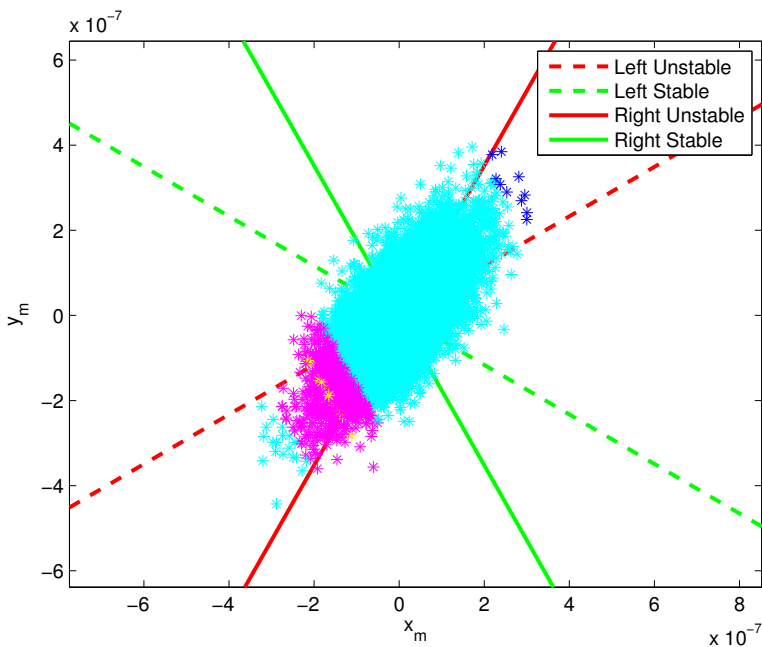

Figure 5.23: Dispersed orbit manifold coordinate projection distribution with Europa eccentricity. Blue: $L < 70$ days, Cyan: $70 \leq L < 100$ days, Magenta: $100 \leq L < 150$ days, Yellow: $L > 150$ days

This manifold structure is strictly valid only in the rotating frame with a circular Europa since the characteristic directions are computed in the RTBP. However, some of this structure will persist in the eccentric inertial frame. Figure 5.23 shows the manifold coordinate distribution for inertial integrations including Europa eccentricity. The lifetime distribution is similar in character to the circular Europa integrations with the main difference being the longer lived orbits are shifted away from the fixed point origin but are still parallel to the stable manifold.

Next, the nominal periodic orbit is continued into a family of periodic orbits to verify that there is no other manifold structure controlling the lifetime properties of the distribution. The orbit is continued by varying the Jacobi energy to find new periodic orbits and compare their eigenvalues, periods, and orbit elements. Small steps in Jacobi energy are required numerically to continue the orbit within its same family. The algorithm for this process is given in Section 2.3.2. The same Poincare map of $z = 0$ is used and the correction to the nominal periodic orbit is iterated to convergence using the same differential as the original computation. This process of continuing a family of periodic orbits is applied to the nominal periodic orbit with 1000 steps of $\delta C = 10^{-6}$ in the positive and negative energy directions. This process converges in both energy directions with the average difference in Jacobi energy of the newly converged orbit $\delta C = 1.7 \cdot 10^{-6}$. The characteristics of the nominal periodic orbit and the longest lifetime orbit from the Monte Carlo covariance draw are shown in Table 5.5. The difference in Jacobi energy is on the order of 10^{-4} and the resulting eigenvalues of the monodromy matrix and angles θ between the stable and unstable manifolds are nearly identical, varying only in the sixth decimal for eigenvalues.

Table 5.5: Continued Europa periodic orbit characteristics

	C (km^2/s^2)	θ (deg)	λ_u	λ_s
Original PO	568.4293	60.4064	1.291574	0.774249
191 day orbit	568.4294	60.4090	1.291576	0.774248

Figure 5.24 shows the decrease in orbit period resulting from a change in Jacobi energy from continuing the periodic orbit family. Figure 5.25 shows changes in the eigenvalues of the monodromy

matrix, with most of the change occurring in the complex eigenvalues associated with the center manifold. The near-unity real eigenvalues are maintained through the continuation process as are the stable ($\lambda_s < 1$) and unstable ($\lambda_u > 1$) real eigenvalues. The variation in the complex eigenvalues is on the order of 10^{-5} .
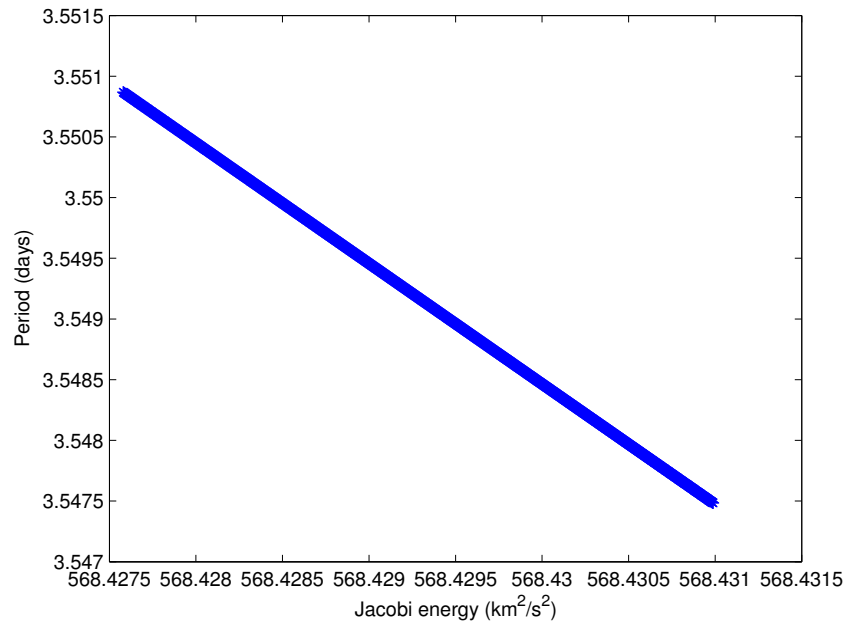

Figure 5.24: Change in orbit period vs. Jacobi energy for continued periodic orbits

The decrease in orbit period shown in Figure 5.24 suggests that the continued orbits are faster in some sense than the nominal periodic orbit. Since the number of Europa revolutions per orbit about Jupiter is conserved ($N = 41$), the semi-major axis should decrease. This is observed in the orbit elements shown in Figure 5.26 where the semi-major axis decreases and the eccentricity increases with the increase in Jacobi energy. Figure 5.27 shows that the inclination and argument of periapse also decrease with the increase in Jacobi energy. So, while the eigenstructure of the monodromy matrix is basically conserved in the continuation process, the resulting continued periodic orbits have slightly different orbital elements. Orbit eccentricity increases slightly but remains near the long lifetime value.

Since this continuation process reaches the Jacobi energy level of the long lifetime orbit from
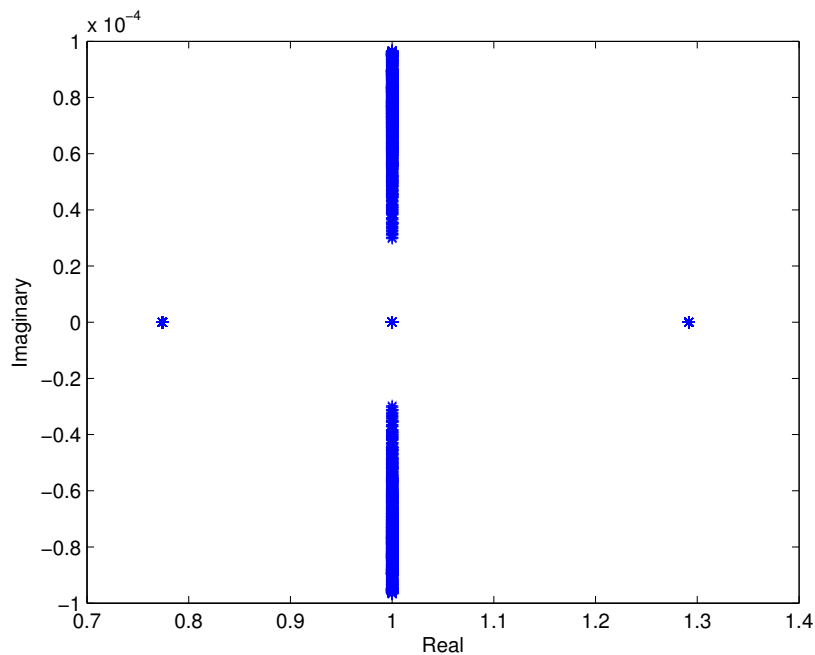
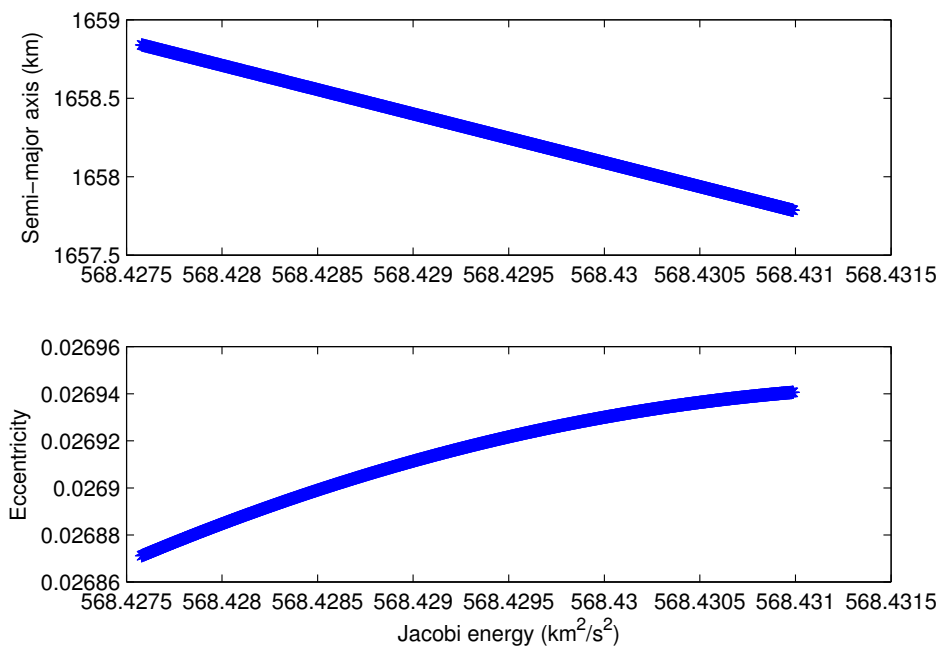Figure 5.25: Eigenvalue evolution for continued periodic orbits

Figure 5.26: Changes in semi-major axis and eccentricity with continuation

the scaled covariance draw, the manifold characteristics for that orbit are computed and applied
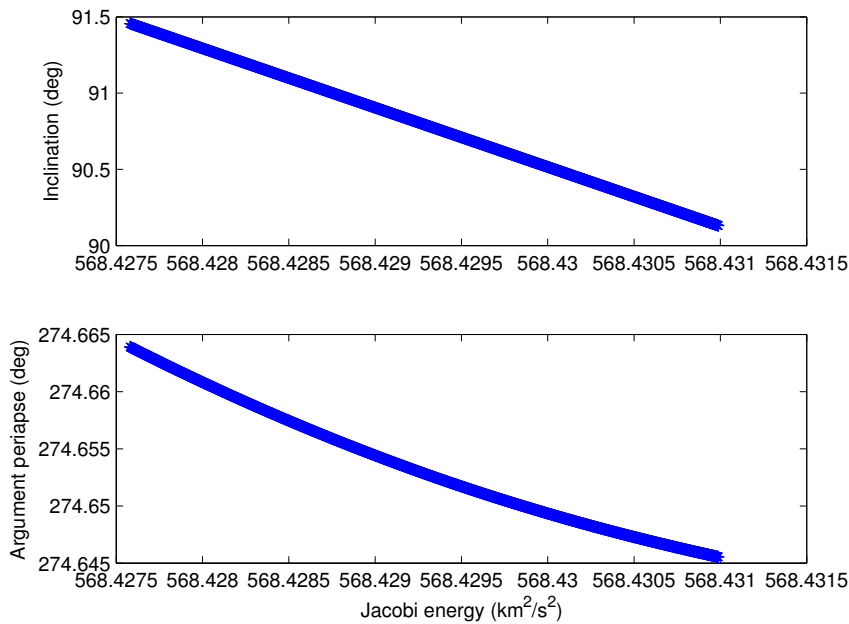
Figure 5.27: Changes in inclination and argument of periapsis with continuation

to scaled covariance distribution. Figure 5.28 shows this application.
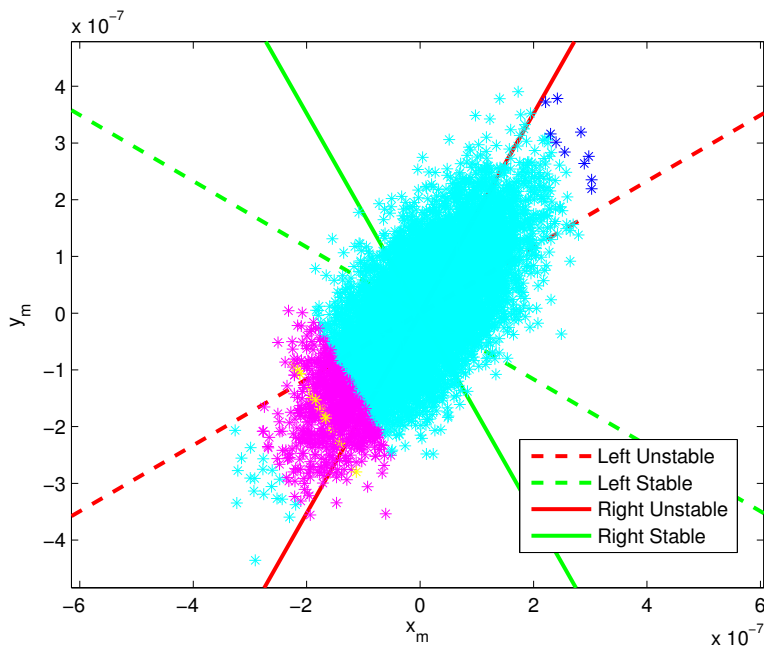

Figure 5.28: Manifold structure for 191 day lifetime orbit applied to scaled covariance draw. Blue: $L < 70$ days, Cyan: $70 \leq L < 100$ days, Magenta: $100 \leq L < 150$ days, Yellow: $L > 150$ days

This manifold coordinate distribution is not vastly different from that resulting from the nominal periodic orbit structure. The location of long lifetime orbits within the distribution is slightly shifter to the left but it is hardly noticeable.

Satisfied that there is no neighboring Jacobi energy periodic orbit that fits the distribution better, other methods of refining the manifold structure are explored. The manifold coordinate distribution for shifting the initial Jupiter true anomaly is shown in Figure 5.29. All of the dispersed orbits are color-coded blue because none avoid impact for longer than 70 days. From the lifetime histogram in the previous section, these orbits have lifetimes which vary little from 56 days.
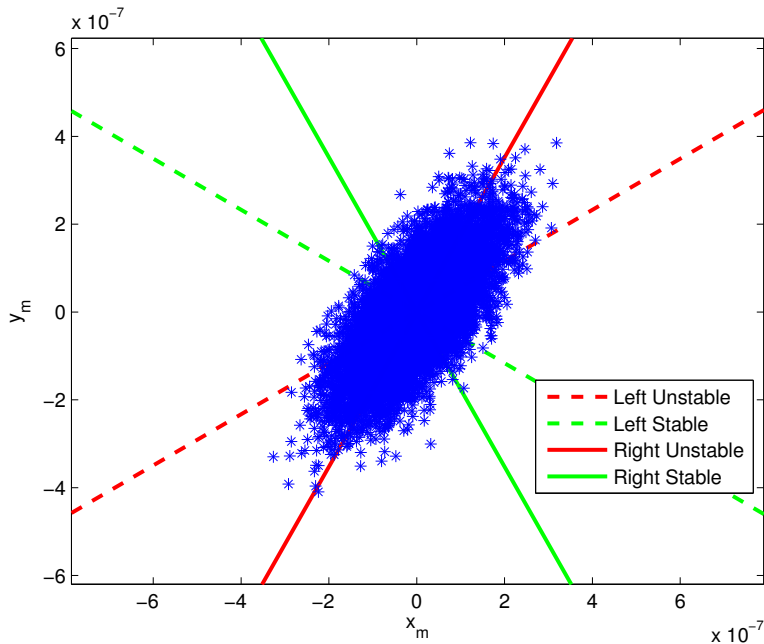

Figure 5.29: Manifold coordinate projection for $\Delta\nu_J = \cos^{-1}(-e)$. Blue: $L < 70$ days

Since this change to the system initial conditions has too drastic an impact on lifetime statistics, the distribution for $\Delta\nu_J = +12°$ is shown in Figure 5.30. This distribution resembles the zero Europa eccentricity case, where the phase space location of long lifetime orbits is shifted nearer the origin and back along the stable manifold. The effect of changing the initial position of Jupiter has the effect of shifting the lifetime distribution and raising the overall mean lifetime and maximum lifetime.
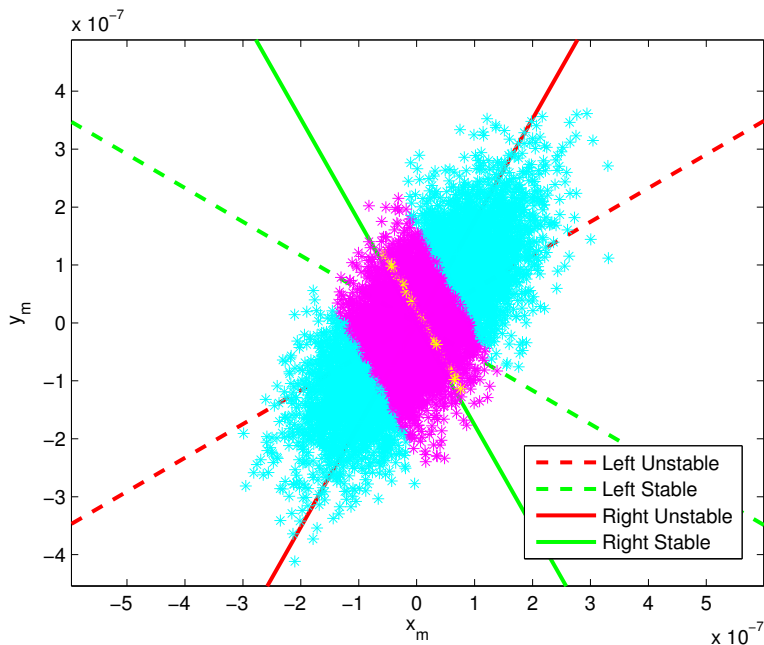
Figure 5.30: Manifold coordinate projection for $\Delta\nu_J = +12°$. Blue: $L < 70$ days, Cyan: $70 \leq L < 100$ days, Magenta: $100 \leq L < 150$ days, Yellow: $L > 150$ days

An additional method of increasing the lifetime statistics of the overall distribution is selecting the longest lifetime orbit from the original scaled covariance draw as the nominal and running another Monte Carlo simulation drawing from the original unscaled covariance as representative of a periodic orbit. Figure 5.31 shows the manifold coordinates of this distribution.

The unscaled covariance is used for this draw, so the extent of the distribution in phase space is much smaller than the other cases examined. The only colors present in the distribution are magenta and yellow, showing that all of the orbits have lifetimes at least greater than 100 days, with a much larger percentage of long lifetime orbits. The maximum lifetime from this distribution is 271 days, longer than the 191 day lifetime of the dispersed orbit used as the nominal for this simulation. Similarly, the nominal covariance is applied to the longest lifetime orbit from the shifted Jupiter initial true anomaly case. This again produces increased minimum, mean, and maximum lifetimes. Figure 5.32 shows the manifold coordinates of this case.

The maximum lifetime from this distribution is near 270 days also. While no orbit used in
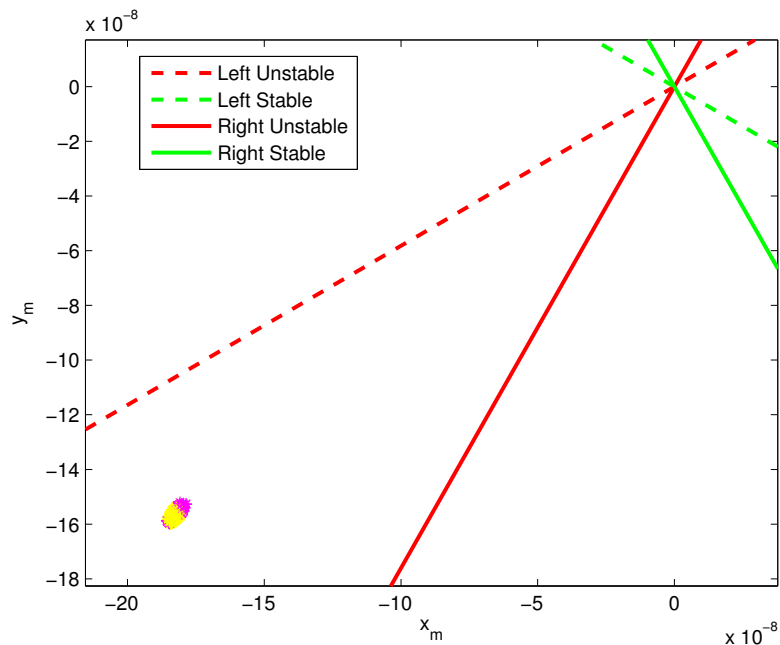
Figure 5.31: Manifold coordinate projection for nominal covariance drawn around 191 day lifetime orbit. Magenta: $100 \leq L < 150$ days, Yellow: $L > 150$ days
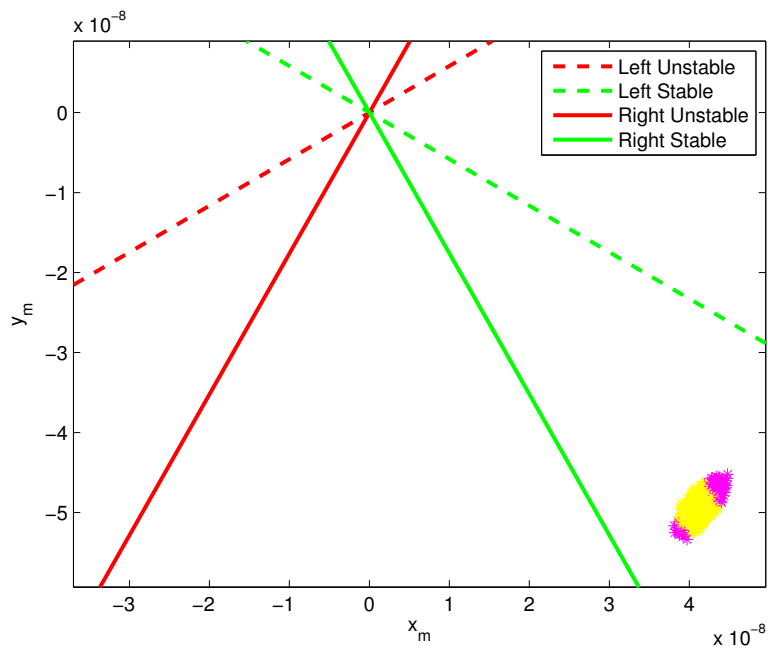

Figure 5.32: Manifold coordinate projection for nominal covariance drawn around $\Delta\nu_J = +12°$ long lifetime orbit. Magenta: $100 \leq L < 150$ days, Yellow: $L > 150$ days

a mission would be uncontrolled for 270 days, this lifetime represents an orbit that remains in the vicinity of its nominal trajectory for much longer than a generic orbit of the type useful for geodesy science.

5.5   Numerical Accuracy

Trajectories falling on or near the right stable manifold are expected to have desirable lifetime properties. Orbit initial conditions constructed using an extension of the linear right stable manifold should have comparable lifetimes to orbits found in the Monte Carlo distribution. The longest lifetime orbit from the Monte Carlo orbit simulation is dispersed in small increments along the right stable manifold. Since the long lifetime orbits from the simulation have manifold coordinates up to 10^{-7}, the increment used is $\epsilon = 10^{-9}$ up to 10^{-7} along either extent of the stable manifold, resulting in 201 trajectories. Again, the $z = 0$ surface of section is used and the resulting points are decomposed into manifold coordinates. This integration is carried out 100 days backward in time and a representative trajectory is shown in Figure 5.33.
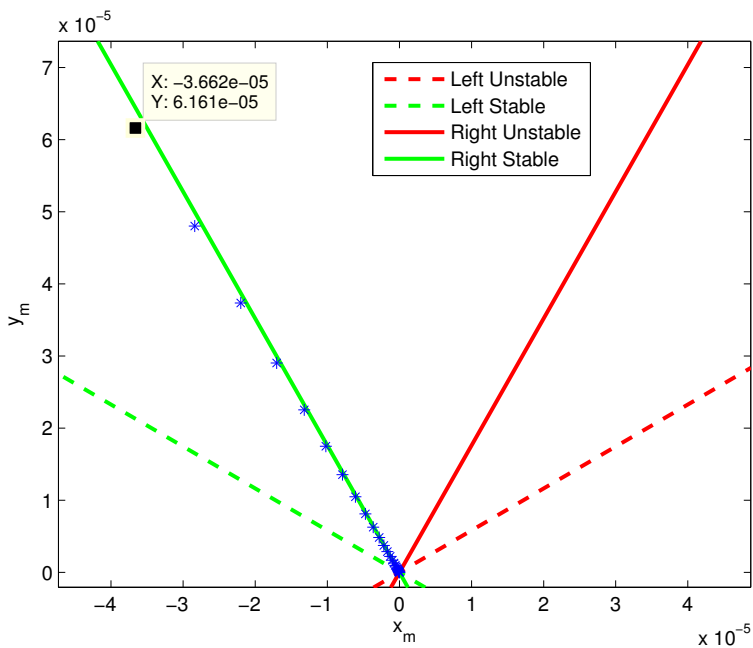

Figure 5.33: $z = 0$ manifold coordinates shown for long lifetime orbit integrated backward in time

The manifold coordinates themselves circulate and repeat about every 3.55 days which is the system repeat period for Europa about Jupiter. The general trend carries the trajectories slightly off the stable manifold but every 3.55 days or $N = 41$ revolutions, the coordinate decomposition falls on or nearly on the stable manifold again.

As a check on numerical accuracy, orbits are integrated backward and then forward along the stable manifold over time intervals corresponding to multiples of the system repeat period and the resulting state is compared with the initial condition. This is shown in Figure 5.34.
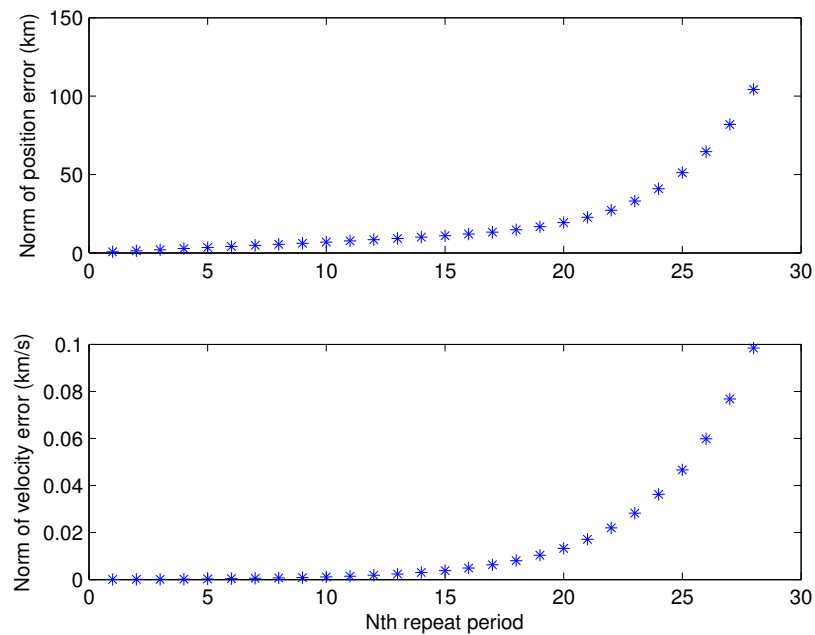

Figure 5.34: Integration error along the stable manifold

The magnitude of the position and velocity deviations are plotted against the number of full system repeat periods which each represent 3.55 days integration time. The numerical error is approximately linear up until around 15 repeat periods and then changes to a quadratic character. This is an expression of the instability of orbits in the Jupiter-Europa system. Better accuracy may be obtained along the stable manifold with a higher order integrator, such as an RK7(8) as opposed to the RK4(5) used here.

Since the points which occur at multiples of the system repeat period fall back on the stable

manifold, they are used as initial conditions for forward integration. Starting near the fixed point origin, each trajectory return on the stable manifold is integrated forward in time until impact with the surface.
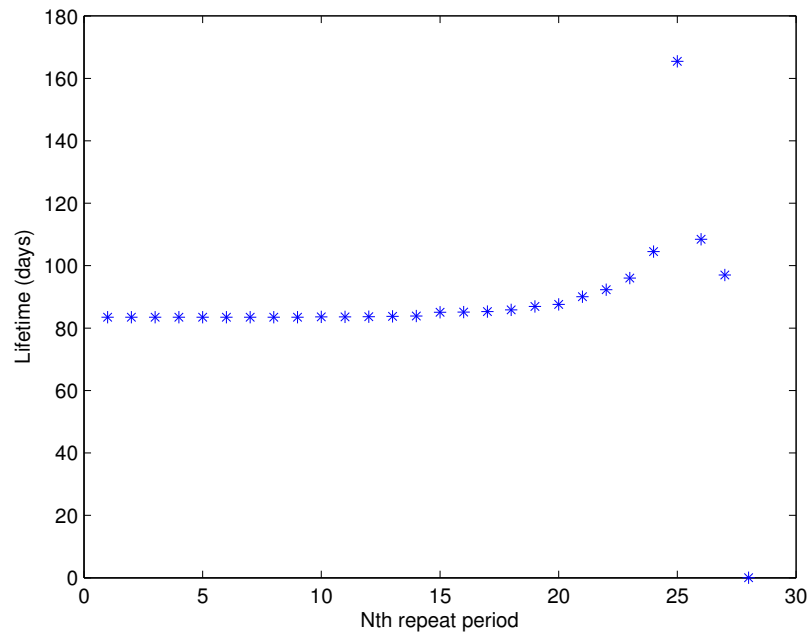

Figure 5.35: Forward integration orbit lifetime for initial conditions on the stable manifold

The orbit lifetimes for integration of these points on or near the stable manifold are shown in Figure 5.35. Interestingly, the trajectory closest to the fixed point does not give the longest lifetime. The longest lifetime orbit achieved from this process is generated by the 25th full system repeat point on the stable manifold. This point is called out as a data point on Figure 5.33. The lifetimes peak with this 25th repeat point which corresponds closely to the change in character of the error associated with integrating along the stable manifold. However, the maximum lifetime found this way is less than the original 191 day orbit found in the scaled covariance Monte Carlo and much less than the 271 day orbit from the iterated Monte Carlo.

Chapter 6

Enceladus Orbiters

In this chapter, periodic orbits are investigated as a means for extending orbit lifetime in the unstable environment of the Saturn-Enceladus system and enabling geodesy science. Other studies have examined periodic orbits at Encealdus [19] but not found orbits as highly inclined or as low altitudes as those presented here. Periodic orbits are computed in the RTBP without the effects of an Enceladus extended gravity field since no reliable estimate exists. The values of the Saturn-Enceladus system parameters are given in Table 6.1.

Table 6.1: Saturn-Enceladus system parameters

Parameter	Value
R_E (km)	256.3
e_E	0.0047
n_E (rad/s)	$5.3036 \cdot 10^{-5}$
T_E (days)	1.371
LU (km)	238040
TU (s)	18855
μ_E (km^3/s^2)	7.2095
μ_S (km^3/s^2)	$3.794 \cdot 10^7$

A covariance analysis is conducted about a nominal periodic orbit using a SRIF to obtain estimation state uncertainties for the orbiter position and velocity. This covariance is used to disperse the nominal orbit in a Monte Carlo simulation which reveals a bias toward longer lifetime orbits. The phase space structure of these orbits is examined through the application of manifold coordinates. This manifold structure is shown to be sensitive to changes in system initial conditions, specifically the initial position of Saturn. By iterating the Monte Carlo simulation using different

nominal orbits, the maximum lifetime achieved increases from 14.5 days to 26 days. This is an order of magnitude improvement over the lifetime performance of a low-altitude geodesy type orbit at Enceladus.

6.1 Enceladus Periodic Orbits

Periodic orbits at Enceladus are computed using the differential corrector discussed in Section 2.3.1. The resonant orbit period relation is illustrated in Figure 6.1. Since there is no published NASA report at the level of detail similar to JEO documents, several periodic orbits are computed at different altitudes corresponding to $N = 11$, $N = 10$, $N = 9$, and $N = 8$ revolutions per Enceladus orbit.
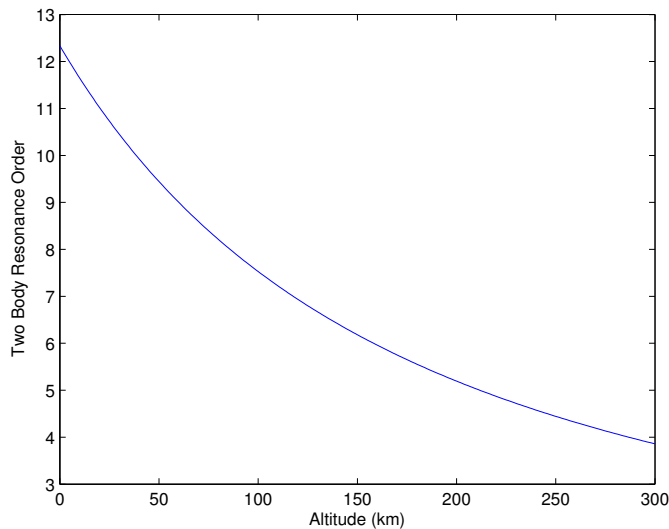

Figure 6.1: Number of orbiter revolutions N per Enceladus orbit

Figure 6.2 shows the change in the stable and unstable eigenvalues of computed periodic orbits at Enceladus. The magnitude of the unstable eigenvalue increases with altitude and the magnitude of the stable eigenvalue, which is the reciprocal of the unstable, slowly decreases. This increase in unstable eigenvalue corresponds to an increase in characteristic instability time, meaning the orbit will in general decay more quickly. For this reason, the 21 km altitude periodic orbit is

chosen for analysis. The 3D integrated periodic orbit is shown in Figure 6.3 and the top view is shown in Figure 6.4.
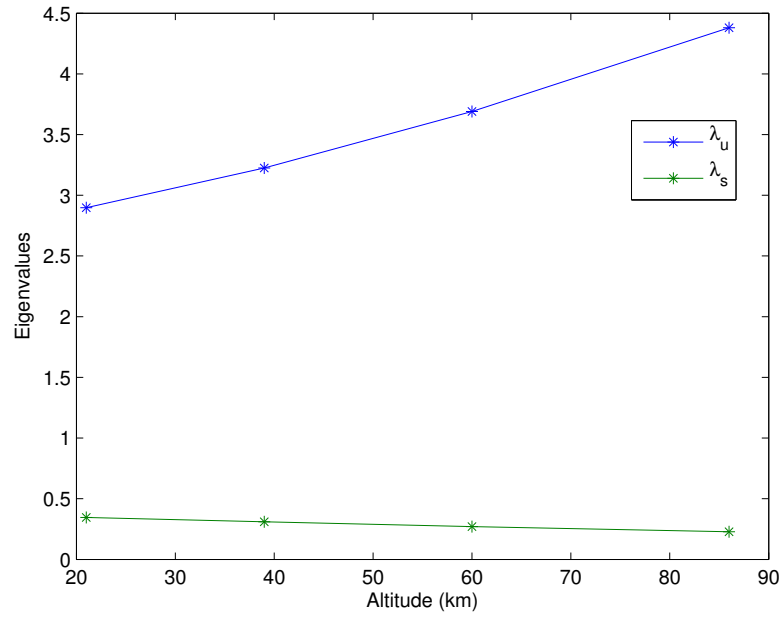

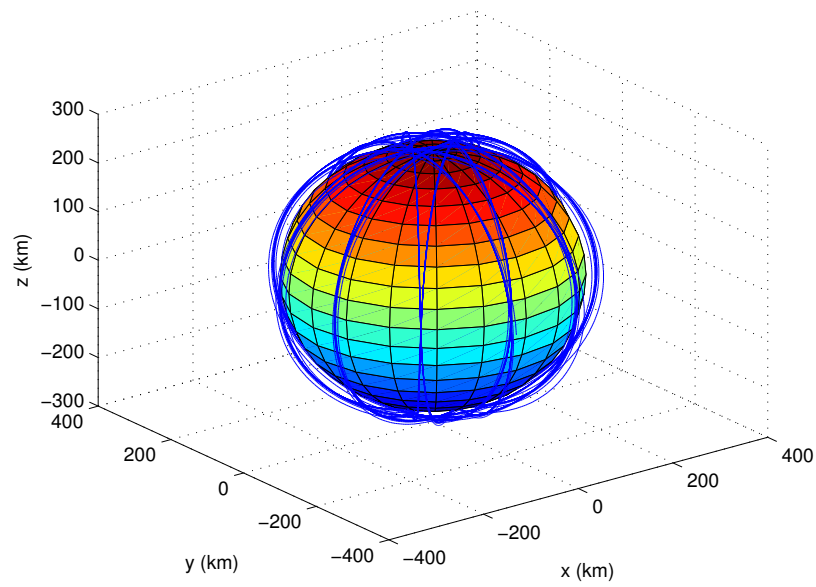Figure 6.2: Variation in eigenvalues with altitude for Enceladus periodic orbits

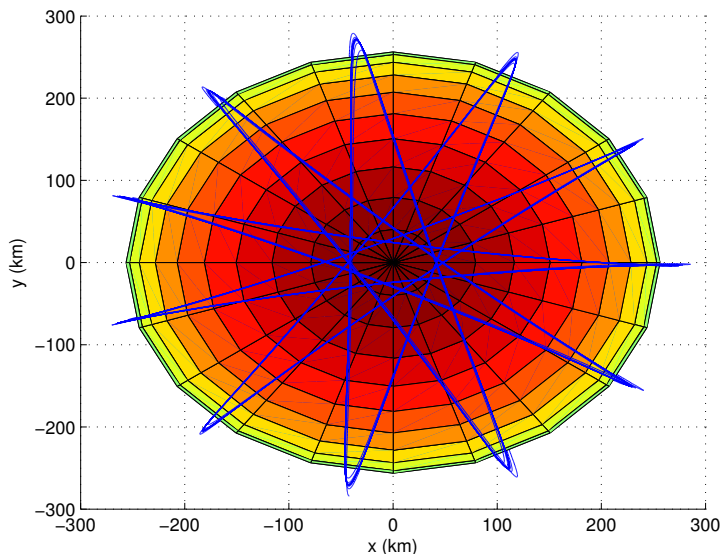Figure 6.3: 21 km altitude Enceladus periodic orbit

Figure 6.4: 21 km altitude Enceladus periodic orbit top view

There are some differences between this orbit and the Europa periodic orbit from the previous section. The body coverage is not quite as global since only $N = 11$ orbiter revolutions are made for each orbit of Enceladus about Saturn. Also, the inclination is 85.1°, giving a prograde orbit instead of a retrograde orbit. Table 6.2 shows the two-body orbit elements and eigenvalues for the 21 km altitude periodic orbit. The unstable eigenvalue is greater than that of the Europa periodic orbit in the previous section. The angle of intersection of the stable and unstable manifolds is also greater than the Europa orbit's, which will change the character of the manifold coordinate decomposition plots.

The variations of the two-body elements are shown over one repeat period, which is about 33 hours, in Figures 6.5, 6.6, and 6.7.

Table 6.2: Two-body orbit elements and eigenvalues for 21 km periodic orbit

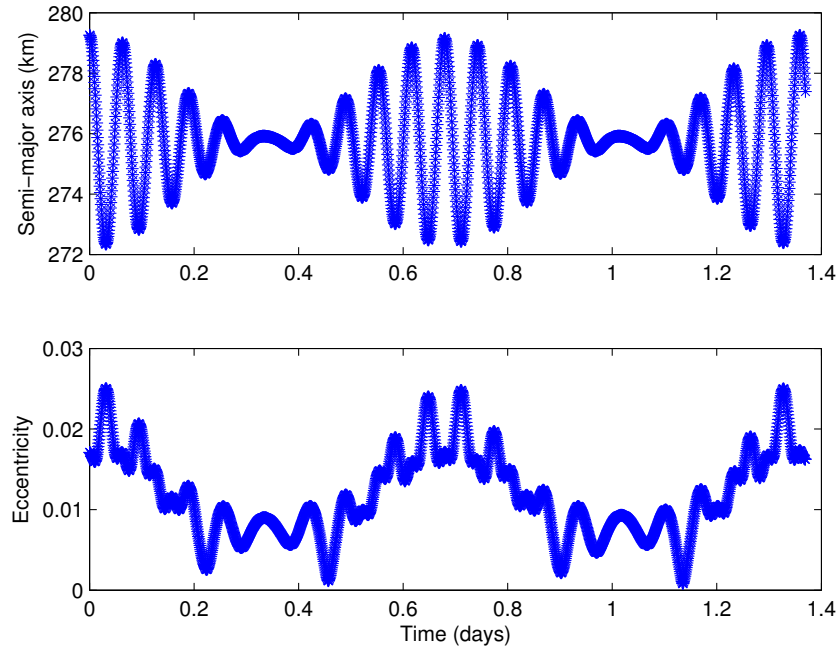| Element	Value
a (km)	279.26
e	0.017096
i (deg)	85.11
Ω (deg)	359.26
ω (deg)	0.36808
M (deg)	-0.355660
λ_u	2.8977
λ_s	0.345103
λ_{c1}	0.999999967 + 0.00025579 i
λ_{c2}	0.999999967 - 0.00025579 i
λ_1	1.0001
λ_1	0.99991
θ (deg)	76.303

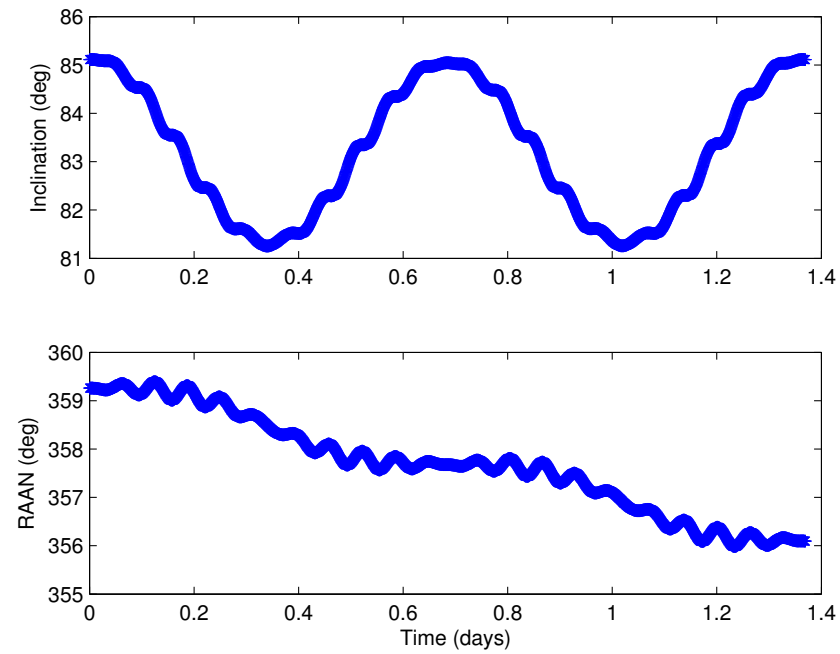Figure 6.5: Semi-major axis and eccentricity 21 km periodic orbit

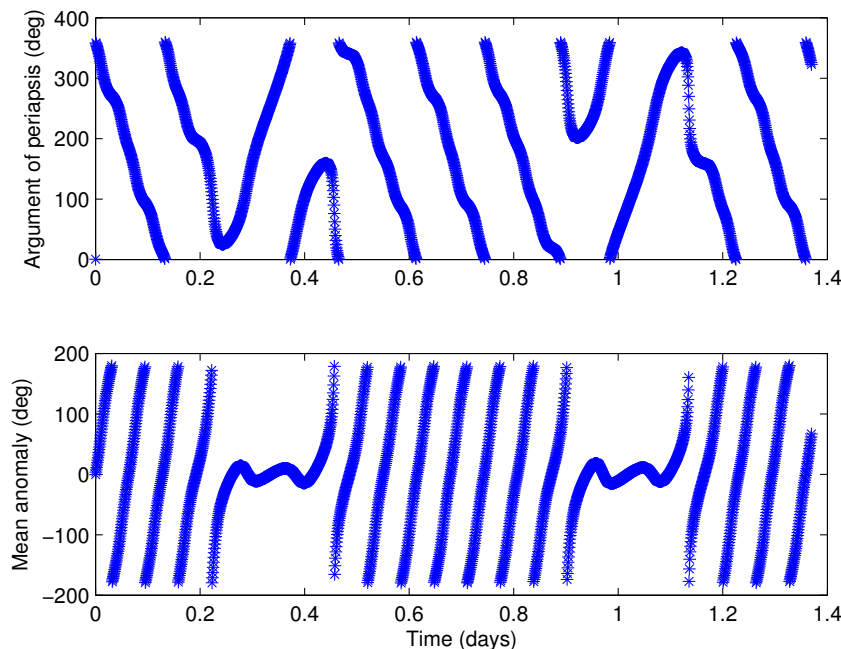Figure 6.6: Inclination and RAAN for 21 km periodic orbit

Figure 6.7: Argument of periapsis and mean anomaly for 21 km periodic orbit

6.2   Covariance Results

Range-rate measurement partials are accumulated in a SRIF to generate a covariance matrix about the 21 km altitude Enceladus periodic orbit. The only parameters included in the state list are the orbiter position and velocity. The extended gravity field terms are omitted from the state since they are not included in the dynamics and the Europa covariance results show that the Stokes coefficients up to C_{30} are sensed very accurately using range-rate data. Consider parameters are not included here either, for simplification. As seen in the Europa Monte Carlo simulation, the overall shape of the covariance, especially when projected into the manifold coordinate frame is of most interest.

Table 6.3 shows the 1σ state accuracies for a three day or two repeat period covariance run. The position uncertainties are on the order of centimeters and the velocity uncertainties are on the order of less than mm/s and again, may be challenging to realize for an outer planet type mission. The very small numerical state uncertainty values are the result of tracking a spacecraft so deep

Table 6.3: 21 km altitude Enceladus periodic orbit initial state uncertainties

x (km)	9.1073×10^{-06}
y (km)	1.0711×10^{-04}
z (km)	1.8368×10^{-05}
u (km/s)	9.2547×10^{-09}
v (km/s)	1.2222×10^{-07}
w (km/s)	1.1409×10^{-08}

within a gravity field. The closer the orbiter is to the body, the greater gravitational force the body exerts and the better the state can be fit to the observed accelerations. These uncertainties will be scaled along with the overall covariance matrix to obtain greater spread in orbit initial conditions in the following Monte Carlo simulations.

6.3   Monte Carlo Lifetime Simulation

To evaluate the statistical properties of an orbit's lifetime, the initial position and velocity of the orbit are dispersed by drawing a random vector from the multivariate normal distribution with zero mean and covariance specified by the output of SRIF covariance analysis. This process is repeated in a Monte Carlo simulation 10000 times and the time to impact along with the integrated spacecraft state are saved for each run. Figure 6.8 shows the eventual decay of the radius magnitude of the nominal 21 km altitude periodic orbit, yielding a 7.47 day lifetime when the radius curve intersects the red line representing Enceladus's surface radius. The Monte Carlo results for the nominal covariance draw are shown in Figure 6.9. Similar to the nominal Europa covariance results, there is very little variance in the lifetime results. All dispersed trajectories have the nominal lifetime with variation in the fifth decimal place.

To obtain variation in the lifetime statistics, the nominal covariance is scaled to increase the uncertainty levels in the orbiter position and velocity. The scale factor used here is much greater than that employed at Europa since the generated covariance is so reduced. Scaling the entire covariance matrix by 10000^2 results in increasing the 1σ uncertainty levels by factors of
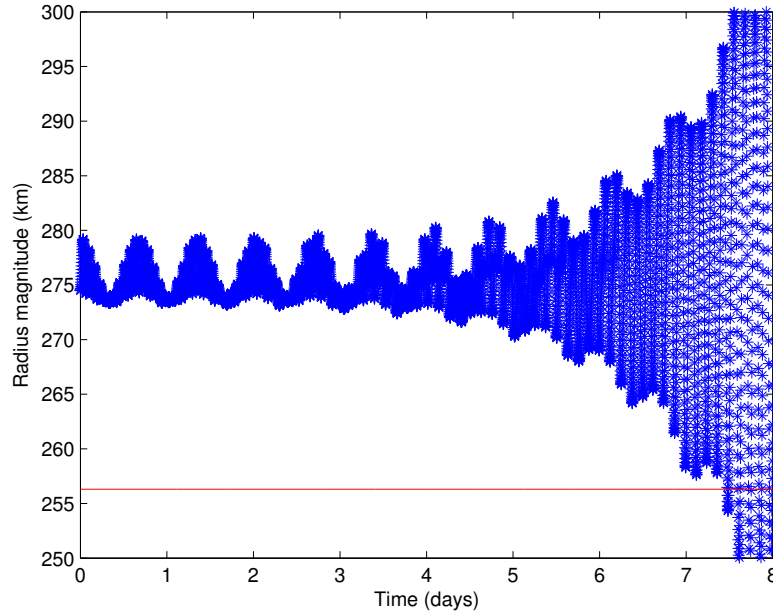
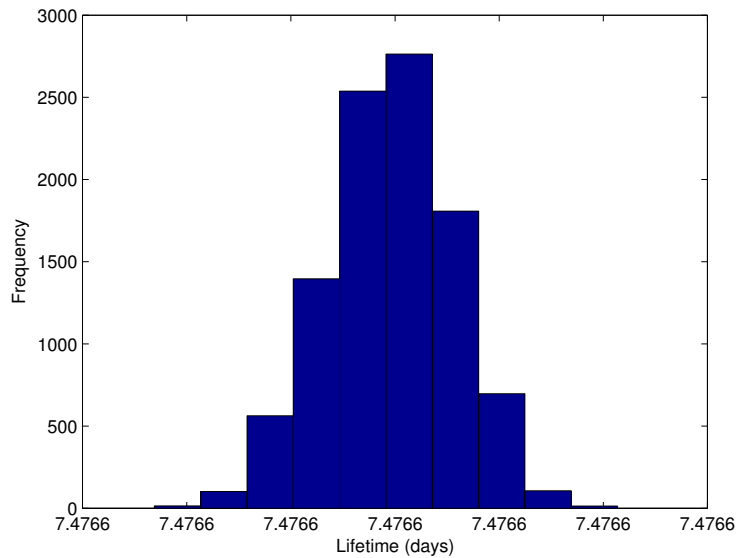Figure 6.8: Orbit radius decay for 21km periodic orbit

Figure 6.9: Lifetime distribution for nominal covariance draw

10000, yielding hundreds of meters dispersion in position and m/s dispersion in velocity. This scaled covariance draw results in a bias toward longer lifetimes as well as raising the mean of the distribution. The lifetime histogram is shown in Figure 6.10 with a maximum lifetime of 14.47

days.

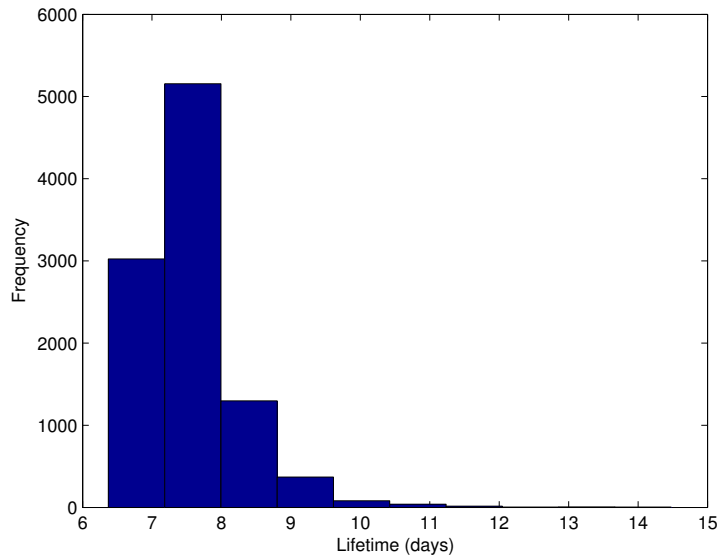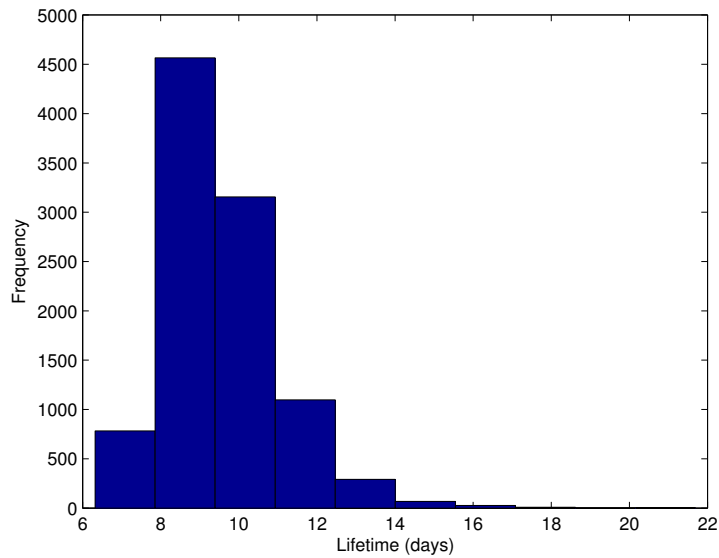Figure 6.10: Lifetime distribution for 21 km altitude orbit dispersed with covariance scaled x10000^2

Figure 6.11: Lifetime distribution for $\delta\nu_S = -2°$ dispersed with covariance scaled by 10000^2

The lifetime distribution can be further modified by adjusting the Saturn-Enceladus initial conditions by stepping the Saturn initial true anomaly. Since Enceladus is much closer to its primary

and much smaller physically than Europa, the overall system is more sensitive to configuration and a smaller $\Delta\nu_S$ produces the most desirable lifetime distribution. Figure 6.11 shows this lifetime distribution for $\Delta\nu_S = -2°$ dispersed with the scaled covariance, with a maximum lifetime of 21.69 days. The same strategy for further improving the lifetime distributions used at Europa is then employed at Enceladus. The longest lifetime orbits from both the scaled covariance draw and the shifted Saturn true anomaly draw are dispersed using their respective covariances scaled by factors of only 100^2. The first result for the covariance scaled by 100^2 applied to the 14.47 day long lifetime orbit is shown in Figure 6.12.
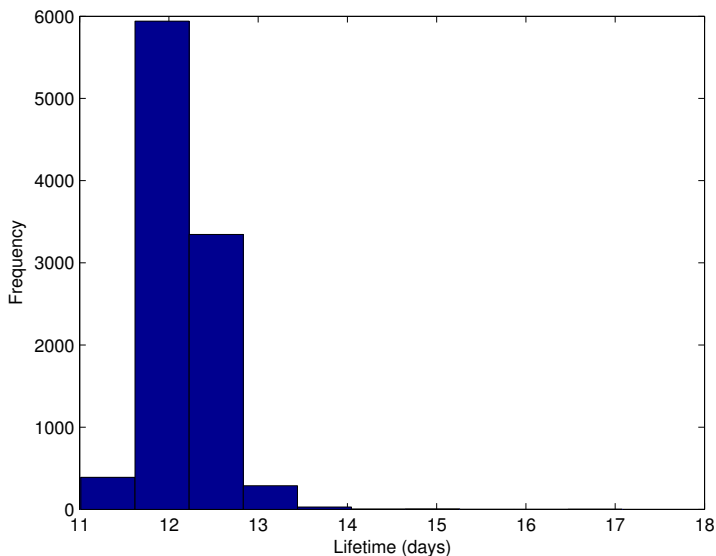

Figure 6.12: Lifetime distribution for covariance scaled x100^2 applied to long lifetime orbit

The mean and maximum of this distribution are raised from the levels of the larger scaled covariance draw. This is due to drawing orbits from a smaller phase space area surrounding the long lifetime orbit. The maximum lifetime of this draw is 17 days, which is still not greater than the maximum obtained from shifting ν_S. Thus, we repeat the process using the long lifetime orbit from the shifted true anomaly draw. Figure 6.13 shows the result of applying the covariance scaled by a factor of 100^2 to the 21 day long lifetime orbit from the shifted true anomaly draw. The mean of this distribution is raised over 15 days and the maximum lifetime is 26 days, more than tripling

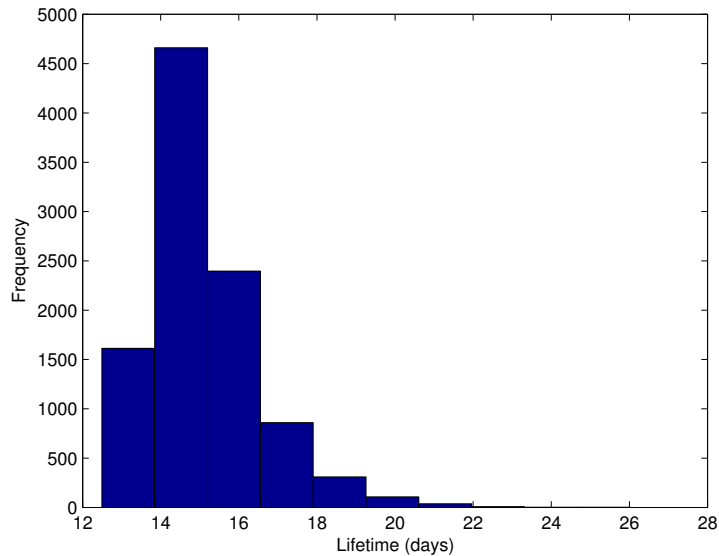the lifetime of the nominal periodic orbits selected.

Figure 6.13: Lifetime distribution for covariance scaled x100^2 applied to $\delta\nu_S = -2°$ long lifetime orbit

A summary of the lifetime statistics from these varied Monte Carlo simulations is given in Table 6.4. By applying the nominal covariance scaled by a factor of 100^2 to the longest lifetime orbit of the shifted Saturn true anomaly distribution, the longest lifetime of the simulations is obtained. Successively scaling the initial covariance, shifting ν_S, and applying the scaled covariance to long lifetime orbits as the nominal raises the mean of the distribution with each iteration. The final achieved mean is over 15 days, which is double the nominal orbit lifetime value.

Table 6.4: Monte Carlo lifetime statistics for different Enceladus covariance draws

Case	Min (days)	Mean (days)	Max (days)
Nominal	7.47662	7.47663	7.47664
Nominal x10000^2	6.372	7.578	14.48
$\Delta\nu_S = -2°$	6.319	9.490	21.69
$\Delta\nu_S = -1°$	6.864	8.850	17.80
$\Delta\nu_S = -5°$	5.577	6.550	7.669
$\Delta\nu_S = +5°$	5.504	5.876	7.368
Scaled LL x100^2	11.02	11.96	17.08
$\Delta\nu_S = -2°$ LL x100^2	12.49	15.17	26.02

6.4   Manifold Coordinate Decomposition

The bias toward longer lifetime orbits is an effect of conducting orbit determination in the vicinity of a periodic orbit. Again, coordinates other than position and velocity are investigated as the cause of the increased orbit lifetimes observed in the processed covariance. The initial eccentricity and argument of periapsis of the dispersed orbit distribution are shown in Figures 6.14 and 6.15 with the effect of Enceladus's eccentricity in the lifetime integrations.
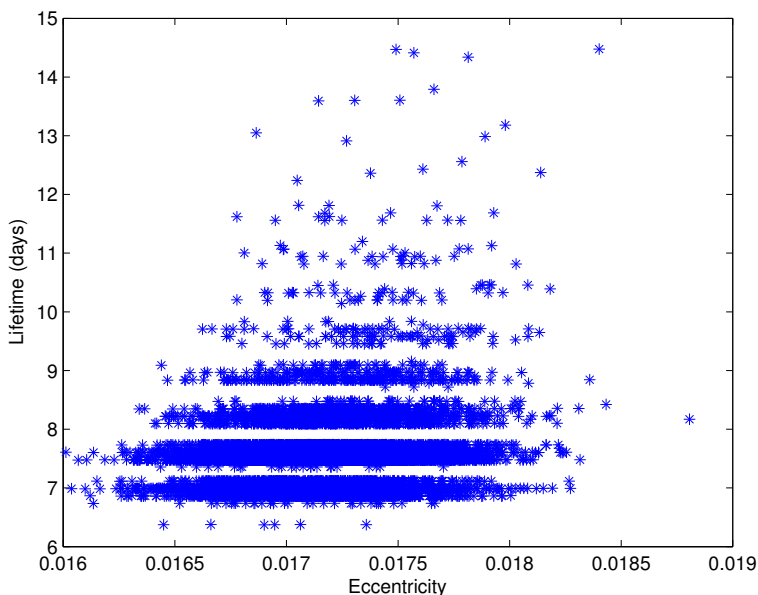

Figure 6.14: Initial eccentricity distribution for covariance scaled x10000^2

As seen in the Europa distributions, there is a trend toward a longer lifetime eccentricity, and for Enceladus, the argument of periapsis is qualitatively similar. However, there are both long and short lifetime orbits present at the center of the eccentricity and argument of periapsis distributions. Thus, two-body orbit elements are not the controlling parameter for long lifetime orbits. The initial state dispersals of each Monte Carlo simulation in the previous section are decomposed into manifold coordinates using the stable and unstable manifolds associated with the nominal 21 km altitude periodic orbit.
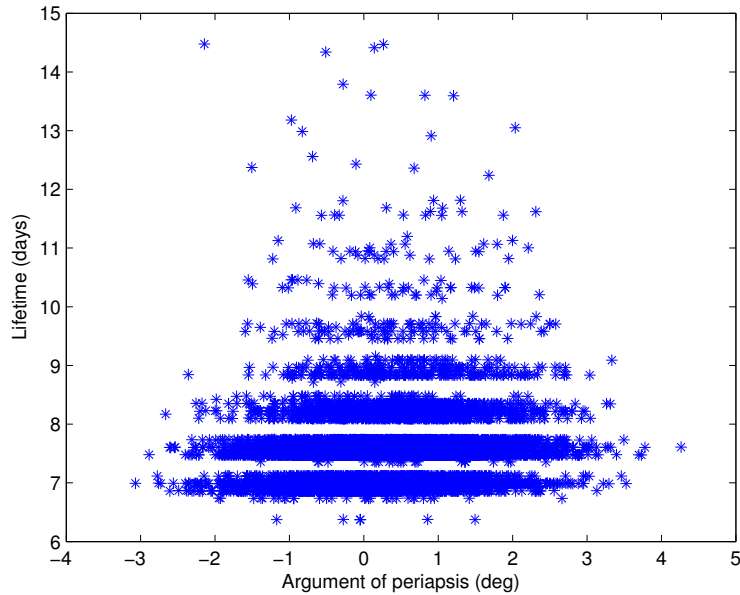
Figure 6.15: Initial argument of periapsis distribution for covariance scaled x10000^2

Figure 6.16 shows the manifold coordinate distribution for the covariance scaled by a factor of 10000^2 applied to the nominal periodic orbit. The color-coding for different lifetime levels is: Blue ≤ 7 days, Cyan 7 days $< L \leq 8$ days, Magenta 8 days $< L \leq 9$ days, Yellow $L > 9$ days. For the 21 km altitude periodic orbit, the angle of intersection θ of the stable and unstable manifolds is 76.3°, greater than the analogue at Europa. This changes the relative orientation of the left and right eigenvector directions. The eigenvector orthogonality properties are preserved, with the left stable manifold perpendicular to the right unstable manifold and the left unstable manifold perpendicular to the left stable manifold. For Enceladus, the overall extent of the covariance is along the right stable manifold. This gives a greater likelihood of drawing a long lifetime orbit from the covariance, since the Europa results and Enceladus results confirm that such orbits are aligned with the right stable manifold. The same delineations in lifetime levels are present in Figure 6.16, where the long lifetime orbits are slightly offset from the fixed point origin and the different lifetime levels are parallel to the right stable manifold.

Figure 6.20 shows the manifold coordinate decomposition for the Monte Carlo simulation
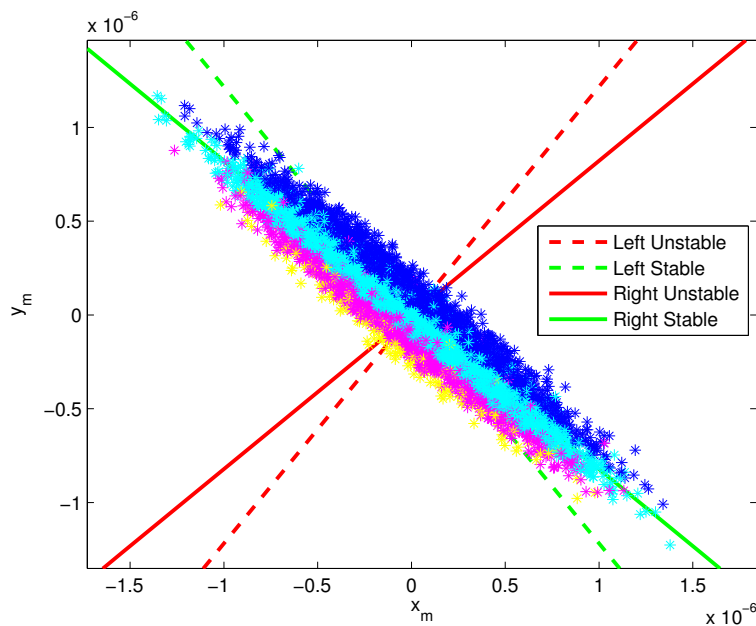
Figure 6.16: Manifold coordinate distribution for covariance scaled x10000^2
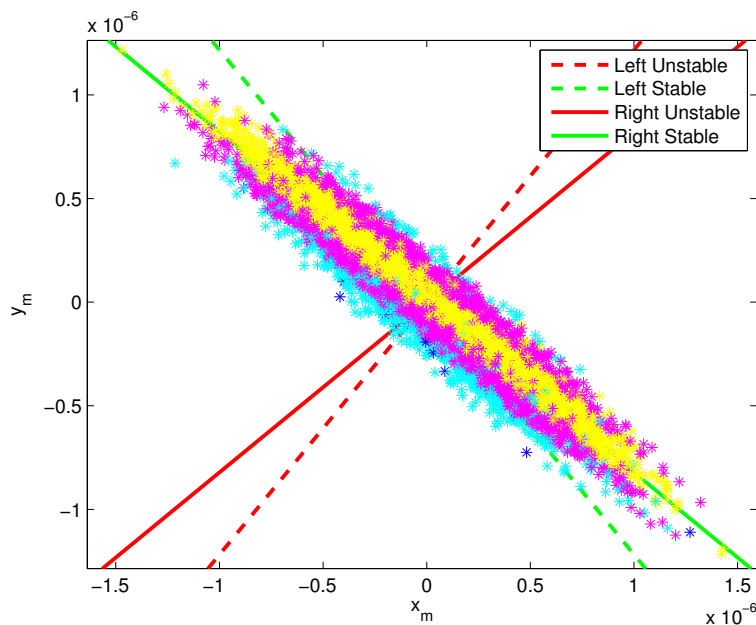

Figure 6.17: Manifold coordinate distribution for $\delta\nu_S = -2°$

with Saturn's initial true anomaly shifted by $\delta\nu_S = -2°$. The yellow long lifetime orbits have been

shifted back over the right stable manifold as we expect to see in the circular Enceladus case and

is the cause if the overall improvement in lifetime performance for the distribution. Very few blue orbits with less than 7 day lifetimes are present and the mean lifetime of this distribution is 9.49 days.
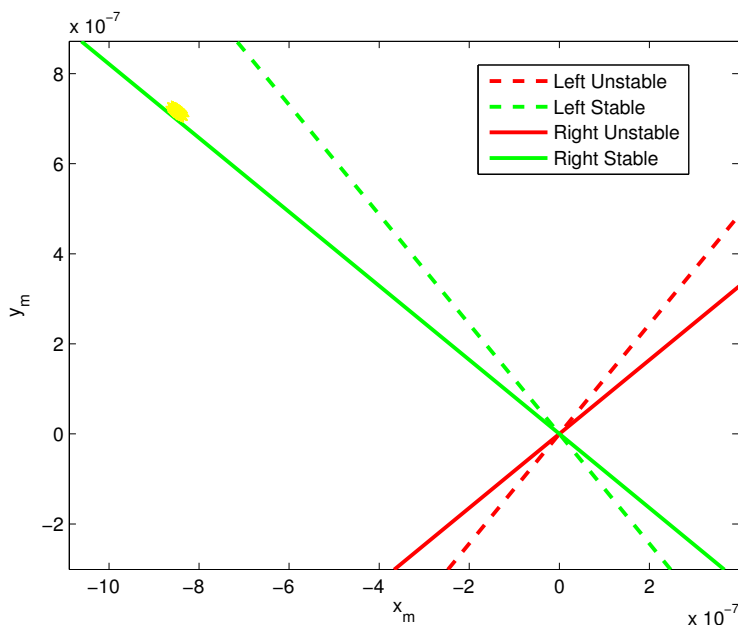

Figure 6.18: Manifold coordinate distribution for covariance scaled x100^2 applied to long lifetime orbit

Seeking to improve the lifetime distribution further, the longest lifetime orbit from the scaled covariance draw is used as the nominal for a new simulation with the original covariance scaled by 100^2 applied to it. Figure 6.18 shows the manifold coordinate decomposition for this simulation. The manifold coordinate location of the long lifetime orbit used as nominal here was in the upper left quadrant of Figure 6.16 and has a smaller volume covariance applied to it in the Monte Carlo process. Thus, a cluster of longer lifetime orbits is formed around this nominal long lifetime orbit. Figure 6.19 shows the same plot zoomed in on the cluster of dispersed orbits. All orbits are color-coded yellow, with lifetimes greater than 9 days. The mean of this distribution is nearly 12 days and the maximum lifetime is 17 days. This is better lifetime performance than the original scaled covariance dispersal but doesn't produce a maximum lifetime as great as the shifted Saturn true anomaly draw. This is likely due to the specific location targeted in manifold coordinate phase

space by using the scaled covariance long lifetime orbit. Higher lifetime statistics are obtained by applying the covariance scaled by 100^2 to the long lifetime orbit from the shifted ν_S simulation.
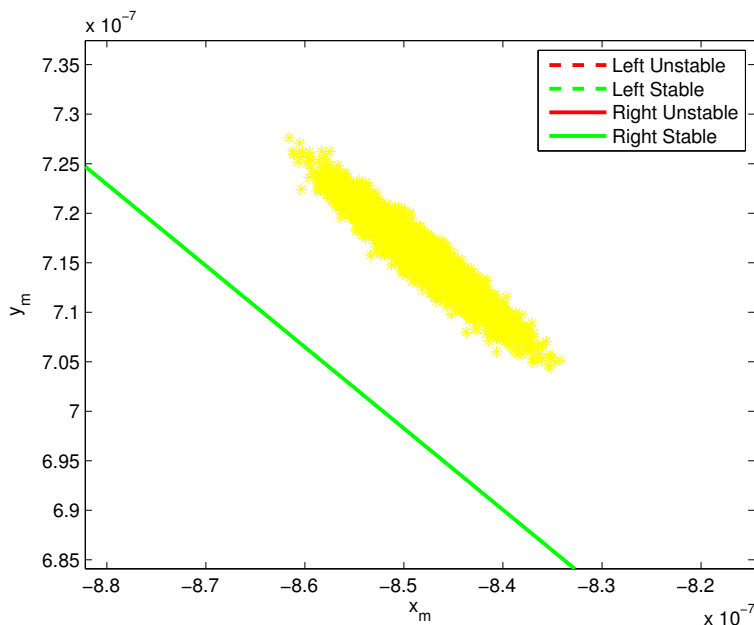
Figure 6.19: Manifold coordinate distribution for covariance scaled x100^2 applied to long lifetime orbit - zoom

Figure 6.20 shows the manifold coordinates for the dispersed long lifetime $\Delta\nu_S$ orbit Monte Carlo simulation. The nominal orbit for this case is located in the lower right quadrant of Figure 6.20. Again, applying the covariance scaled by a smaller factor results in a tighter distribution, with all orbits having lifetimes greater than 12 days. The mean and maximum lifetimes from this distribution eclipse the mean and maximums from all others at 15 and 26 days respectively. Figure 6.21 shows the same distribution zoomed in on the location of the dispersed orbits. This section has developed a method of iterative Monte Carlo simulations for increasing orbit lifetimes at Enceladus. The maximum lifetime of 26 days combined with a statistical mean of 15 days within the associated covariance would enable geodesy orbiter type missions to Enceladus where previously no low-altitude, near-polar orbits were known.
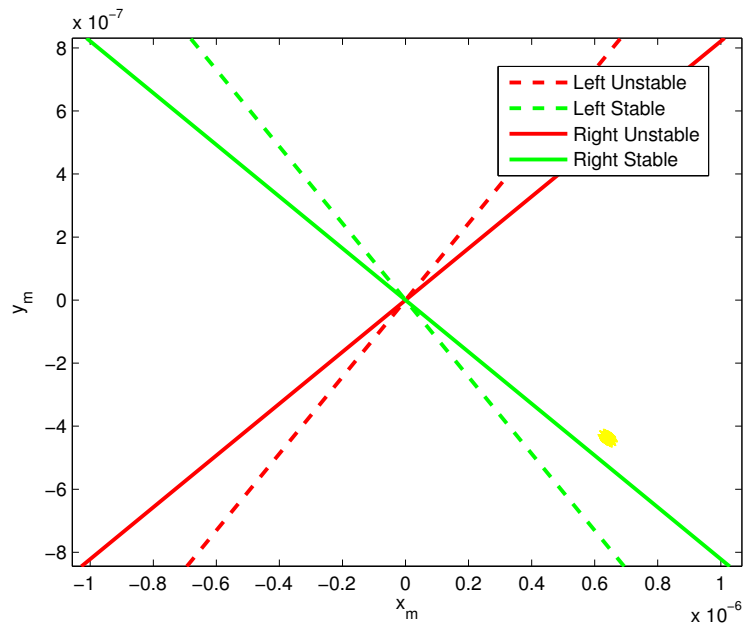
Figure 6.20: Manifold coordinate distribution for covariance scaled x100^2 applied to $\delta\nu_S = -2°$ long lifetime orbit

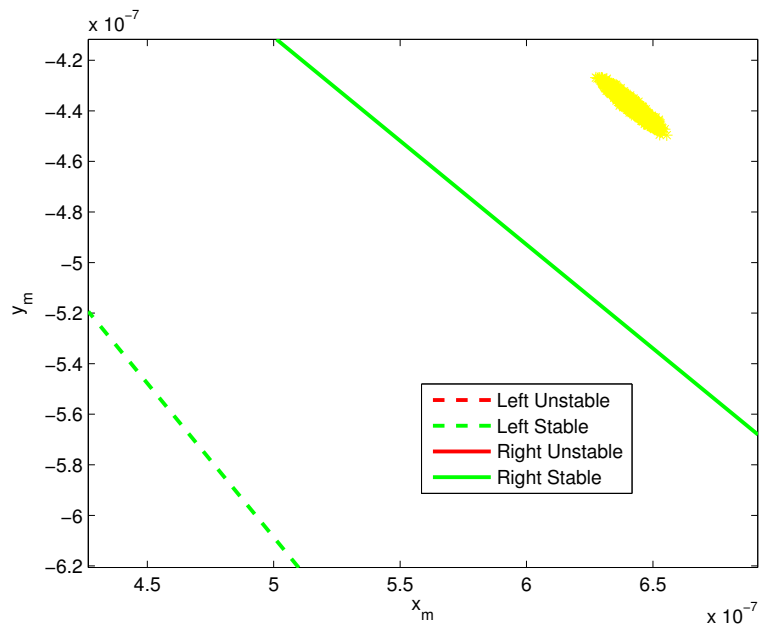Figure 6.21: Manifold coordinate distribution for covariance scaled x100^2 applied to $\delta\nu_S = -2°$ long lifetime orbit - zoom

Chapter 7

Conclusions and Future Directions

In this thesis, orbit design and navigation are investigated for planetary satellite orbiters, specifically Europa and Enceladus. Low-altitude, near-polar orbits are computed in the RTBP using a differential corrector and covariances are computed using a SRIF for both Europa and Enceladus orbits. These orbits have lifetimes comparable to long lifetime orbits found in other studies and much longer lifetimes than previous studies for low altitude Enceladus orbits. A development of information processing in the orbit determination process is given for the Jupiter-Europa system L_2 equilibrium point. The left unstable and stable manifolds associated with a fixed point are shown to control information accumulation at epoch and current state respectively. The generation of a realistic covariance is the key to evaluating long lifetime orbits in the vicinity of a periodic orbit. Monte Carlo simulations draw 10000 orbits from processed covariances and integrate them to impact in the eccentric inertial frame. Other studies fail to address how isolated long lifetime trajectories are in phase space. Manifold coordinates are used to show whether orbits are primarily aligned with the stable or unstable manifold associated with the periodic orbit. Iterating this Monte Carlo lifetime simulation increases the maximum orbit lifetime found.

7.1   Conclusions

The main contributions of this thesis are:

- Accounting for navigation uncertainties in the design of long lifetime geodesy orbits at

Europa

Periodic orbits computed in the RTBP have nominal lifetimes in the inertial eccentric frame much greater than generic, geodesy-type orbits. Long lifetime orbits are present within a realistic covariance generated for an orbiter tracked using range-rate measurements about a periodic orbit. The overall statistical lifetime distribution is improved for orbits in the vicinity of a periodic orbit. This property is not found in covariances generated for a random low-altitude, near-polar orbit in the same system.

- Understanding the properties of phase space near a periodic orbit in terms of its stable and unstable manifolds, orbit lifetime, and orbit determination

These long lifetime orbits are offset from the manifold coordinate origin which represents the periodic orbit and are aligned with the stable manifold of the nominal periodic orbit. The phase space location of long lifetime orbits is shown to be sensitive to the initial position of the primary in the three-body system and can be shifted back over the origin through incrementing the initial true anomaly of the primary. These Monte Carlo simulations are iterated by applying the nominal covariance to a long lifetime orbit from a previous simulation. Using this method, lifetimes of up to 271 days for Europa are found in these Monte Carlo covariance dispersals.

- Showing a fundamental structure to information and measurement partial mapping in terms of the stability properties of an equilibrium point

The computed stable and unstable manifolds of an unstable fixed point, which includes the Lagrange equilibrium points in the RTBP, are shown to affect the accumulation of information in the orbit determination process. Information is preferentially accumulated along the left unstable manifold for measurements mapped to epoch and along the left stable manifold for covariances mapped to the current state. This is due to the orthogonality of left and right eigenvectors and the eigenstructure of the STM, which can be decomposed into matrices of right eigenvectors, eigenvalues, and left eigenvectors. An asymmetry in information mapping is shown between left and

right eigenvectors. A full rank information matrix can be constructed from a series of the same measurement aligned with a right eigenvector. However, a series of measurements missing a left eigenvectors will have a deficient measurement direction along the right eigenvector paired with the omitted left eigenvector.

- Enabling geodesy science at Enceladus by computing statistically realistic long lifetime orbits

The process used for designing long-lifetime orbits at Europa also applies to Enceladus. The covariance associated with a low altitude, near-polar periodic orbit at Enceladus contains longer lifetime orbits. The location of these long lifetime orbits in manifold coordinate space are sensitive to shifts in the initial Saturn true anomaly. Taking the longest lifetime orbit from a scaled covariance Monte Carlo simulation and applying the nominal covariance to the orbit produces an orbit with 26 days lifetime. This is an order of magnitude improvement over random low altitude, near-polar orbits with lifetimes of only days. These long lifetime orbits also have mean and minimum lifetimes over 10 days in statistical lifetime draws. Such long lifetime orbits can be used as nominal orbits for geodesy mission designs.

7.2 Future Directions

There are several areas open to future work for this thesis. The discussion of information accumulation is not only relevant to equilibrium points. The same manifold structure exists around periodic orbits but the manifold directions are not constant in time as they are at equilibrium points. The angle of manifold intersection must be preserved between time steps although the manifold directions themselves will rotate in phase space. This is a challenge numerically since multiple mappings with the STM are required even for only a handful of measurements. Numerically integrating a monodromy matrix for each measurement time in the simulation is also not computationally feasible. A method of mapping manifolds in time which preserves the relative

eigenstructure is necessary but not currently available.

Once the problem of mapping manifolds in time is solved, the interaction between the information accumulation process and the specific phase space location of the long lifetime orbits computed here can be investigated. If the influence of stable and unstable manifolds on the accumulation of the orbiter position and velocity covariance is understood, nominal orbits can be designed to produce a specific covariance orientation which gives improved lifetime statistics. For example, designing a nominal orbit whose manifold coordinate covariance projection is aligned with the right stable manifold. This would produce more long lifetime orbits in the statistical distribution.

The information mapping theory can be applied to specific real measurements such as a position measurement along a given direction. If that direction is perpendicular in phase space to the eigenvector describing a left manifold, there will be a deficient phase space direction in the paired right manifold direction. Also, a particular direction or measurement schedule could be developed to gain the most information on the estimated state from the smallest number of measurements. Depending on the type of estimation, taking measurements where the partial is aligned with the left stable or unstable manifolds can yield information compression.

Since the most likely candidate for a Europa mission, the Europa Clipper, is now designed for multiple flybys, other planetary satellite targets can be studied as potential orbiter missions. Enceladus was chosen for analysis here because of the severity of the unstable orbital environment. Planetary moons such as Titan and Dione are both viable options for an exploration mission due to the methane sea and ice cliffs respectively. The techniques for designing long lifetime orbits developed for Europa and verified at Enceladus in this thesis would be applicable to either of these bodies.

Bibliography

[1] Park, R. S., Asmar, S. W., Buffington, B. B., Bills, B., Campagnola, S., Chodas, P. W., Folkner, W. M., Konopliv, A. S., and Petropoulos, A. E., "Detecting tides and gravity at Europa from multiple close flybys," *Geophysical Research Letters*, Vol. 38, L24202, 2011.

[2] Clark, K., Magner, T., Pappalardo, R., Blanc, M., Greeley, R., Lebreton, J., Jones, C., and Sommerer, J., "Jupiter Europa Orbiter Mission Study 2008: Final Report." NASA NMO710851, February 2009.

[3] Scheeres, D. J., Guman, M. D., and Villac, B. F., "Stability Analysis of Planetary Satellite Orbiters: Application to the Europa Orbiter. *Journal of Guidance, Control, and Dynamics.* Vol. 24, No. 4, 2001, pp. 778-787.

[4] Boone, D. R., and Scheeres, D. J., "Evaluating periodic orbits for the JEO mission at Europa in terms of lifetime and stability." American Astronautical Society, Paper AAS 11-518, August 2011.

[5] Squyres et al. "Visions and Voyages for Planetary Science in the Decade 2013-2022." United States National Research Council. March 2011.

[6] Casotto, S., and Padovan, S., "Detecting Body Tides and Librations of Europa With an Altimetric Exploration Mission." AIAA Paper 2008-7200, August 2008.

[7] Wu, X., Bar-Sever, Y. E., Folkner, W. M., Williams, J. G., and Zumberge, J. F., . "Probing Europas Hidden Ocean from Tidal Effects on Orbital Dynamics. *Geophysical Research Letters*, Vol. 28, No. 11, 2001, pp. 2245-224.

[8] Wahr, J. M., Zuber, M. T., Smith, D. E., and Lunine, J. I., "Tides on Europa, and the thickness of Europa's icy shell." *Journal of Geophysical Research*, Vol. 111, E12005, 2006. doi:10.1029/2006JE002729

[9] Lambeck, K. *Geophysical Geodesy: The Slow Deformations of the Earth.* Oxford University Press, New York, 1988, pp. 576-579.

[10] McCarthy, D. D., IERS Technical Note 21, International Earth Rotation Service, Observatoire de Paris, July 1996, pp. 40-42.

[11] Anderson, J. D., Lau, E. L., Sjogren, W. L., Schuber, G., and Moore, W. B., "Europa's Differentiated Internal Structure: Inferences from Two Galileo Encounters," *Science*, Vol. 276, No. 1236, 1997, pp. 1236-1239.

[12] Moore, W. B., and Schubert, G., "The Tidal Response of Europa," *Icarus*, Note, Vol. 147, 2000, pp. 317-319.

[13] Olgin, J. G., Smith-Konter, B. R., and Pappalardo, R. T., "Limits of Enceladus's ice shell thickness from tidally driven tiger stripe shear failure," *Geophysical Research Letters*, Vol. 38, E02201, 2011.

[14] Rappaport, N. J., Iess, L., Wahr, J., Lunine, J. I., Armstrong, J. W., Asmar, S. W., Tortora, P., Di Benedetto, M. Racioppa, P., "Can Cassini detect a subsurface ocaen in Titan from gravity measurements?", *Icarus*, Vol. 194, 2008, pp. 711-720.

[15] Paskowitz-Possner, M. and Scheeres, D. J., "Design of Science Orbits about Planetary Satellites: Application to Europa," *Journal of Guidance, Control, and Dynamics*, Vol. 29, No. 5, 2006, pp. 1147-1158.

[16] Paskowitz-Possner, M., "Orbit Design and Control of Planetary Satellite Orbiters in the Hill 3-Body Problem," Ph.D. Dissertation, Aerospace Engineering Department, University of Michigan, Ann Arbor, MI, 2007.

[17] San-Juan, J. F., Lara, M., and Ferrer, S., "Phase space structure around planetary satellites," Paper AIAA 2004-4863, August 2004.

[18] Russell, R. P., "Global Search for Planar and Three-Dimensional Periodic Orbits Near Europa," American Astronautical Society, Paper AAS 05-290, August 2005.

[19] Russell, R. P., and Lara, M., "On the design of an Enceladus science orbit," *Acta Astronautica*, Vol. 65, 2009, pp. 27-39.

[20] Gomez, G., Lara, M., and Russell, R. P., "A Dynamical Systems Approach to the Design of the Science Orbit around Europa, 19th International Symposium on Space Flight Dynamics, Paper ISTS 2006-d-02, Kanazawa, Japan, June 2006.

[21] Lara, M., and Russell, R. P., "Computation of a Science Orbit About Europa," *Journal of Guidance, Control, and Dynamics*, Vol. 30, No. 1, 2007, pp. 259-263.

[22] Lara, M., and San Juan, J. F., "Dynamic Behavior of an Orbiter Around Europa," *Journal of Guidance, Control, and Dynamics*, Vol. 28, No. 2, 2005, pp. 291-297.

[23] Scheeres, D. J., Han, D., and Hou, Y., "Influence of Unstable Manifolds on Orbit Uncertainty," *Journal of Guidance, Control, and Dynamics*, Vol. 24, No. 3, 2001, pp. 573-585.

[24] Szebehely, V. *Theory of Orbits: The Restricted Problem of Three Bodies*. Academic Press, New York, 1967, pp. 556-557.

[25] Scheeres, D. J., Williams, B. G., Miller, J. K., "Evaluation of the Dynamic Environment of an Asteroid: Applications to 433 Eros," *Journal of Guidance, Control, and Dynamics*, Vol. 23, No. 3, 2000, pp. 466-475.

[26] Bierman, G. J., *Factorization Methods for Discrete Sequential Estimation*. Mathematics in Science and Engineering, Vol. 128. Academic Press Inc. 1977.

[27] Tapley, B. D., Schutz, B. E., and Born, G. H., *Statistical Orbit Determination*, Elsevier Academic Press, Burlington, 2004, pp. 387-400.

[28] Boone, D. R., and Scheeres, D. J., "Understanding and Utilizing Properties of Phase Space near a Periodic Orbit for the Jupiter Europa Orbiter," Paper AIAA 2012-5076 , August 2012.

[29] Gustafson, E. D., and Scheeres, D. J., "Dynamically Relevant Local Coordinates for Halo Orbits," AIAA Paper 2008-6432, August 2008.

[30] Lara M., and Pelaez. "On the numerical continuation of periodic orbits. An intrinsic, 3-dimensional, differential, predictor-corrector algorithm." *Journal of Astronomy and Astrophysics* Vol. 389, No. 2, March 2002, pp. 692-701.

[31] Scheeres, D.J. *Orbital Motion in Strongly Perturbed Environments: Applications to Asteroid, Comet and Planetary Satellite Orbiters*, Springer, UK, 2012, pp.136-138.

[32] McGrath, M. A., Hansen, C. J., and Hendrix, A. R., "Observations of Europa's Tenuous Atmosphere," Chapter in *Europa*. University of Arizona Press, Tuscon, 2009, pp. 485-506.

[33] Kaula, W. M., *Theory of Satellite Geodesy: Applications of Satellites to Geodesy*. Dover Publications Inc., Mineola, New York, 2000, pp. 30-40.

[34] Vallado, D. A., *Fundamentals of Astrodynamics*. Microcosm Press 2001. Second Edition.

[35] Shum, C. K., Zhang, B. H., Schutz, B. E., and Tapley, B. D., "Altimeter Crossover Methods for Precision Orbit Determination and the Mapping of Geophysical Parameters," *Journal of the Astronautical Sciences*, Vol. 38, No. 3, 1990, pp. 355-368.

[36] Paskowitz-Possner, M. and Scheeres, D. J., "Control of Science Orbits About Planetary Satellites," *Journal of Guidance, Control, and Dynamics*, Vol. 32, No. 1, 2009, 223-231.

[37] Boone, D. R., and Scheeres, D. J., "Analysis and Implementation of Geodesy Science for the Jupiter Europa Orbiter Mission." Paper AIAA 2010-8255, Toronto, ON, Canada, August 2010.

[38] Boone, D. R., and Scheeres, D. J., "Integration of Mission Design and Navigation for a Europa Geodesy Orbiter," NASA JPL International Symposium on Space Flight Dynamics, Pasadena, CA, October 2012.

[39] Boone, D. R., and Scheeres, D. J., "Long-Life Europa Geodesy Orbits Accounting for Navigation Uncertaintites," *Journal of Guidance, Control, and Dynamics*, Accepted April 2013.

Appendix A

Manifold Coordinate Decomposition

In this Appendix, the manifold coordinate decomposition used to plot the stable and unstable manifold coordinates is discussed. Taking the dot product between the state deviation and the stable and unstable eigenvectors yields the stable and unstable coordinates a_s and a_u. These coordinates are plotted in the plane of intersection of the stable and unstable eigenvectors with the x axis bisecting the angle of manifold intersection θ. This is a non-orthogonal coordinate frame but gives insight into where the initial conditions lie in phase space. A coordinate system for plotting is established involving unit vectors aligned with $(\hat{u}, \hat{s})$ and perpendicular to $(\hat{u}_p, \hat{s}_p)$ the unstable and stable manifolds as shown in Figure 1.
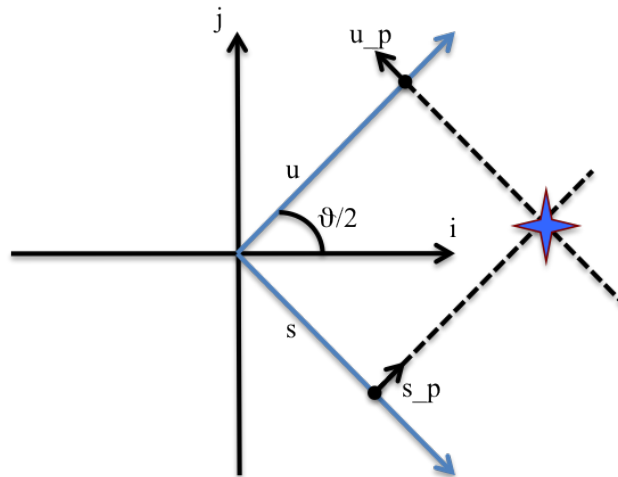

Figure A.1: Coordinate system for manifold decomposition

$$\begin{aligned}
\hat{u} &= \cos(\theta/2)\hat{i} + \sin(\theta/2)\hat{j} \\
\hat{u}_p &= -\sin(\theta/2)\hat{i} + \cos(\theta/2)\hat{j} \\
\hat{s} &= \cos(\theta/2)\hat{i} - \sin(\theta/2)\hat{j} \\
\hat{s}_p &= \sin(\theta/2)\hat{i} + \cos(\theta/2)\hat{j}
\end{aligned} \tag{A.1}$$

The point of intersection of the projection of the stable and unstable coordinates along the perpendicular to their respective manifolds is represented by the orange star in the figure. So, equating the two plotting representations using the stable, unstable, and perpendicular unit vectors where t and r are scalars gives the magnitude along the perpendicular directions.

$$a_u \hat{u} + t\hat{u}_p = a_s \hat{s} + r\hat{s}_p \tag{A.2}$$

In the xy coordinate framework, this looks like:

$$\begin{aligned}
\hat{i} &: a_u \cos(\theta/2) - t\sin(\theta/2) = a_s \cos(\theta/2) + r\sin(\theta/2) \\
\hat{j} &: a_u \sin(\theta/2) + t\cos(\theta/2) = -a_s \sin(\theta/2) + r\cos(\theta/2)
\end{aligned} \tag{A.3}$$

Solving for the t scalar in terms of r:

$$\hat{i}: t = \frac{a_u \cos(\theta/2) - a_s \cos(\theta/2) - r\sin(\theta/2)}{\sin(\theta/2)} \tag{A.4}$$

and substituting into the $\hat{j}$ equation gives an expression involving only the r unknown.

$$\hat{j}: a_u \sin(\theta/2) + \frac{a_u \cos(\theta/2) - a_s \cos(\theta/2) - r\sin(\theta/2)}{\sin(\theta/2)} \cos(\theta/2) = \\ -a_s \sin(\theta/2) + r\cos(\theta/2) \tag{A.5}$$

Solving for r yields the magnitude along the $\hat{s}_p$ vector to add to the extent along the stable manifold direction.

$$r = \frac{a_u \sin(\theta/2) + (a_u \cos(\theta/2) - a_s \cos(\theta/2))\frac{\cos(\theta/2)}{\sin(\theta/2)} + a_s \sin(\theta/2)}{2\cos(\theta/2)} \tag{A.6}$$

The point plotted in the initial condition distribution figures is $x_M^\star$ which corresponds to the orange star in Figure 1. This process is repeated for each initial condition projected into manifold space.

$$x_M^\star \;=\; a_s \hat{s} + r \hat{s}_p \tag{A.7}$$